Contents

List of Figures

List of Tables

Chapter 1

Introduction

1.1. Objectives of the work

This present study emphasizes ocean surface wave measurements using Synthetic Aperture Radar (SAR) wave mode data. The following points are the main contributions of this study.

- Validation of SAR ocean wave retrieval using the non-linear PARSA algorithm and the quasi-linear one used for ASAR wave mode Level2 WVW products from ESA.
- Development of a new CWAVE_ENV algorithm for the ASAR wave mode data.
- Global validation of the CWAVE_ENV empirical algorithm.
- A global sea state statistical analysis derived from ASAR wave mode data using the CWAVE_ENV empirical algorithm.
- Investigation of extreme sea state measurements using SAR wave mode data.
- Coastal surface wave measurements using high resolution TerraSAR-X data.

In the frame work of this thesis, following articles in Chapter 5 – 9 have been published or are under review.

- Li, Xiao-Ming; Lehner, Susanne; He, Ming-Xia (2008): Ocean wave measurements based on satellite synthetic aperture radar (SAR) and numerical wave model (WAM) data - extreme sea state and cross sea analysis. *International Journal of Remote Sensing*, **29** (21), pp. 6403 - 6416, DOI: 10.1080/01431160802175546
- Li, Xiao-Ming; Lehner, Susanne; and Thomas Bruns (2009), "Ocean Wave Integral Parameter Measurements Using ENVISAT ASAR Wave Mode Data," submitted to *IEEE Transactions on Geoscience and Remote Sensing.*

- Li, Xiao-Ming; König, Thomas; Schulz-Stellenfleth, Johannes; and Lehner, Susanne (2009), "Validation and intercomparison of ocean wave spectra retrieval scheme using ASAR wave mode data," submitted to *International Journal of Remote Sensing*.
- Li, Xiao-Ming and Lehner, Susanne (2009), "Utilization of ASAR Wave Mode Data for Shipping Safety," Proceedings of Oceans' 09 IEEE, Bremen, Germany, DOI: 10.1109/OCEANSE.2009.5278274
- Li, Xiao-Ming; Lehner, Susanne; Rosenthal, Wolfgang (2010): Investigation of Ocean Surface Wave Refraction Using TerraSAR-X data. *IEEE Transactions on Geoscience and Remote Sensing,* **48**(2), pp.830-840, DOI: 10.1109/TGRS.2009.2033177.

While the articles are represented in the relevant chapters, a general introduction, a wider outlook, and summary and conclusions are given.

1.2. State of the art - - Satellite measurements of ocean waves

We live on a water planet. Ocean covers over 70% of the Earth's surface and contains about 97% of the Earth's surface water. The ocean plays a major role in climate and weather.

Waves are the ocean's most obvious surface feature. They play a significant role in the processes at the air-sea interface, the ocean surface mixed layer, and the atmosphere marine boundary layer. Consequently, waves impact upon surface winds, surface currents, turbulent mixing in the surface mixed layer and consequently the transport of heat, momentum and freshwater. Knowledge of the large-scale climate of the ocean surface waves, in terms of seasonal patterns and natural variability is of central importance to climate studies. Many have demonstrated the researches on relationship between the wave climate and the global climate change, e.g. whether the increased wave height in northeast Atlantic Ocean is related to the increased surface air temperature and storminess, as described by *Grevemeyer et al*., [2000] and *Von Storch and Weisse* [2008].

Ocean waves are traditionally measured in situ at one point as by moored buoys, which are often located near coasts, therefore giving very limited spatial coverage.

Numerical wave modeling is an important approach to generate and predict surface sea state. The third generation WAve Model (WAM) has made promising progress since 1984 [WAMDI, 1988]. From June 1992 outwards a new version of WAM called cycle 4 [*Komen*, 1994] was introduced operationally at the European Centre for Medium-Range Weather Forecasts (ECMWF). For global sea state forecasts, the horizontal resolution of WAM is operated at the ECMWF at 1.5º resolution, and for regional forecast a higher resolution model up to 10 km is available as well, e.g., the WAM run operationally at Deutscher Wetterdienst (DWD). Modelers have improved wave model forecast performance considerably. During 1992-1993, the RMSE error of the 24-hour forecast of ECMWF was around 0.75 m for SWH which has been reduced to 0.25 m in 2002-2003, due to the assimilation of sea state and surface wind observations provided by satellite sensors, e.g., Radar Altimeter (RA), SAR and Scatterometer [*Janssen*, 2008]. The accuracy of some regional numerical wave models is validated as well in extreme sea state, for instance the LSM (Local Sea wave Model) operated by the DWD. This was tested, e.g., in selected severe winter storms over the North and the Baltic Sea, giving reasonable quality for short period forecasts [*Behrens and Günthe*r, 2008].

However, with respect to the long-term accuracy of global wave models, there is still room for improvement as shown in the validation for the reanalysis ERA-40 wave products. SWH is slightly overestimated for low sea state (<1.5 m) and substantially underestimated by more than 20% for rough sea state, when compared to the RA onboard Topex/Poseidon and *in situ* buoy measurements [*Caires and Sterl*, 2003].

Satellite remote sensing, particularly the active microwave sensors SAR and RA, offers alternative approaches for the observation of ocean surface waves with global coverage and independence of cloud coverage and daylight.

Satellite altimeters consist of a radar measuring the height of the satellite above the sea surface and a tracking system to determine the height of the satellite in geocentric coordinates. The system measures the sea surface height (SSH) relative to the center of mass of the Earth. This gives the shape of the sea surface. Spaceborne altimetry including Seasat (1978), Geosat (1985–1988), ERS–1 (1991–1996), ERS–2 (1995–), Topex/Poseidon (1992–2006), Jason (2002–), and Envisat (2002-) has produced a large dataset for sea level, near surface wind speed , sea state and even

further for insight into oceanic low-frequency variability, e.g., eddy characteristics analyzed by *Stammer* [1997]. The altimeter can measure wave height to about an accuracy of ±10% or 0.25 m, e.g. seen in *Carter et al.* [1992]; *Challenor and Cotton* [2002] and *Queffeulou* [2004]. Unlike the approach for SWH measurements, retrieval of wave period from RA is still under development. Several empirical models, e.g., *Gommenginger et al.* [2003], *Quilfen et al.* [2004] and *Mackay et al.* [2008] have been suggested to obtain wave period measurements from altimeter data.

ERS-1/2 SAR and ENVISAT ASAR can operate in wave mode thus acquiring global ocean surface wave measurements every 200 km or 100 km along the orbits, when the image mode (typical with swath width of 100 km by 100 km) data are not requested. Wave mode data are particularly suitable for global wave measurements and statistics. Since the launch of ERS-1 in 1991 SAR wave mode data were acquired by only the SAR image spectrum, namely the User Wave (UWA) spectrum (SAR wave fast delivery product) [*Brooker*, 1995] is available. The full wave mode data became available since 2002, when ENVISAT was launched. This gave the possibility to study individual waves in the open sea. Using three years (1993-1995) ERS-1 SAR wave mode, an assessment for the performance of the MPI retrieval scheme [*Hasselmann and Hasselmann*, 1991] as well as the operational feasibility was given by *Heimbach et al.* [1998]; the analysis of ERS SAR wave mode image intensity data was performed by *Kerbaol et al.* [1998]; and wind and wave measurements delivering global wave statistics using two years reprocessed ERS-2 SAR wave mode data [*Lehner et al.*, 2000; *König et al.*, 2007; *Li et al.*, 2008] are also available.

Since the launch of ENVISAT on 2002, wave mode data itself and high level products (the so called retrieved ocean wave spectra) are available and are provided to users [*ENVISAT Handbook*, 2007]. These ocean wave spectra only yield information on the inner spectral bins [*Abadalla et al.*, 2008] contained in the ASAR wave mode data. Validation (see Chapter 4) shows that the integrated wave parameter SWH of these high level products is significantly underestimated and does not give correct measurements for sea state with SWH larger than 4 m.

With the algorithm CWAVE, a new empirical approach delivers SWH and mean wave period, rather than the full two-dimensional wave spectra. The algorithm does not need priori information. For the ERS mission, the empirical algorithm

CWAVE_ERS [*Schulz-Stellenfleth et al.*, 2007] was proposed for the reprocessed ERS-2 SAR wave mode data. Validation results show that the performance of CWAVE _ERS is fairly good when compared to the ECMWF WAM model using 6000 collocation data pairs and 21 buoy measurements during three weeks in 1996. For both comparisons with respect to SWH, results of CWAVE_ERS show a bias and an RMS of 0.44 m and 0.39 m, respectively.

As the full SAR wave mode data are not provided as standard products for the ERS mission, and also considering that ENVISAT ASAR wave mode data have different spatial resolution, image size, calibration constant and ocean surface imaging performance compared to ERS SAR wave mode data, the empirical algorithm is here extended to ASAR wave mode data. This will contribute to acquire a complete independent global wave measurements dataset used for analyzing global wave statistics and for satellite data assimilation into numerical wave models.

1.3. Outline of the thesis

This thesis is structured as follows. After a brief introduction, basic knowledge on ocean waves is introduced in Chapter 2. Chapter 3 contains the introduction of the SAR system and its geometry. SAR ocean wave imaging mechanisms as well as two-dimensional wave spectra inversion schemes are discussed. The main dataset used in the present study is then described in Chapter 4.

The application of ERS-2 SAR wave mode data to global wave measurements is presented in Chapter 5 including also a case of cross sea that occurred in the South Pacific.

Performance of the existing ASAR wave mode products and the non-linear parametric inversion scheme PARSA for ocean wave spectra and integral wave parameters is presented in Chapter 6. An assessment of the performances of both algorithms under high sea state is given as well.

In Chapter 7, the newly developed empirical algorithm CWAVE_ENV to derive integral wave parameters from ASAR wave mode data is described in detail. Its validation is carried out by comparison to *in situ* buoy measurements, numerical wave model results and radar altimeter data.

In order to investigate spatial variations of wave refraction and diffraction in

coastal zones, wide swath SAR data acquired by TerraSAR-X over Terceira island are used to derive high resolution wave direction, wavelength, and SWH fields in Chapter 8.

One full year (2006 June to 2007 May) global ASAR wave mode data have been processed. Statistical analysis for sea state, including extreme wave height estimation, global wave maps of SWH, mean wave period, and wave steepness are presented in the Chapter 9.

Conclusions and an outlook are given in Chapter 10.

Appendices are listed in Chapter 11.

Chapter 2

Ocean Wave Basics

In this chapter, basic elements of ocean surface gravity wave theory are briefly introduced.

Ocean surface waves may be characterized by their period, which is the time taken by successive wave crests to pass a fixed point. Fig.2.1 demonstrates the classification of ocean waves by wave period.

The present study is concerned with remote sensing of ocean surface gravity waves having periods between 3 s ~ 30 s. The gravity waves are distinguished in two states: *windsea*, when the waves are being generated by the wind, and *swell*, when they have traveled away and escaped the influence of the generating wind.

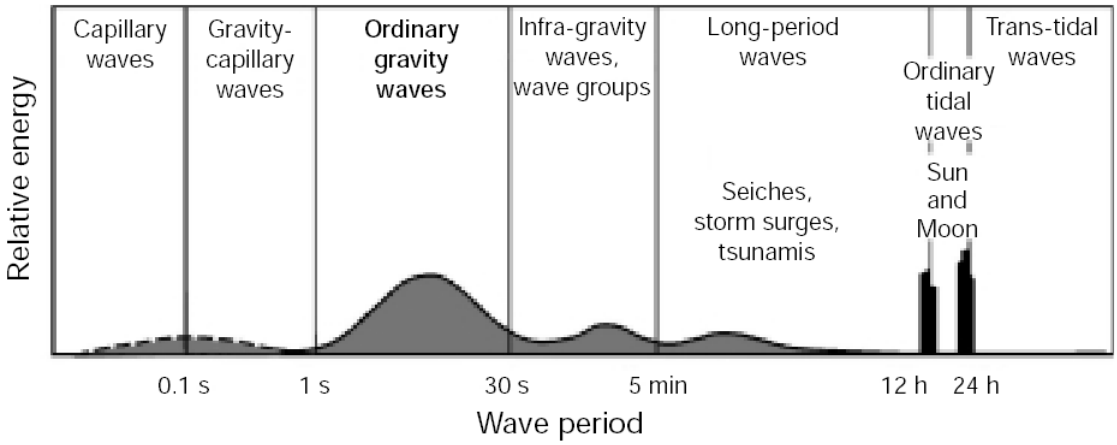

*Figure 2. 1*Classification of ocean surface waves [After ECMWF training course http://www.ecmwf.int/newsevents/training/rcourse_notes/NUMERICAL_METHODS /index.html]

2.1. Description of ocean waves

The ocean surface appears to be composed of random waves with various height, lengths and directions. The basic model for describing the moving surface elevation is the **random-phase/amplitude model** [*Holthuijsen*, 2007], in which the sea surface is considered to be the sum of a large number of harmonic waves. Each of them may be represented by a sinusoidal, long-crested, progressive wave:

$$\eta(x,t)=\frac{H}{2}\sin\left(\frac{2\pi}{T}t-\frac{2\pi}{L}x\right) \tag{2.1}$$

where H is the wave height, T is the wave period and L is the wavelength (see illustration in Fig.2.2). *Amplitude* $a=H/2$, *radian frequency* $\omega=2\pi/T$ and *wave number* $k=2\pi/L$, so that the propagating harmonic wave can be written as

$$\eta(x,t)=a\sin(\omega t-kx) \tag{2.2}$$

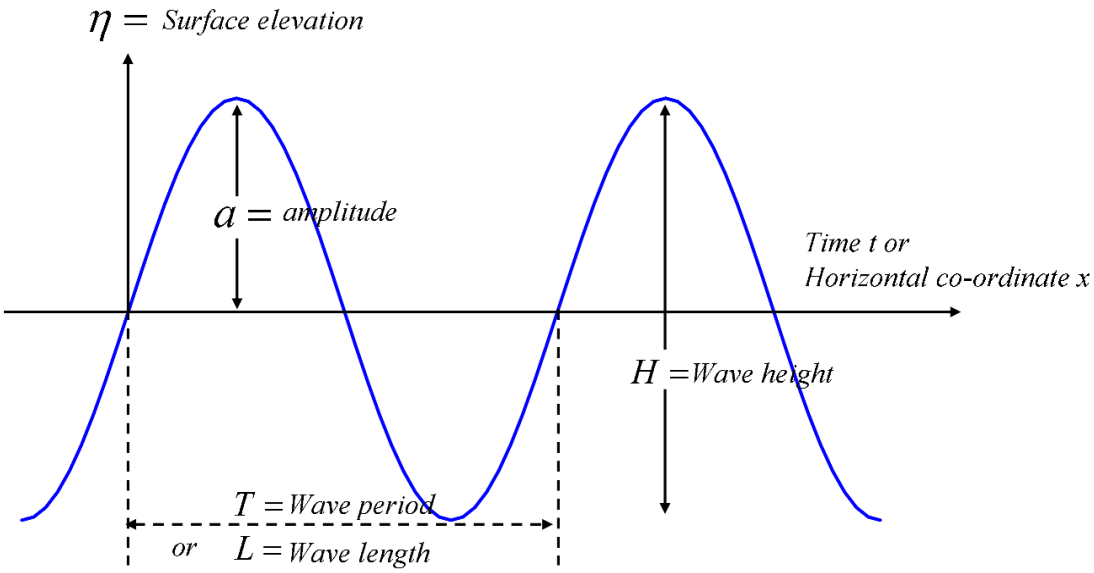

Figure 2. 2 A sine wave

Then the random surface elevation can be expressed by the sum of numerous sinusoidal waves with different frequencies, amplitudes and phases,

$$\eta(t)=\sum_{i=1}^{N}a_i\sin(\omega_i t+\phi_i) \text{ or } \eta(t)=\sum_{i=1}^{N}a_i\sin(2\pi f_i t+\phi_i) \tag{2.3}$$

Where N is a large number and the amplitude a_i and phase ϕ_i ($0<\phi_i\le 2\pi$) are random variables.

Wave spectrum

Equ. (2.2) shows that the water surface time history measured at a fixed point can be reproduced by linearly adding a large number of component sine waves having different amplitudes, frequencies, and phases. The continuous **variance density spectrum** $E(f)$ for the sea surface elevation is:

$$E(f) = \lim_{\Delta f \to 0} \frac{1}{\Delta f} E\left\{\frac{1}{2} a_i^2\right\} \tag{2.4}$$

Here the $E(\cdot)$ means variance density while $E\{.\}$ stands for expected value. The unit for $E(f)$ is $\left[m^2/Hz\right]$ or $\left[m^2/rad\right]$. The total variance $\langle \eta^2 \rangle$ of the sea surface elevation is the sum of the variances of all frequency bands Δf or for a continuous spectrum,

$$\langle \eta^2 \rangle = \int_0^\infty E(f)\, df \tag{2.5}$$

The variance density spectrum $E(f)$ shows how the variance of the sea surface elevation is distributed over the frequencies. By multiplying with ρg, one can get the **energy density spectrum**:

$$E_{ene}(f) = \rho g E_{\mathbf{var}}(f) \tag{2.6}$$

Here the two terms, variance density spectrum and energy density spectrum, are used indiscriminately. Transforming the spectrum into the radiance frequency, gives:

$$E(\omega) = E(f)\frac{df}{d\omega}$$

The harmonic wave is described as a one-dimensional process without considering the directions. For the actual sea surface, the horizontal dimension, i.e. direction of wave propagation, has to be added.

$$\eta(x, y, t) = a\,\mathbf{sin}\left(\omega t - kx\,\mathbf{cos}\,\theta - ky\,\mathbf{sin}\,\theta + \phi\right) \tag{2.8}$$

where $k = 2\pi/L$ is the wave number and θ is the direction of wave propagation. Then the sea surface elevation can be described by the sum of numerous such harmonic

waves:

$$\eta(t)=\sum_{i=1}^{N}\sum_{j=1}^{M}a_{i,j}\sin\left(\omega_i t-k_i x\cos\theta_j-k_i y\sin\theta_j+\phi_{i,j}\right) \tag{2.9}$$

Each wave component is therefore indicated in Equ.(2.9) with two indices: i for the frequency (or wave number) and j for the direction.

Similar with Equ.(2.4), the **two-dimensional** variance density spectrum for the three-dimensional sea surface elevation is given by:

$$E(f,\theta)=\lim_{\Delta f\to 0}\lim_{\Delta\theta\to 0}\frac{1}{\Delta f\Delta\theta}E\left\{\frac{1}{2}a_i^2\right\} \tag{2.10}$$

and transformed to the radian frequency domain:

$$E(\omega,\theta)=\lim_{\Delta\omega\to 0}\lim_{\Delta\theta\to 0}\frac{1}{\Delta\omega\Delta\theta}E\left\{\frac{1}{2}a_i^2\right\} \tag{2.11}$$

The two-dimensional spectrum $E(f,\theta)$ shows how the variance of sea surface elevation is distributed over frequencies and directions. By integrating the variances in all directions, one can get the one-dimensional spectrum:

$$E(f)=\int_0^{2\pi}E(f,\theta)d\theta \tag{2.12}$$

The directional frequency spectrum $E(f,\theta)$ is related to the wave number spectrum $E(\mathbf{k})$ via

$$E(f,\theta)=\frac{32\pi^4 f^3}{g^2}E(\mathbf{k}) \tag{2.13}$$

A directional wave number spectrum (hereafter referred to as 2D or two-dimensional spectrum) is displayed in Fig. 2.3.

The sea state can be characterized by different integral parameters, e.g., SWH (often also designated H_s), mean wave period (e.g. zero upcrossing wave period, denoted as T_{m02})

$$H_s=4\sqrt{\int E(f,\theta)df\,d\theta} \tag{2.14}$$

$$T_{m02} = \sqrt{\int E(f,\theta) df d\theta \Big/ \int E(f,\theta) f^2 df d\theta} \tag{2.15}$$

Another practical definition of significant wave height H_s is to be computed as the average of the 30% highest wave crests during the observation period.

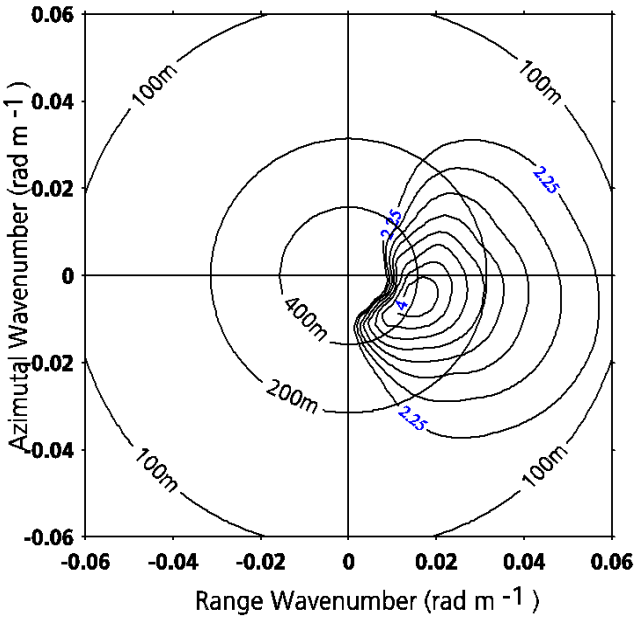

Figure 2. 3 An example of a directional spectrum computed by the WAM Model (see section 2.5). Unit of the wave energy isoline is m^2/rad

2.2 Wave propagation in deep water

In fluid dynamics, the Airy wave theory [*Airy*, 1841] (often referred to as linear wave theory) gives a linear description of the propagation of gravity waves in deep waters (such that the waters are unaffected by the seabed), without currents or obstacles like islands and breakwaters. The linear wave theory of gravity waves is valid only if some assumptions are fulfilled.

1. Water depth h is constant.

2. Wave motion is two-dimensional, which leads to waves with long crest and constant wave height H.

3. Ocean wave is incompressible and the effects of viscosity, turbulence and surface tension can be neglected.

4. Wave height H is small compared to the wave length L and water depth h, i.e. $H/L \le 1$ and $H/h \le 1$.

Wave frequency ω is related to wave number k by the **dispersion relation** [*Lamb*, 1945]:

$$\omega^2 = gk\,\mathbf{tanh}(kh) \tag{2.16}$$

where h is the water depth and g is the acceleration of gravity.

For deep water ($\mathbf{tanh}(kh) \to 1$ for $kh \to \infty$), the dispersion relation is reduced to:

$$\omega^2 = gk \tag{2.17}$$

The propagation speed of the surface wave profile, i.e., the **phase speed**, is obtained from the dispersion relation (2.16) with $C = \omega/k$.

$$C = \sqrt{\frac{g}{k}\mathbf{tanh}(kh)} \tag{2.18}$$

In deep water, Equ.(2.18) reduces to:

$$C = \sqrt{\frac{g}{k}} \tag{2.19}$$

indicating that long waves propagate faster than short waves.

2.3. Wave propagation in shallow waters

When ocean waves enter coastal waters, their amplitude and direction are affected by the limited water depth.

When a harmonic wave propagates over seabed topography, it begins to change as it "feels" the bottom. Since the wave period remains constant, therefore via dispersion relationship (2.16), its wave length becomes progressively shorter and the phase speed C correspondingly decreases. This near-shore process of surface gravity waves is called **wave shoaling**.

Provided that the harmonic wave approaches a straight coast at an angle α_d, the part of the wave in deep water moves more rapidly than it does in shallow water (Equ.

(2.18) for phase speed). The effect causes the wave to turn parallel to the bottom contours. This phenomenon is called **wave refraction** as demonstrated in Fig.2.4.

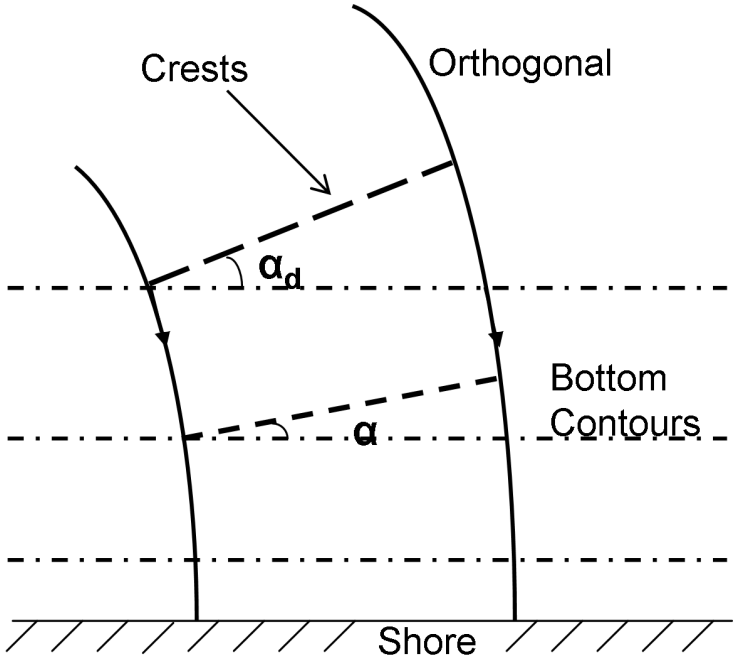

Figure 2. 4 Sketch of wave refraction caused by bottom topography

During the wave refraction process, the change of wave height becomes rather complex. Wave height H in shoaling water is quantified by using [*Kinsman*, 1965]:

$$H = H_d DK \tag{2.20}$$

in which H_d is the SWH in deep water. D is called shoaling coefficient given by

$$D = \left(\frac{k}{k_d}\right)^{1/2} \left(1 + \frac{2kh}{\sinh(2kh)}\right)^{-1/2} \tag{2.21}$$

and the refraction coefficient K is determined by

$$K = \left(\frac{\cos(\alpha_d)}{\cos(\alpha)}\right)^{1/2} \tag{2.22}$$

Using Snell's law, α in (2.22) is expressed by,

$$\alpha = \sin^{-1}(\frac{k_d}{k}\sin(\alpha_d))$$

(2.23)

It can be observed that the shoaling effect of D, which is only relative to the water depth alone, acts first to decrease wave height as the waves shoal and then when the decreasing depth reaches some threshold (i.e., ratio of shallow water depth to wave length in deep water lower than 0.056 proposed in [*Kinsman*, 1965]), the wave height increases again. The coefficient K is taken relative to the approaching angle α_d of the waves in deep water. Therefore, change of wave height during the wave refraction process is governed by both factors.

When the waves propagate around obstacles such as small islands, reef and breakwaters, the wave amplitude may vary rapidly across the geometric shadow line of such obstacles. This rapid variation in amplitude causes the waves to turn into the areas with lower amplitude. This phenomenon is called **wave diffraction**.

All these phenomena described above are due to the transportation characteristics of the waves. They can be accommodated by the linear wave theory as long as the waves are not too steep or not in very shallow water [*Holthuijsen*, 2007].

2.4. Generation of waves and decay

The growth of waves due to wind is described by three different physical processes [*Stewart*, 1985], i.e. generation, dissipation and nonlinear interaction.

Small waves with wavelength of a few centimeters are produced by random pressure fluctuations associated with turbulence in the sea surface wind. This is called Phillip's resonance [*Phillips*, 1957], a process significant early in the growth of waves on a calm sea.

The wind continues acting on the small waves causing them to become larger. Wind pressure over the waves is different along the wave profile and causes wave growth, which is unstable due to the differences of wind pressure. The higher the waves, the larger the pressure differences and thus the waves grow faster. The instability makes the waves to grow with exponential rate [*Miles*, 1957].

The above two stages are considered for wind waves in the process of growing. During this stage, the waves begin to interact among themselves [*Hasselmann et al.*,

1973]. The interaction transfers wave energy from short waves to longer waves and eventually, this leads to longer waves going faster than the wind. When the longer waves propagate out of the generating area, they are called "swell". The propagation of swell in the open sea and the deep water is described by the dispersion (as shown in Equ.(2.16)). Dispersion and angular spreading can be considered as the main causes of a gradual decrease of swell waves. For the deep ocean, the primary mechanism of swell wave energy dissipation is whitecapping. As waves grow, their steepness increases until a critical point when they break. This kind of dissipation depends on the existing energy of the swell waves and on the wave steepness [*Hasselmann*, 1974; *Komen et al.*, 1994]. This dissipation is often small enough that swell can survive over long distances. A well-known example is that of *Snodgrass et al*. [1966] who observed waves generated in the Antarctica propagate all the way across the Pacific to the Gulf of Alaska.

The diagram in Fig. 2.5 quantitatively describes the empirical swell propagation relating distance, wave height and wave period as well as the wind speed in the generating area.

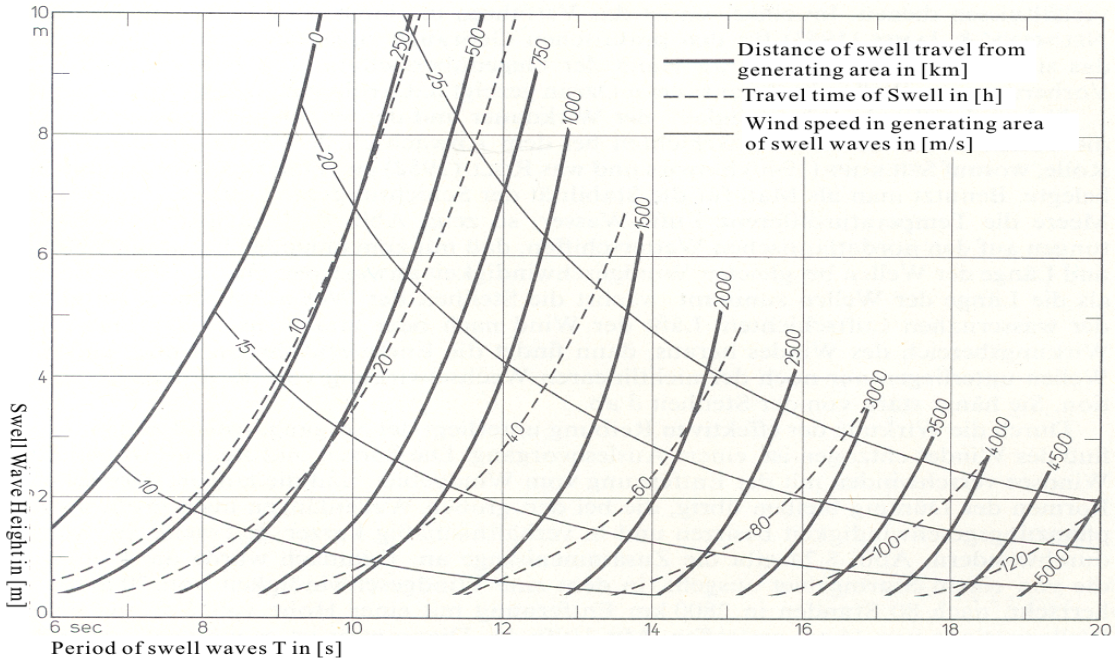

Figure 2. 5 Relation of swell wave height and period depending on the distance from the generation region and the travel time of the swell as well as wind speed in the generating area. [*Dietrich et al.*, 1975, pp.254]

The diagram can be used to track storms generating swell. The swell propagates in the open ocean on great circles and can be observed far from the storms. If wind speed and wave height are measured in the storm, e.g. by remote sensing radar data, the swell can be forecasted for large traveling distance and a time span accordingly.
When swell propagates into shallow water, a number of mechanisms may be involved in the dissipation of wave energy, which includes bottom friction, and bottom motion.

2.5. Numerical wave model

After the introduction of the concept of a wave spectrum by *Pierson et al.* [1964], different wave models were developed, which are commonly classified into three generations [*Komen et al*., 1994]. First and second generation models were analyzed and intercompared in SWAMP [1985]. As the result of this intercomparison, a third generation wave model was developed in which the wave spectrum is computed by integration of the energy balance equation without any priori restriction of the spectral shape. The model is expressed in terms of an action balance equation:

$$\frac{\partial E}{\partial t} + C_g \left(\frac{\partial E}{\partial x} + \frac{\partial E}{\partial k} \right) = S = S_{in} + S_{nl} + S_{ds} \tag{2.24}$$

where: $E = E(k, x, t)$ is the action density spectrum depending on wave number k, time t, and locations x. C_g is the deep-water group velocity.
S is the net source function, consisting of three terms:

S_{in}: Energy input by wind;

S_{nl} :Non-linear energy transfer by wave-wave interactions [*Hasselman*, 1962]

S_{ds} : Dissipation [*Komen et al*., 1994]

This form of the equation is valid for deep water without refraction and no significant currents. From the full spectrum integral quantities like SWH or mean wave period are calculated by (2.14) and (2.15).

Up to now, quite a few improved models [WAM cycle 4 by *Günther et al*. 1992; WAVEWATCH by *Tolman*, 1989; *Tolman,* 1992] use the basic WAM formulations. Improvements mainly concentrate on the source-term parameterization, particularly in the wind input, the propagation dynamics, and the extension to shallow-water and coastal regions.

Chapter 3

SAR Basics

In this chapter principles of Synthetic Aperture Radar (SAR), as well as the SAR ocean wave imaging theory and inversion algorithms are explained.

SAR designs and applications have developed since the 1950s when Carl Wiley of Goodyear Aircraft Corporation discovered that with a side looking airborne radar (SLAR), Doppler could be used to improve the cross-range spatial resolution of the radar. The first experimental validation was carried out in 1953 by a group of scientists at the University of Illinois [*Sherwin et al.*, 1962]. The following section provides a summary of civilian Earth observing SAR satellites.

3.1. Review of SAR systems

The first civilian SAR mission in space was the SEASAT in L-band, which operated only from early July to mid-September in 1978. Afterwards, there has been a considerable increase in SAR satellite missions. A brief summary for the spaceborne SAR missions is given in Table 3.1. The general characteristics of these radars are compared and contrasted. The acronyms are defined in the following.

IM: Image mode; **AP**: Alternative Polarization mode; **WS**: Wide Swath mode;
HS: High-resolution Spotlight mode; **SL**: Spotlight mode; SM: StripMap mode;
SC: ScanSAR mode

SAR systems developed from low resolution to high resolution, from single imaging mode to multi modes, and from single polarization to dual- and/or Quad-polarizations. TerraSAR-X, Cosmo-SkyMed and Radarsat-2 launched in 2007 are the representatives of the so-called “new generation” civilian SAR system, which can achieve high resolution up to 1 m when operating in spotlight mode.

Table 2. 1 Main Spaceborne SAR missions

Satellite	Country	Year	Band & wavelength (cm)	Incidence Angle (degree)	Polarization	Range Resolution (m)	Azimuth Resolution (m)
SEASAT	USA	1978	L-band (23.5)	23	HH	25	25 (4 looks)
ERS-1/2	Europe (ESA)	1991/1995	C-band (5.7)	23	VV	25	25
ALMAZ	USSR	1991	S-band (10)	30-60	HH	15	30
JERS-1	Japan	1992	L-band (23.5)	39	HH	18	18
Radarsat-1	Canada	1995	C-band (5.7)	20-50	HH	25 (standard mode) 35 (wide mode) 9 (fine res. mode) 50 (scansar mode)	28 (standard mode) 28 (wide mode) 9 (fine res. mode) 50 (scansar mode)
ENVISAT	Europe (ESA)	2002	C-band (5.7)	15-45	HH,HV, VH, VV	30 (IM and AP mode) 150 (WS mode) 1000 (GM mode)	30 (IM and AP mode) 150 (WS mode) 1000 (GM mode)
TerraSAR-X	Germany	2007	X-band (3.1)	20-55	HH,HV, VH, VV	1.5-3.5 (HS mode) 1.5-3.5 (SL mode) 1.7-3.5 (SM mode) 1.7 -3.5 (SC mode)	1 (HS mode) 2 (SL mode) 3 (SM mode) 16 (SC mode)
Radarsat-2	Canada	2007	C-band (5.7)	20-49	HH,HV, VH, VV	25 (standard mode) 25 (wide mode) 10 (fine res. mode) 50 (scansar mode)	28 (standard mode) 28 (wide mode) 9 (fine res. mode) 50 (scansar mode)

3.2. SAR geometry and system parameters

Synthetic Aperture Radars were developed as a means of overcoming the limitations of real aperture radars (RAR). These systems can achieve good azimuth resolution, but have to use large antenna. A synthetic aperture is produced by using the forward motion of the radar to illuminate one target or scatter with many successive pulses and acquire the echoes in sequence. By recording and then combining these individual signals, a "synthetic aperture" is created in the computer providing a much improved azimuth resolution. Figure 3.1 illustrates how this is achieved.

As a **target (A)** first enters the illumination of radar beam (1), the backscattered echoes from each transmitted pulse begin to be recorded. As the platform keeps moving forward, all echoes from the target for each pulse are recorded during the entire time that the target is within the beam. Till the target leaves the view of radar beam (2), the length of the **synthesized aperture (B)** is determined. This method of achieving uniform, fine azimuth resolution across the entire imaging swath is called **synthetic aperture radar**, or **SAR**.

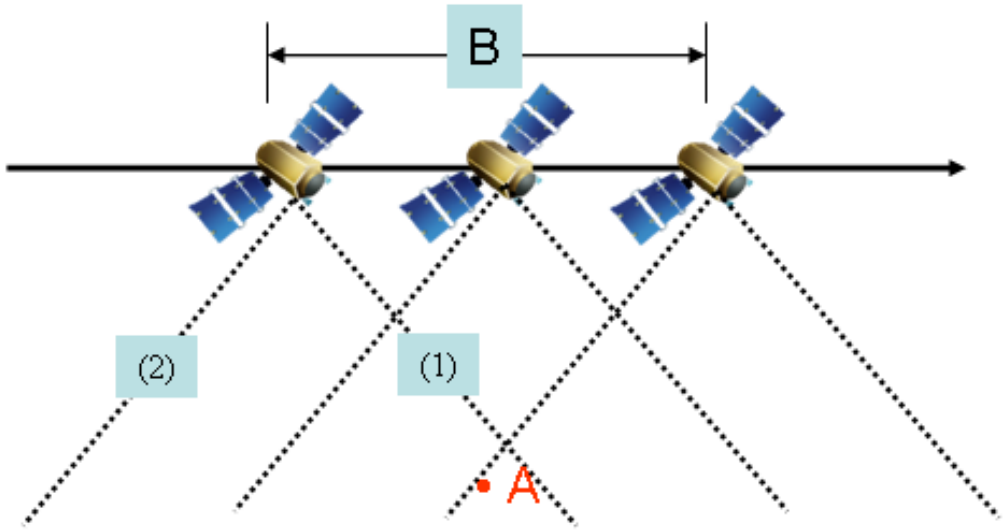

Figure 3. 1 SAR operating principles

SAR is a typical side looking radar with a geometry demonstrated in Figure 3.2. The platform moves forward in the flight direction. The microwave beam is transmitted obliquely at right angles to the direction of flight illuminating a **swath (B)**

which is offset from **nadir** (A). **Range (C)** refers to the across-track dimension perpendicular to the flight direction, while **azimuth (D)** refers to the along-track dimension parallel to the flight direction.

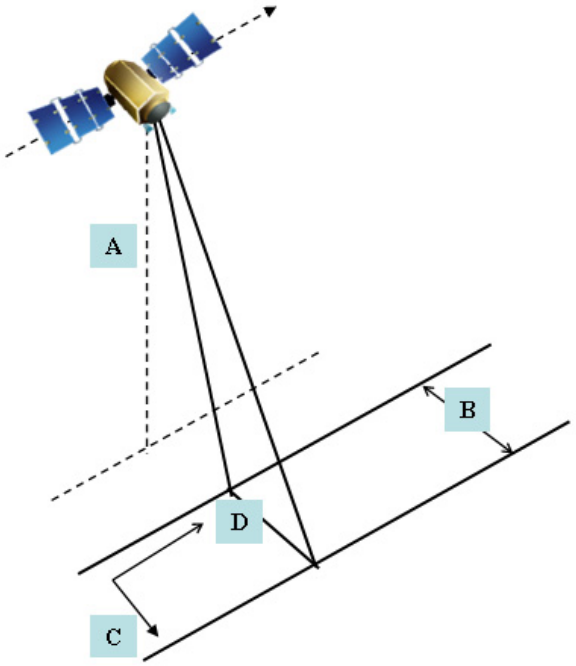

Figure 3. 2 SAR Geometry

For the radar to be able to distinguish two closely spaced elements, their echoes must necessarily be received at different times. As shown in Figure 3.3 (a), the pulse-width L is approaching targets T1 and T2. The slant range distance between the two targets is d. Since the radar pulse must travel round trip, the two targets lead to two distinguished echoes if $d > L/2$.

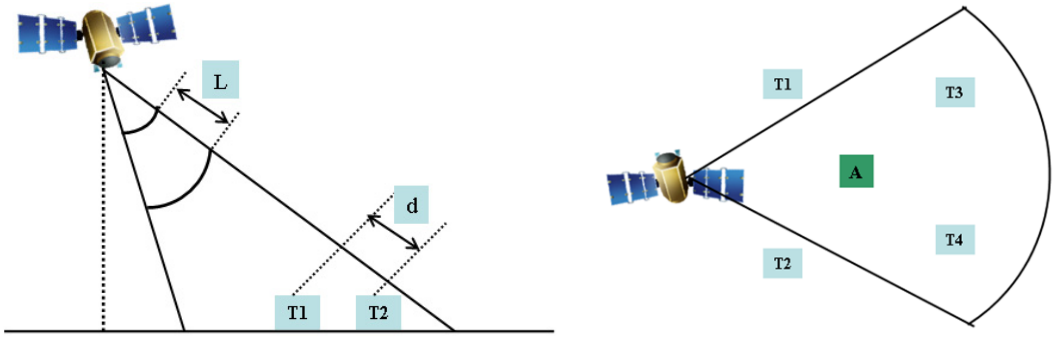

(a) (b)

Figure 3. 3 Illustration of SAR range resolution (a) and azimuth resolution (b)

The **range resolution** R_R can be expressed as the reciprocal of the effective pulse-width multiplied by the speed of light c,

$$R_R = \frac{c}{2L} \tag{3.1}$$

Azimuth resolution describes the ability of imaging radar to separate two closely spaced scatterers in the direction parallel to the motion vector of the sensor. Compared to the RAR, the prominent advantage of SAR is its ability to achieve high resolution in azimuth or along-track direction. In the following a brief explanation is given.

For real aperture radar, two targets in the azimuth or along-track resolution can be separated only if the distance between them is larger than the radar beam width (A) as demonstrated for T1 and T2 in Figure 3.3 (b). This beam width is a measurement of the width of the illumination pattern. As the radar illumination propagates to increasing distance from the sensor, the azimuth resolution becomes coarser thus the targets in the far range can not be distinguished correctly, as shown for T3 and T4 in the figure. Thus one can find that the beam width is taken as the azimuth resolution depending also slant-range distance to the target for these systems.

For a diffraction limited system of a given radar wavelength λ_R, the azimuth beam width β_A depends on the physical length L of the antenna in the horizontal direction according to:

$$\beta_A = \frac{\lambda_R}{L} \tag{3.2}$$

Therefore, for the targets in the (slant) distance R to the radar, the azimuth resolution for the RAR is given by,

$$R_{A\_RAR} = \beta_A R = \beta_A \frac{H}{\cos\theta} \tag{3.3}$$

in which H is the orbit height of radar and θ is local incidence angle.

The ERS-2 SAR has an azimuth resolution of 25 m, the orbit height is around 750 km, and incidence angle in the mid-swath is 23°. Considering the Equ.(3.2) and (3.3), one can find the size of antenna should be around 1 km for the RAR, which is impossible due to the size of spaceborne or airborne platforms. To achieve high resolution in azimuth direction, as well as to keep the antenna at small size, the concept of synthetic antenna or aperture was developed. The improved **azimuth resolution** is

$$R_{A\_SAR} = \frac{\lambda H}{2R_{A\_RAR}\cos\theta} = \frac{L}{2} \tag{3.4}$$

Thus the azimuth resolution is independent of spacecraft height and improves as the antenna length is reduced. Equ.(3.4) is the theoretical resolution of strip-mode SAR. One could form a longer synthetic aperture by steering the transmitted radar beam so it follows the target as the spacecraft (aircraft) flies by. This is called spotlight-mode SAR [*Carrar et al.*, 1995].

Achieving fine azimuth resolution may also be described from a Doppler processing viewpoint. A target's position along the flight path determines the Doppler frequency of its echoes: Targets ahead of the radar produce a positive Doppler offset; targets behind it produce a negative offset. As the satellite flies a distance (the synthetic aperture), echoes are resolved into a number of Doppler frequencies. The target's Doppler frequency determines its azimuth position.

3.3. SAR-Ocean surface interactions

This section will review SAR operation and geometry in the context of ocean imaging. Over the ocean, a SAR image consists of two-dimensional radar backscatter information of the roughness of the ocean surface. The backscattered radar energy depends on wavelength, polarization, geometry, attenuation by the atmosphere, and the roughness of the ocean surface.

The returned energy over sea surface is primarily scattered by the small wind induced surface waves. It is assumed that for moderate incident angles between 20° and 60º the Bragg resonance is the primary mechanism for SAR ocean surface imaging [*Plant*, 1990], i.e. the incident radar waves are backscattered by short

capillary wave components on the ocean surface, whose wave length λ_B, is related to radar wave frequency or wave length λ_R at an incident angle θ by,

$$\lambda_B = \lambda_R / 2\sin\theta \tag{3.5}$$

For X-band SAR with a wavelength λ_R of 3.1 cm, the resonant Bragg wave length is 3.9 cm at an incidence angle of θ=23°, while a SAR operated in C-band ($\lambda_R = 5.6$ cm) has a longer λ_B of 7.1 cm at the same incidence angle. This may lead to different radar signatures of the same oceanic or atmospheric phenomena as shown in simultaneous scenes acquired by multi-frequency SAR, e.g. SIR-C/X SAR.

The Bragg resonance may be assumed to apply locally, i.e. within a resolution cell. This is the reason for the two-scale model [*Hasselmann et al.*, 1985], where the ocean surface is divided into facets with the size of a resolution cell.

SAR images acquired over the ocean contain abundant information on small scale and mesoscale phenomena occurring in the ocean and the marine boundary layer. The following provides a short summary for the oceanic or atmospheric features that can be detected by a SAR.

- Surface wave characteristics – two dimensional wave spectrum, integral wave parameters, e.g. significant wave height, wavelength and wave direction.
- Near surface wind field (10 m height), wind speed and wind direction.
- Mesoscale and microscale atmospheric features – barrier jets, gap winds, storms, fronts, etc.
- Surface current using the Along-track interferometric (ATI) technique or by estimating the shift of the Doppler-centroid.
- Bathymetry
- Ocean mesoscale features – fronts, eddies, current boundaries, river plumes, upwelling.
- Internal waves and mixed layer depth estimates.
- Ship and oil spill detection

Mesoscale oceanic or atmospheric phenomena can be imaged by a single SAR image, particularly in ASAR wide swath mode of up to 350 km by 350 km. Figure 3.4 shows a TerraSAR StripMap image acquired over the Changjiang River in China on March 19, 2008. One can observe hundreds of ships in the river with visible ship

wakes. Low wind speed in the river region causes the low backscatter and manifests itself as dark region. The surface current is strong in the mouth of Changjiang River. In the North of the River, one can find dry mud flats as dark parts. In the South, Marine Atmospheric Boundary Layer information on roll vortices is also visible.

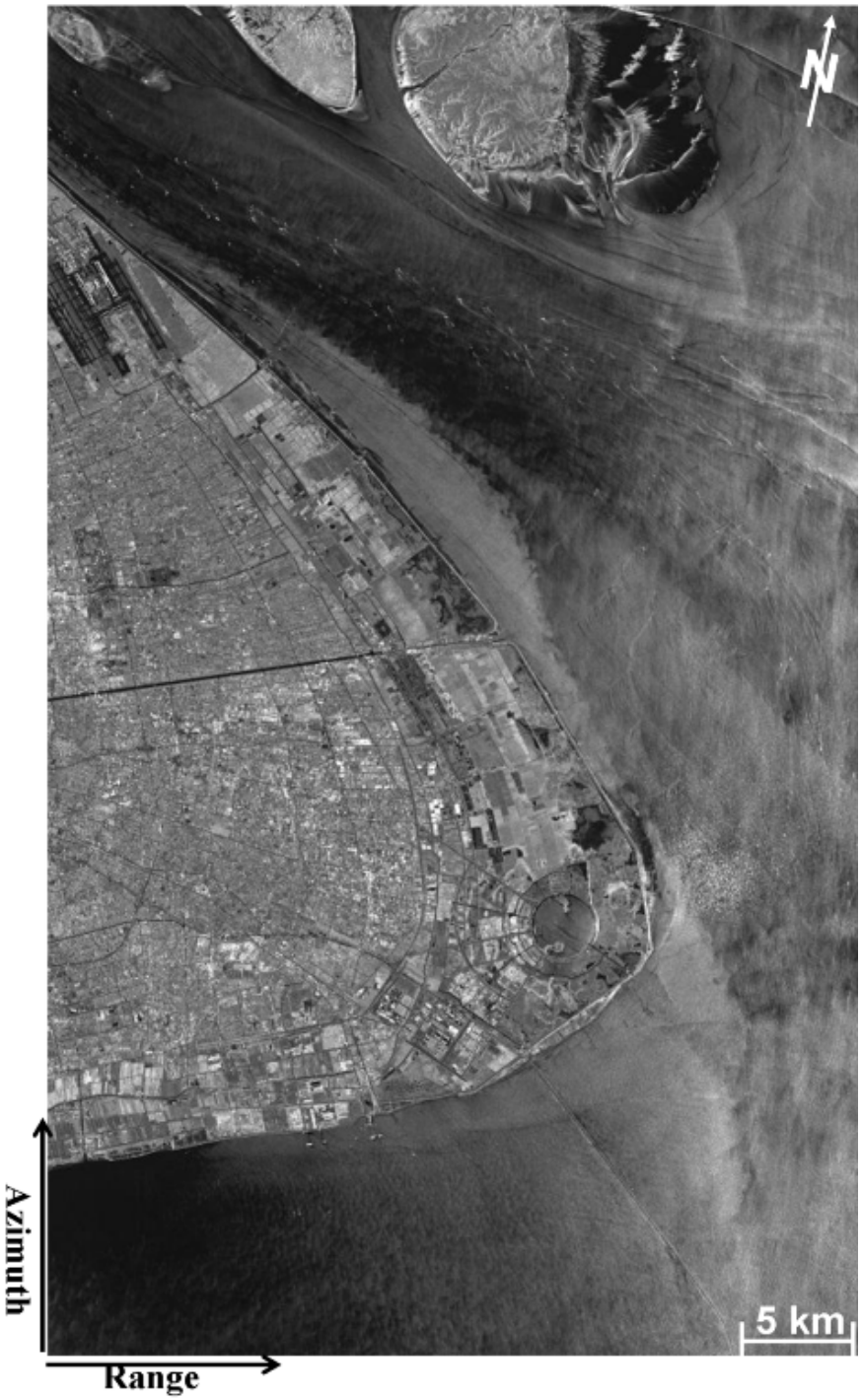

Figure 3. 4 TerraSAR-X StripMap mode image acquired over Changjiang River, China on Mar.19, 2008. Swath width is 30 km.

3.4. SAR Ocean wave imaging theory

In order to derive ocean wave characteristics from SAR images, it is important to understand how ocean waves are imaged by SAR. In this section, the SAR imaging of ocean waves is examined on the basis of the two-scale model.

The two-scale model [*Hasselmann et al.*, 1985] is used as the basic element to describe the SAR ocean wave imaging process, in which the short waves are responsible for the Bragg scattering mechanism. Detection of longer waves is possible through the modulation of these capillary waves by the longer ones. In the model the combined RAR and SAR radar cross section modulation is attributed to three effects: tilt modulation, hydrodynamic modulations and orbital motion effect. Tilt and hydrodynamic modulations are considered to be the dominant RAR modulation mechanisms [*Alpers*, 1981]. The long waves tilt the capillary waves so that the local incident angle is changed thus modifying the Bragg wavelength and the backscattered energy. The hydrodynamic interaction between the long waves and the capillary waves causes the divergence and convergence and thus modulate the energy returned.

SAR imaging of ocean waves has an additional source of modulation due to the orbital motion effect. This effect is often the dominant imaging mechanism for waves propagating in the azimuthal direction.

All the three mechanisms are shown schematically in Figure 3.5.

The RAR modulation dominates imaging of range traveling waves and is in general assumed to be a linear process and can be written using the linear transfer function T_k^R [*Hasselmann and Hasselmann*, 1991].

$$I^{RL} = \frac{\sigma_0(X,t) - \langle \sigma_0 \rangle}{\langle \sigma_0 \rangle} = 2\,\mathrm{Re}\left(\sum_k T_k^R \rho_r \exp\left[-i\left(\mathbf{KX} - \omega t \right) \right] \right) \tag{3.6}$$

The transfer function T_k^R can be expressed as the sum of the respective three modulations, i.e.

$$T_k^R = T_k^{titl} + T_k^{hydr} + T_k^{rb} \tag{3.7}$$

For VV polarization and a right looking SAR, the respective transfer functions for these modulations are given by the following:

$$T_k^{tilt} = -4ik_y \frac{\cot\theta}{1+\sin^2\theta} \tag{3.8}$$

$$T_k^{hydr} = 4.5\omega \frac{k_y^2(\omega - i\mu)}{|k|(\omega^2+\mu^2)} \tag{3.9}$$

$$T_k^{rb} = -ik_y \frac{\cos\theta}{\sin\theta} \tag{3.10}$$

With SAR right looking direction in negative k_y direction. θ is the incidence angle and μ is the hydrodynamic relaxation rate with value of 0.5 S^{-1} after [*Hasselmann and Hasselmann*, 1991].

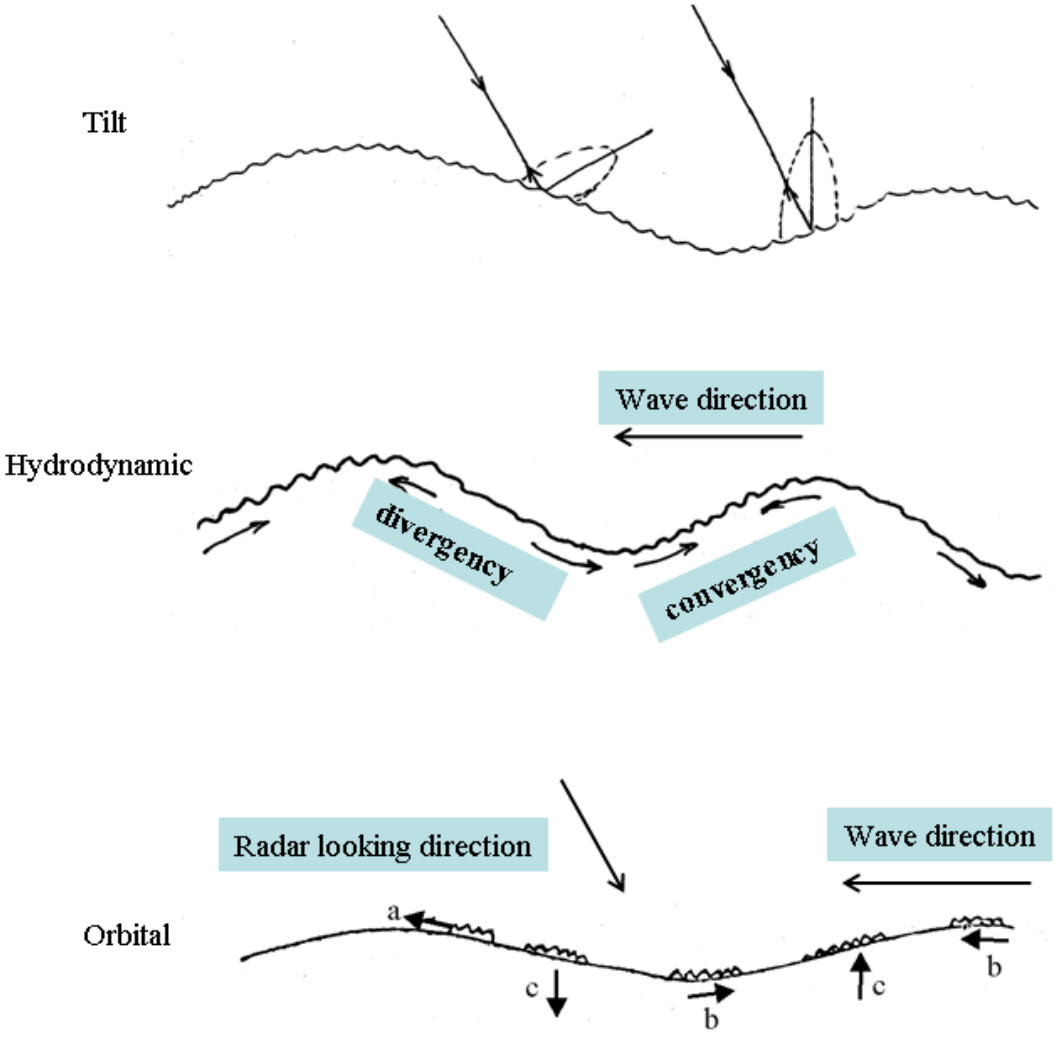

Figure 3. 5 The three modulation mechanisms for SAR imaging ocean wave

Tilt and hydrodynamic modulation are basically explained at the scatter level, assuming a frozen sea surface during the SAR coherent integration period. However for the motion associated with the traveling waves a frozen sea surface assumption is on longer valid.

In deep water, individual water particles follow a circular trajectory, therefore long waves have a periodic orbital motion (as shown in Figure 3.5, the third image, a, b and c demonstrate the motions), which will produce an apparent increase and decrease in the density of scatters.

Assuming the water circle has an orbital velocity component u_r (positive for direction towards the radar), then the effect of a facet having a constant radial velocity u_r induces an azimuthal shift ξ_x [*Lyzenga et al.*, 1985],

$$\xi_x = \beta \cdot u_r \tag{3.11}$$

where β is defined as ratio of slant range R to platform velocity V

$$\beta = R/V \tag{3.12}$$

This effect makes the azimuthally traveling waves detectable in a SAR image however there is a shift from their true position.

T_k^u is the orbital velocity transfer function, which is given by [*Hasselmann and Hasselmann*, 1991] for a right looking SAR as:

$$T_k^u = -\omega\left(\frac{k_y}{k}\sin\theta + i\cos\theta\right) \tag{3.13}$$

The orbit motion of long waves during SAR data acquisition time leads to a distortion of the image spectrum, as well as the cut-off effect in the azimuth direction [*Alpers and Brüning*, 1986], namely waves shorter than a certain threshold will not be imaged by SAR. In Fig. 3.6, left panel is the SAR image spectrum and the collocated numerical wave model spectrum is shown in right panel. Comparing the wave energy distribution in the region out of the dashed lines, one can observe that some short waves propagating in the SAR azimuthal direction are not imaged.

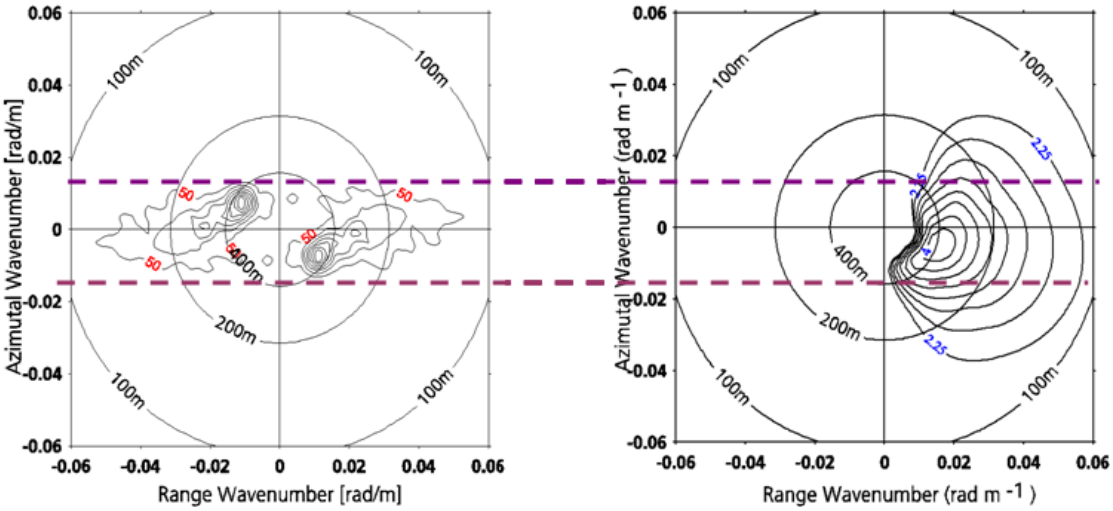

Figure 3. 6 Comparison of SAR image spectrum (left) to collocated numerical wave model WAM spectrum (right) to demonstrate the cut-off effect for wave propagation in SAR azimuthal direction

This low-pass filter effect is proportional to the value of β defined in Equ. (3.12) [*Beal et al.*, 1983]; also it is supposed to be dependent on other parameters, such as incidence angle, scene coherence time [*Milman et al.*, 1993], and geophysical parameters, for example, SWH [*Beal et al.*, 1983; *Milman et al.*, 1993] and mean wave period T_z. As pointed out as also by *Vachon et al.* [1994], the intrinsic scene coherence time is dependent upon surface wind speed U_{10}. It is believed that the SAR cut-off wavelength λ_c can be determined by the following function.

$$\lambda_C = F(\frac{R}{V}, \theta, H_s, T_z, U_{10}) \tag{3.14}$$

Different approaches, including empirical relationships, have been proposed to estimate the SAR cut-off wavelength, e.g. see [*Beal et al.*, 1983; *Monaldo*, 1994; *Kerbaol et al.,* 1998; *Schulz-Stellenfleth and Lehner*, 2002].

3.5. SAR ocean wave inversion algorithms

Some SAR ocean wave inversion schemes are based on the forward mapping function of wave spectrum into SAR image spectrum or cross spectrum. And the forward mapping relations are derived based on the SAR ocean wave imaging mechanisms. Following the introduction of SAR ocean wave imaging theory, in this section, the

current schemes to derive two-dimensional ocean wave spectra from SAR data are briefly summarized.

3.5.1. Linear and Non-linear Mapping of SAR Image Spectrum

The SAR surface wave imaging process can be regarded as the sum of RAR imaging process and orbital motion effect. Respective modulation transfer functions have been introduced in Equ. (3.7) and (3.13).

An integral transform relating the ocean wave spectrum F_k to the SAR cross spectrum of two looks I^i with separated time Δt is given by [*Engen and Johnsen*, 1995] in the following

$$\begin{aligned}\Phi_{I^1,I^2}^{\Delta t}(\mathbf{k}) = \frac{1}{4\pi^2}\exp(-k_x^2\beta^2 f^v(0))\cdot\int_{\mathbf{R}^2}\exp(-i\,\mathbf{kx})\exp\left(k_x^2\beta^2 f^v(\mathbf{x})\right)\cdot \\ \left\{1+f^R(\mathbf{x})+ik_x\beta\left(f^{Rv}(\mathbf{x})-f^{Rv}(-\mathbf{x})\right)+\right. \\ \left. k_x^2\beta^2\left[f^{Rv}(\mathbf{x})-f^{Rv}(0)\right]\left[f^{Rv}(-\mathbf{x})-f^{Rv}(0)\right]\right\}d^2\,\mathbf{x}\end{aligned} \tag{3.15}$$

In which, $\Phi_{I^1,I^2}^{\Delta t}$ denotes the cross spectrum estimated from the normalized two looks of SAR complex data, which is defined as Fourier spectrum of the cross-covariance function $\rho^{I1,I2}$,

$$\Phi_{I^1,I^2}^{\Delta t} = \mathbf{F}\left(\rho^{I1,I2}\right) \tag{3.16}$$

Here β is defined in equation (3.12), k_x is the azimuth wave number component and the cross-covariance functions f^v, f^{Rv}, f^R are defined as follows.

$$\begin{aligned}f^R(\mathbf{x}) &= 0.5\int_{\mathbf{R}^2}\left(F(\mathbf{k})\cdot\left|T_k^R\right|^2\exp(i\omega\Delta t)+F(\text{-k})\cdot\left|T_{-k}^R\right|^2\exp(-i\omega\Delta t)\right)\exp(i\,\mathbf{kx})\,d^2\,\mathbf{k} \\ f^{Rv}(\mathbf{x}) &= 0.5\int_{\mathbf{R}^2}\left(F(\mathbf{k})\cdot T_k^R\left(T_k^v\right)^*\exp(i\omega\Delta t)+F(\text{-k})\cdot T_{-k}^R\left(T_{-k}^v\right)^*\exp(-i\omega\Delta t)\right)\exp(i\,\mathbf{kx})\,d^2\,\mathbf{k} \\ f^v(\mathbf{x}) &= 0.5\int_{\mathbf{R}^2}\left(F(\mathbf{k})\cdot\left|T_k^v\right|^2\exp(i\omega\Delta t)+F(\text{-k})\cdot\left|T_{-k}^v\right|^2\exp(-i\omega\Delta t)\right)\exp(i\,\mathbf{kx})\,d^2\,\mathbf{k}\end{aligned} \tag{3.17}$$

Expanding the transform of Equ.(3.15) to first order with respect to the wave spectrum F_k yields the linear approximation as introduced by [*Hasselmann and Hasselmann*, 1991].

$$\Phi_{I^1,I^2}^{\Delta t}(\mathbf{k}) \approx 0.5\left(\left|T_k^S\right|^2 \exp(i\omega\Delta t) F_k + \left|T_{-k}^S\right|^2 \exp(-i\omega\Delta t) F_{-k}\right) \tag{3.18}$$

The SAR transfer function T^S is given by

$$T_k^S = T_k^R + i\frac{R}{V} k_x T_k^u \tag{3.19}$$

T^R is given via (3.8)-(3.10) and T^u is given in (3.13).

If one expands only the integral part of (3.15) to linear order and keeps the leading exponential factor this yields the quasi-linear transform given by

$$\Phi_{I^1,I^2}^{\Delta t}(\mathbf{k}) \approx 0.5 \exp\left[-k_x^2 \beta^2 f^v(0)\right]\left(\left|T_k^S\right|^2 \exp(i\omega\Delta t) F_k + \left|T_{-k}^S\right|^2 \exp(-i\omega\Delta t) F_{-k}\right) \tag{3.20}$$

The quasi-linear forward model is helpful as it yields a simple transform to retrieve the two-dimensional ocean wave spectrum from SAR cross spectrum. The quasi-linear relationship is the basis for the cross spectral scheme adopted by ESA for developing ASAR wave mode level2 WVW products [*Engen et al.*, 2001].

3.5.2. Algorithms of ocean wave spectrum retrieval from SAR data

The general non-linear transformation relating the SAR image spectrum or cross spectrum to the ocean wave spectrum is given in the previous section. Several retrieval algorithms to derive the two-dimensional ocean wave spectrum or integral wave parameters from SAR data have been developed. A short summary for the current algorithms are given in the following.

Nonlinear retrieval approach - - MPI and PARSA

The mechanism of SAR imaging of ocean surface gravity waves generally consist of the linear transformation of tilt and hydrodynamic modulation, as well as the non-linear distortion induced by the radial wave motions [*Hasselmann et al.*, 1985]. This leads, among other effects, to image smearing and to a loss of information beyond the so-called azimuth cut-off wavelength [*Alpers and Brüning*, 1986]. For ERS and ENVISAT SAR, this corresponds typically to wavelengths shorter than about 200 m in the along track direction. In addition, ocean wave spectra from satellite SAR images suffer from a basic 180^o ambiguity of wave propagation direction, which can

be resolved by using complex data [*Engen and Johnson*, 1995]. A nonlinear mapping of ocean wave spectra into SAR image spectra as well as its inversion was developed by *Hasselmann and Hasselmann* [1991] and is referred to as MPI scheme in the following**.** This inversion algorithm accomplishes the retrieval of ocean wave spectra from SAR spectra within the computational constraints of real-time operational applications (see also [*Krogstad*, 1992] for a simpler transform). An assessment of the performance of the algorithm as well as the operational feasibility was given by *Heimbach et al.*, [1998] using three years (1993-1995) ERS-1 SAR wave mode UWA spectral data (i.e. SAR image spectrum, see [*Brooker*, 1995]). Validation results show that approximately 75% of the available SAR wave mode spectral data were converted into successful retrievals. There remains a small overestimation less than 0.5 m for retrieved SWH by the MPI scheme compared to the results from WAM model.

A semi-parametric algorithm was developed as well for full ocean wave spectrum retrieval from SAR by taking the ERS SAR wave mode image spectra and collocated wind vectors from ERS wind scatterometer into account as additional input [*Mastenbroek and de Valk*, 1998]. The algorithm could not be used for the ENVISAT mission where the scatterometer is not onboard.

A parametric inversion scheme for the derivation of two-dimensional ocean wave spectra from SAR look cross spectra is presented by *Schulz-Stellenfleth et al.* [2005] and is referred to as the PARSA algorithm. This algorithm needs priori information from a numerical wave model as well, while by using the complex information of SAR data to resolve the ambiguity on wave propagation direction.

SAR cross spectral algorithm

Taking two looks of SAR wave mode complex data, the cross spectra can be used to remove the 180º ambiguity of ocean wave propagation direction [*Engen and Johnson*, 1995], which was demonstrated for airborne C-band SAR data. Furthermore, the algorithm was extended to the spaceborne ERS-2 SAR reprocessed wave mode data by *Lehner et al.* [2000].

This method has been adopted by ESA for the ASAR wave mode data, the so called WVW Level2 products WVW [*ENVISAT Handbook*, 2007]. Ocean wave

spectra of the WVW products only yield information in the inner spectral bins [*Abadalla et al.*, 2008] contained in the ASAR wave mode data.

To some extent, the PARSA algorithm introduced above is the combination of the nonlinear approach and the cross spectral algorithm. It uses the cross spectrum of SAR two looks to remove the 180º ambiguity and blends the SAR image spectra and first priori information from a wave model.

Intercomparison and validation for PARSA and WVW algorithms are described in Chapter 6 in detail.

Empirical algorithm - - CWAVE

For the current non-linear or quasi-linear algorithms retrieving two-dimensional ocean wave spectra from SAR imagery, either a priori information from a numerical wave model is needed, e.g., for the MPI or PARSA scheme as used at weather forecast centers where a first guess is available. Otherwise the information provided on wave height is limited to parts of the spectrum for waves longer than a certain threshold.

Here a new approach using an empirical algorithm is given to derive ocean wave integral parameters, e.g., SWH and mean wave period, instead of the full two-dimensional spectra, while without needing priori information. For the ERS mission, the empirical algorithm CWAVE_ERS [*Schulz-Stellenfleth et al.*, 2007] was proposed for the reprocessed ERS-2 SAR wave model data [*Lehner et al.*, 2000]. Validation results show that the performance of CWAVE _ERS is fairly good when compared to the ECMWF WAM model using 6000 collocated data pairs and to 21 buoy measurements during three weeks in 1996. For both comparisons with respect to SWH, results of CWAVE_ERS showed the RMS is to be 0.44 m and 0.39 m, respectively. However CWAVE_ERS has not been validated for high sea state, e.g., SWH higher than 6 m. In the frame of this thesis, a new algorithm for ENVISAT ASAR wave mode data was developed.

In this thesis, as well, wave measurements of ERS-2 SAR wave mode data using PARSA and CWAVE_ENV algorithms are cross validated as demonstrated in Chapter 5.

Chapter 4

Dataset Description

In this chapter, the datasets used in the present study are introduced briefly. Tab.4.1 lists the used active microwave data, numerical wave model data and in situ buoy data.

Table 4. 1 Datasets used in the present study

Type	Name	Source
Active microwave	SAR wave mode (ERS-2 SAR and ENVISAT ASAR)	ESA, DLR
Active microwave	Radar Altimeter	RADS, TU Delft CERSAT
Numerical wave model	ECMWF reanalysis wave model DWD forecast wave model	ECMWF DWD
In situ	Meteorological buoy	NDBC and MEDS

ERS-2 SAR and ENVISAT ASAR wave mode data are the main data source, which are used for SAR ocean wave algorithm development and validation. The radar altimeter is used for validating the SWH retrieved from SAR image and wave model results.

On the ENVISAT platform both the ASAR sensor and the RA-2 are onboard and they are jointly used for global wave measurements.

4.1. SAR wave mode data

ERS-1/2 and ENVISAT acquire SAR wave mode data every 200 or 100 km along the satellite track as so called imagettes with approximately 5 km x 10 km size, when image mode data (typical swath size is 100 km by 100 km) is not requested.

ERS-2 SAR wave mode data

The standard ERS-2 SAR wave mode data are acquired over the ocean every 200 km

along the satellite track with coverage of 5 km x 10 km. It operates at C Band with 23.5º incidence angle and VV polarization. The spatial resolution of wave mode data is 10 m in azimuth and 20 m in ground range. UWA spectra are the standard ESA fast delivery product [*Brooker*, 1995] for wave mode data during the ERS era. UWA spectra are coarsely gridded image power spectra derived from imagettes with a directional resolution of 15º and 10 wavenumber bins logarithmically spaced between 66–660 m as an example shown in Fig. 4.1. The complex imagettes themselves are so far not available from ESA as a standard product, while delivering them is under consideration.

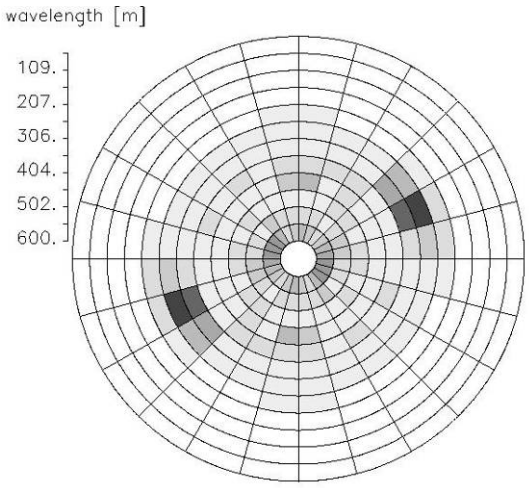

Figure 4. 1 An example of standard ERS-2 SAR wave mode product- UWA spectrum

Two-year ERS-2 wave mode raw data acquired during 1998 and 2000 were processed to SLC imagettes using the BSAR processor [*Breit et al*., 1997]. Four examples of ocean surface wave imaged by ERS-2 SAR wave mode are shown in Fig.4.2. Upper left represents the extreme sea state; upper right shows long swell travelling in azimuth direction; lower left is a cross sea case and an example of ocean wave travelling into ice zone is shown in lower right.

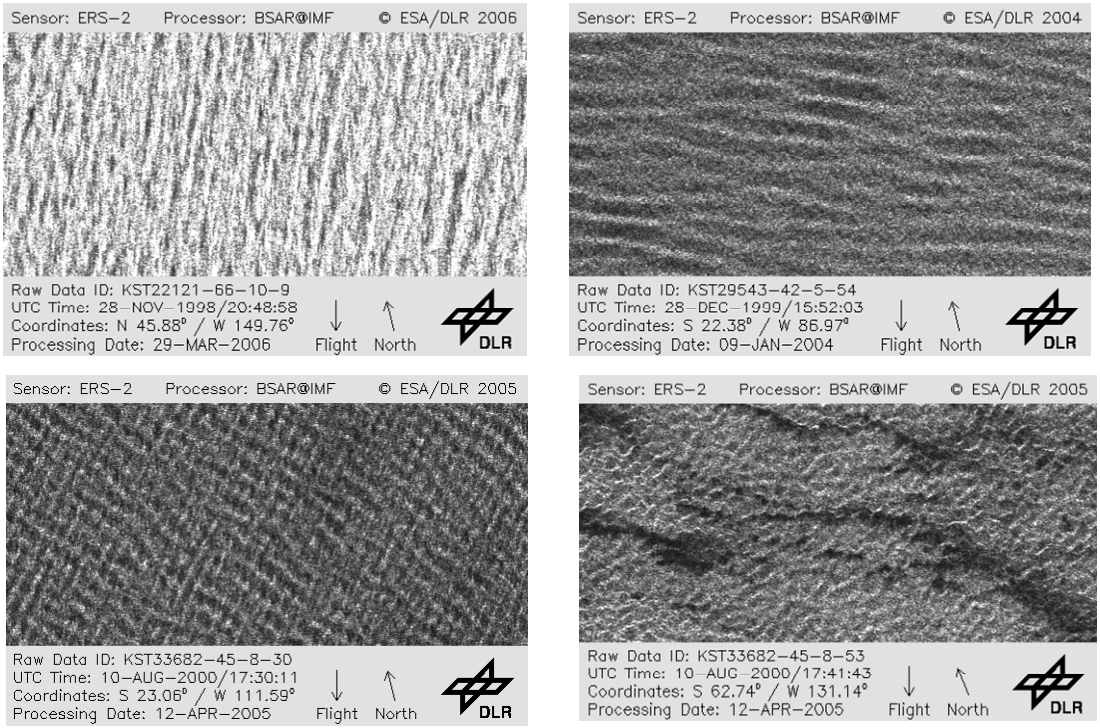

Figure 4. 2 Examples of surface waves imaged by the reprocessed ERS-2 SAR wave mode

ENVISAT ASAR wave mode data

As the successor of ERS/SAR, ASAR onboard ENVISAT also collects wave mode data to form small images (imagettes) of 5 km x 10 km size while every 100 km along the satellite's orbit. Unlike for ERS, where only the SAR image spectra of wave mode data are provided, ESA generates different ENVISAT ASAR wave mode products from the respective raw data. In particular the level-1b (ASA_WVI_1P, for wave mode complex data and ASA_WVS_1P, for cross spectra derived from these complex data) and level-2 products (ASA_WVW_2P, the so called retrieved ocean wave spectra) are relevant for the present study.

4.2. Radar altimeter data

For more than thirty years, spaceborne radar altimetry including Seasat (1978), Geosat (1985–1988), ERS–1 (1991–1996), ERS–2 (1995–), Topex/Poseidon (1992–2006), Jason (2002–), and Envisat (2002-) have created a wealth of space data for earth observation.

The radar altimeter is a nadir-viewing active microwave sensor operating at the

main frequency of Ku-band (13.575 GHz), which makes measurements of the delay time and power of the return signal. Details of the principles of radar altimeter sea surface measurements are given in Appendix 1.

These measurements are directly related to the range to the target, its radar backscatter coefficients and the surface roughness. The spatial resolution (footprint) of radar altimeters onboard on ERS-2 and ENVISAT are both 16-20 km and the measurements are performed about every second with about 7 km spacing. In the present study, RA data onboard ERS and ENVISAT (RA-2) operating in Ku-band is used for ocean surface wave observations, i.e. SWH measurements. RA data is acquired via the TuDelft Radar Altimeter Database System (RADS) freely [http://rads.tudelft.nl/rads/; *Schrama et al.,* 2000; *Naeije et al*., 2002]. It needs to be pointed out that ESA normally provides the RA or RA-2 in Fast Delivery Products (FDP) to the users in real time. However, in some research centres, upgraded level products are processed from the RA raw data using different algorithms and therefore the performance of the upgraded products is slightly different.

ASAR and RA-2 are both active microwave sensors onboard ENVISAT, which can provide the synergy sea surface measurements at a distance of around 300 km. Fig. 4.3 illuminates a typical daily coverage of the both tracks, i.e. ASAR wave mode and RA-2 tracks over the ocean. The grey line shows the orbit of ASAR sensor, which are always to the right side of RA-2 tracks.

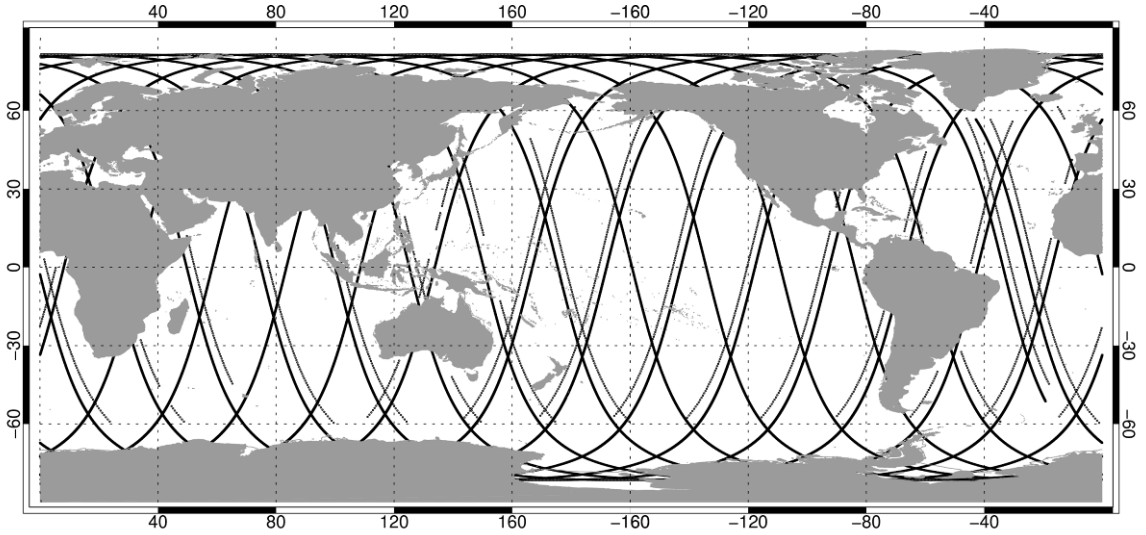

Figure 4. 3 An example of global ENVISAT ASAR wave mode tracks (grey line) and RA-2 tracks (dark line on the left side of ASAR tracks) during one day

4.3. Numerical wave model data

In the present study, numerical wave model data run at weather centers, e.g. ECMWF and DWD are used. The reanalysis wave model at ECMWF generally is assimilated with satellite information, e.g., radar altimeter and SAR, and some *in situ* buoy measurements. While for both reanalysis and forecast numerical wave model, the input forcing of wind field from scatterometer measurements has been assimilated.

Details for the numerical wave model used are described in Appendix 2.

4.4. *In situ* buoy measurements

Fig. 4.4 shows the geographical position of 77 moored buoys used for the present study. Most of the buoys are maintained by the NOAA National Data Buoy Center (NDBC) and the Environment Canada Marine Environmental Data Service (MEDS).

Non-directional buoys measure the sea surface vertical acceleration, which is then used to derive surface displacement spectra. Data collection and analysis procedure for the NDBC non-directional wave buoys were described in detail by [*Steele and Earle*, 1979]. Generally, in each hour a 20-minute record of vertical hull accelerations of the buoy, sampled at a rate of 1Hz, is collected. By applying a segmented Fast Fourier Transformation (FFT) for the record, an acceleration spectrum is calculated from which the non-directional wave spectrum $S(f)$, i.e., frequency spectrum, is obtained.

Integral wave parameter, e.g. SWH, can be estimated from the frequency spectrum $S(f)$ using a limited frequency interval.

$$Hs = 4\left[\int_{f_0}^{f_1} S(f)df\right]^{1/2} \tag{4.1}$$

The frequencies usually range from 0.03 to 0.40 Hz at intervals of 0.01 Hz.

Name, latitude and longitude of the buoy stations as shown in Fig. 4.4 are given in Appendix 3.

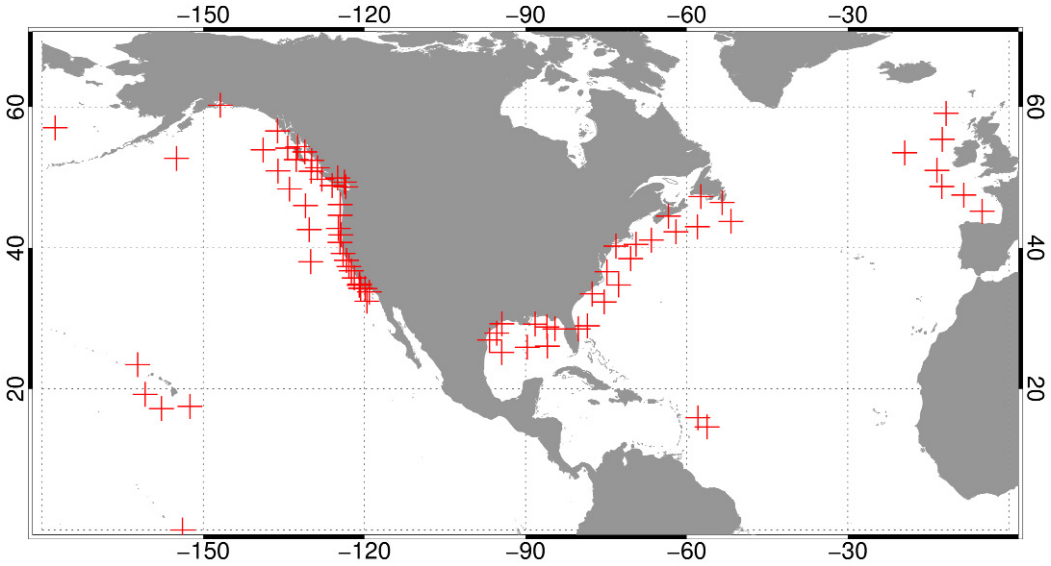

Figure 4. 4 Location of collocated buoys for CWAVE_ENV model validation

Chapter 5

Investigation of Cross Sea Using ERS-2 SAR Wave Mode Data

I started the investigation of SAR surface wave measurements with the based on a cross sea case that occurred in the South Pacific.

The content of the Chapter is based on the following publication:
Li, Xiao-Ming; Lehner, Susanne; He, Ming-Xia (2008): **Ocean wave measurements based on satellite synthetic aperture radar (SAR) and numerical wave model (WAM) data - extreme sea state and cross sea analysis**. *International Journal of Remote Sensing*, **29** (21), S. 6403 - 6416, DOI: 10.1080/01431160802175546

Two types of ocean waves usually characterize the sea surface, namely wind sea and swell. The first refers to waves influenced by the local wind, the latter to waves that have propagated out of the generating area and are thus no longer affected by the local wind. A sea state with two wave systems traveling at oblique angles is called cross sea. In the present study, such a case, which occurred in the South East Pacific, was analyzed by using ERS-2 SAR reprocessed wave mode images.

Here only the main conclusions and plots are presented.

The case is studied using two-dimensional spectra, including the WAM model spectra, cross spectra derived from complex SAR data and the non-linear retrieved PARSA spectra [Schulz-Stellenfleth *et al*., 2005].

In Fig. 5.1, the measurements and model results are summarized for three consecutive imagettes. The most distinct peaks can be observed on the image shown rightmost of first row in figure 5.1, which is situated at 23.06°S and 111.6°W degrees. The hindcast WAM model spectra (second row), observed SAR cross spectra (third row) with ambiguity of wave propagation direction removed by using the imaginary part of the cross spectra and nonlinear retrieved PARSA spectra (lower row) are shown as well. It is clear from these contour plots that the cross sea contains two distinct swell systems propagation to northeast and to northwest. These are denoted as

S_{ne} and S_{nw} respectively. The generation and propagation of the two swells are demonstrated in Figure 5. 2.

For the S_{nw} swell system, it is observed from the SAR cross spectra and retrieved PARSA spectra that the peak energy is underestimated by the WAM model. One explanation is that the input wind field from ERA-40 at the generation area of the swell was too weak. This can be concluded as well from comparison to the QuikSCAT wind field (acquired on August 8, 2000 at around 12: 30 UTC) in Fig. 5.3. The maximum wind speed measured by QuikSCAT is about 30 m/s, which is substantially larger than the ERA-40 model result given to be 20m/s. Thus validation of the ocean wave model results can be used as a joint validation tool for the wind field.

Fig. 5.4 shows nine SAR imagettes acquired during 17:28 to17:32 UTC on August 8, 2000, along the orbit (North to South) demonstrated as squares in Fig. 5.2. The feature of the cross sea increases from north to south and reaches the most distinct two swell systems in the imagettes represented as the yellow square in Fig. 5.2. By a spectral partitioning method, the PARSA retrieved SWH of two distinct swells are calculated respectively and marked as well in Fig. 5.4. The PARSA retrieved swell SWH and the WAM model result against swell traveling distance from the source is shown in Fig. 5.5.

It is observed from the imagettes that the swell S_{nw} dissipated gradually and the feature of cross sea vanishes along the SAR descending orbit from north to south. In Fig. 5.5 (left), it can be seen that the individual swell SWH decreases from north to south along the track and the results both from the PARSA and the WAM model are fairly low. There is a slight difference between them lower than 0.5 m.

The swell S_{ne} has the reverse trend compared to the swell S_{nw}, i.e. the swell SWH increases from North to South (nearer to the centre of the generation source) as shown in the right plot in Fig. 5.5.

At the most distinct cross sea feature observed by the SAR imagette acquired at 17:30 UTC, the swell SWH behaviour changes for both swell systems. In the right plot in Fig. 5.5, it can be found that after the turning point, swell SWH retrieved from PARSA decreases significantly compared to the WAM results. Thus in a first assessment a stronger damping than expected by the wave model is observed in the SAR data due to interaction with a second wave system.

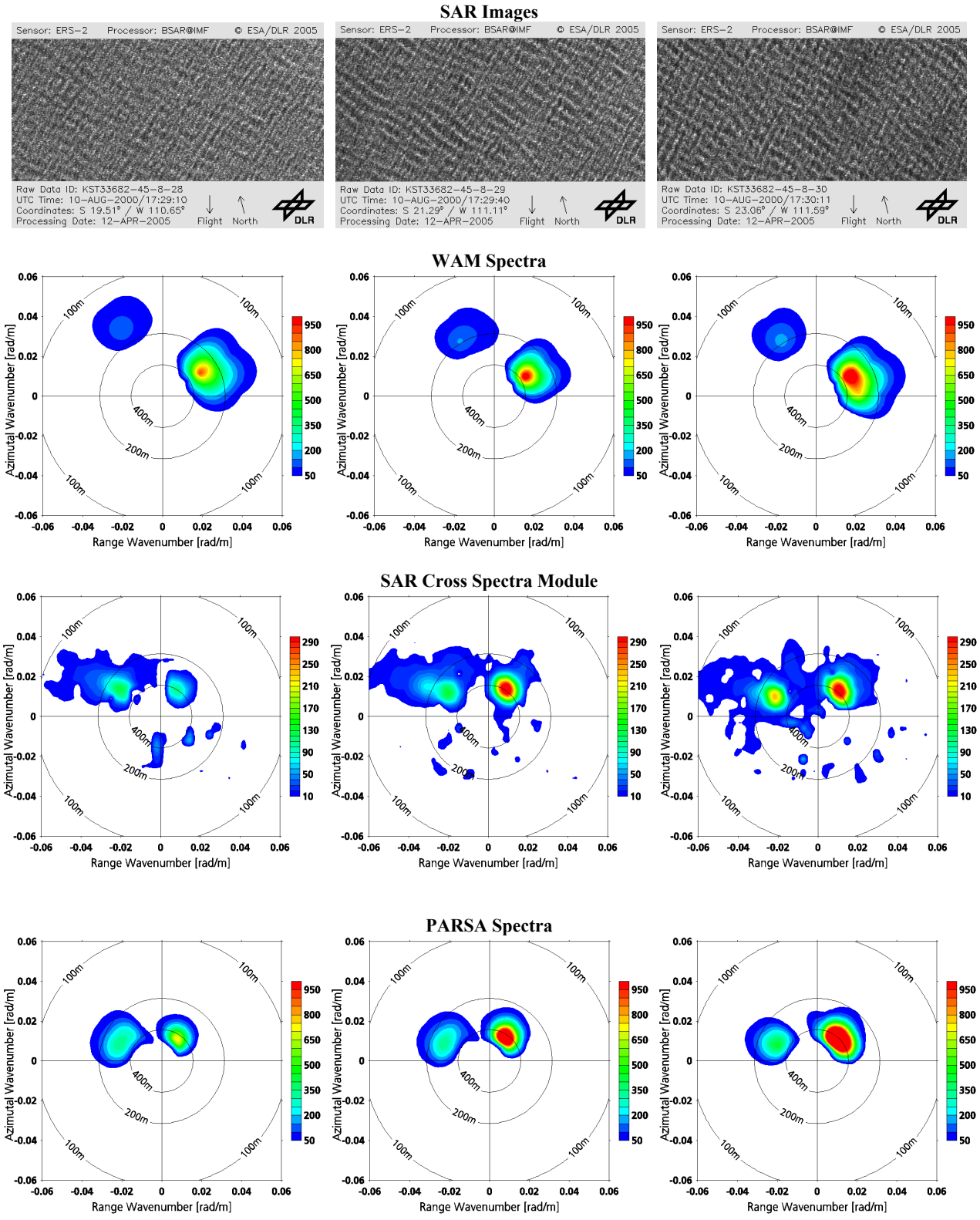

Figure 5. 1 SAR Imagettes, WAM Model spectra (m^4), SAR cross spectra (m^2), PARSA retrieved spectra (m^4) for the cross sea case

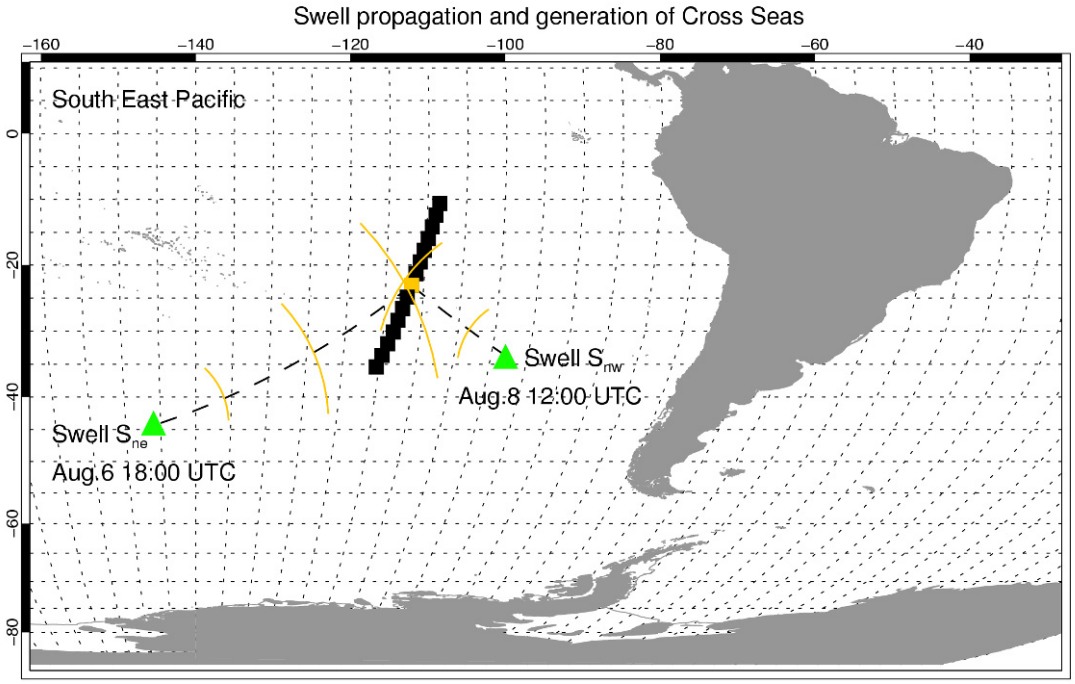

Figure 5. 2 Sketch map of the cross sea generation

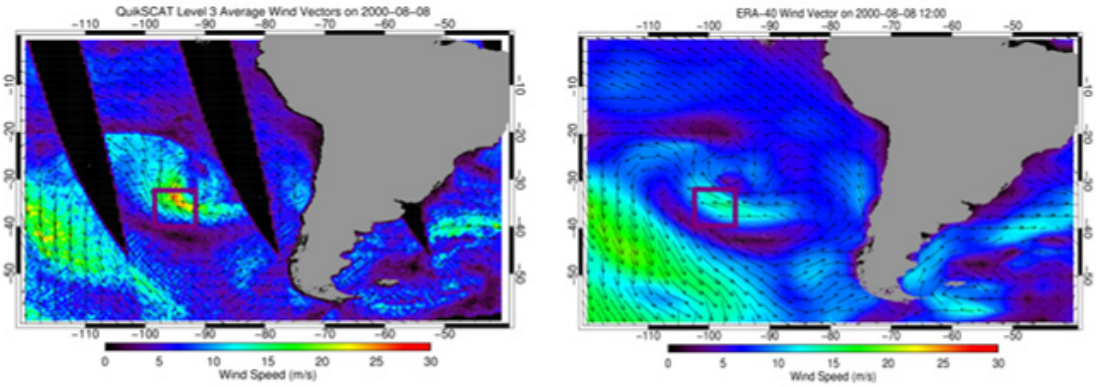

Figure 5. 3 ERA-40 (right) and Quikscat (left) wind fields over the generation area for the swell traveling to northwest (S_{nw})

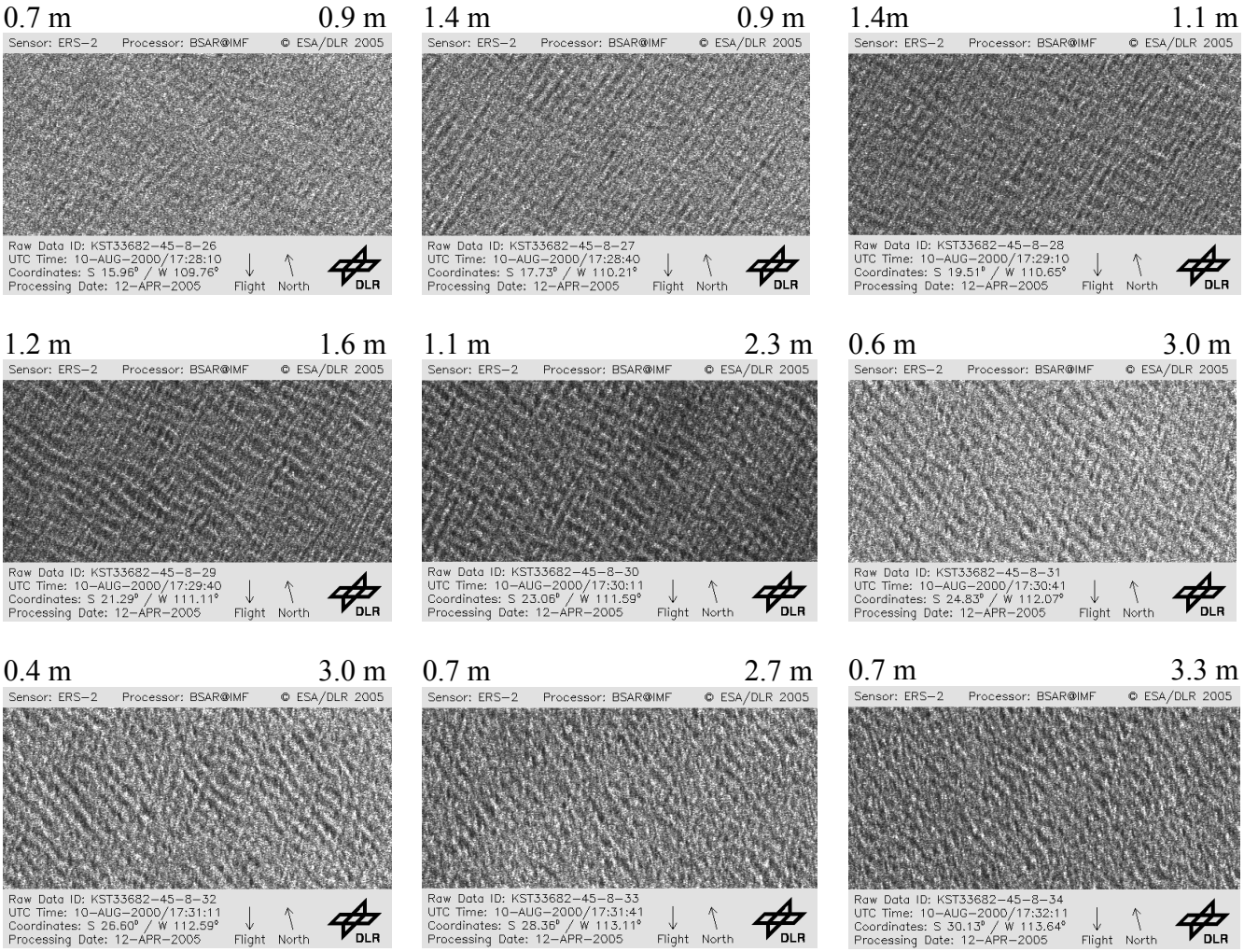

Figure 5. 4 SAR imagettes shown as squares in Fig. 5.2.

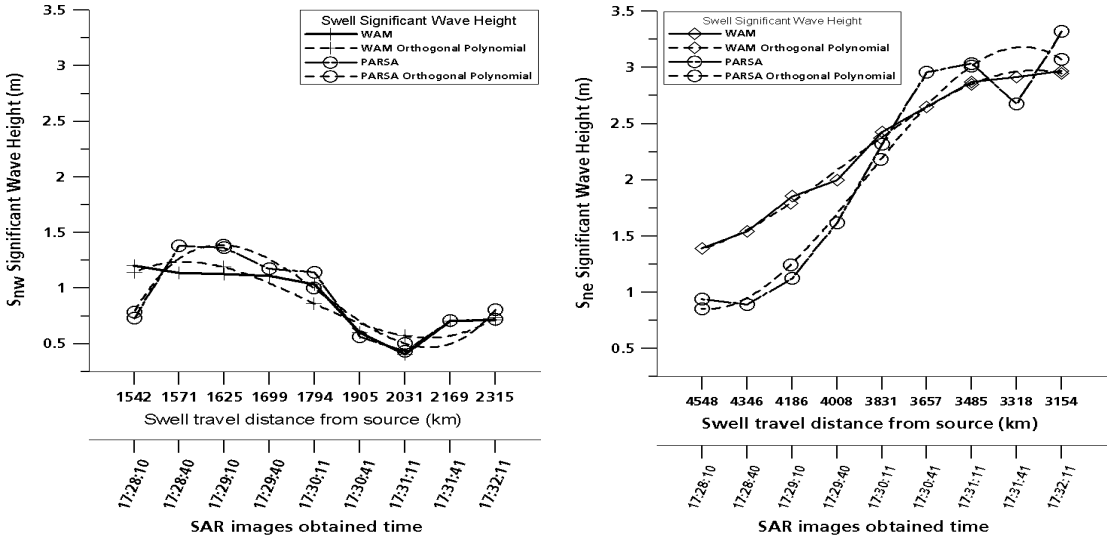

Figure 5. 5 Swell SWH against propagating distance comparison for the swell S_{ne} (right) and S_{nw} (left)

Summary

A cross sea case is observed on at least eight consecutive imagettes, i.e. over a distance of more than 1000 km. The comparison among WAM model spectra, cross spectra and PARSA nonlinear inverted spectra is demonstrated. The generation area of the swell systems is determined. It is shown that as derived from the SAR wave measurements, the wind field in the generation area was too weak in the ERA-40 model.

Finally, swell dissipation is studied based on the comparison of SWH (derived from the retrieved and the model results) versus swell propagation distance. Although the PARSA retrieval scheme needs first guess information from the WAM model, the difference of wave model and SAR measurements along the orbit shows that the model results are consistently low after crossing of the two swell systems. Investigating the different behaviour of the WAM model and the SAR measurements, it can be shown that the swell systems affect each other, thus leading to a strong wave damping.

This research shows the wave damping effect after crossing of two swell systems.

Chapter 6

Validation and Intercomparison of Ocean Wave Spectra Retrieval Schemes Using ASAR Wave Mode Data

As a next step, the existing SAR ocean wave retrieval algorithms from ESA and developed at DLR were investigated and validated. The content of this Chapter is based on the paper:

Li, Xiao-Ming; König, Thomas; Schulz-Stellenfleth, Johannes; and Lehner, Susanne (2009), "**Validation and intercomparison of ocean wave spectra retrieval scheme using ASAR wave mode data**," submitted to *International Journal of Remote Sensing*.

In this chapter, validation of the non-linear Partition Rescaling and Shift Algorithm (PARSA) for deriving two-dimensional ocean wave spectra from ASAR wave mode data is presented. Intercomparison of the PARSA algorithm to the quasi-linear retrieval algorithm adopted by ESA for ASAR wave mode Level-2 WVW products are analyzed as well in this chapter.

Both schemes make use of the cross spectrum calculated from ASAR wave mode complex data as input. The forward mapping function of wave spectrum into SAR image spectrum or the cross spectrum, as well as the general descriptions for the inversion schemes have been already introduced in Chapter 3.

At first the theoretical models for PARSA and WVW schemes are presented.

6.1. Inversion scheme of PARSA

The PARSA scheme [*Schulz-Stellenfleth et al.* 2005] is proposed to derive complete two-dimensional ocean wave spectra from SAR wave mode data with priori information obtained from numerical wave model, e.g., WAM [WAMDI Group, 1988]. Thus the retrieved results present the best available estimation making use of both SAR and wave model information, which is not only essential for practical

applications in marine design, but is also important for the understanding of ocean wave physics, as well for the assimilation of numerical wave forecast models. The scheme is available for reprocessed ERS-2 SAR and ENVISAT ASAR wave mode data and is also suitable for the future Sentinel-1 mission of ESA.

The PARSA inversion scheme needs priori information from a numerical wave model while using complex information from SAR data to resolve the ambiguity on wave propagation direction.

SAR Cross Spectra

A SAR requires a finite period of time, in the order of 1 second e.g. for C-band SARs, to collect data from the synthetic aperture. As such, individual looks can be extracted from Doppler spectrum during the integration time or aperture synthesizing period. The waves propagate during this period and therefore by taking advantage of the offset during different looks, the 180° ambiguity of ocean wave propagation direction can be removed as investigated in, e.g., [*Engen and Johnsen*, 1995; *Lehner et al.*, 2000].

The SAR cross spectrum $\Phi_{I^1,I^2}^{\Delta t}$ is defined as the Fourier spectrum of the cross covariance function ρ_{I^1,I^2} of two SAR looks with separation time Δt.

$$\Phi_{I^1,I^2}^{\Delta t} = \mathbf{F}\left(\rho^{I^1,I^2}\right) \tag{6.1}$$

The cross spectrum is a complex valued function with symmetric real and anti-symmetric imaginary part. The positive peaks of the imaginary part indicate the propagation direction of the waves.

Two individual looks derived from one ERS-2 SAR wave mode image acquired on Nov.28th, 1998 over the North Pacific storm [*Li et al.* 2009] are shown in Fig. 6.1 (a) and (b). The real part and imaginary part of the cross spectrum computed from the two looks are presented in (c) and (d) respectively. The negative value in the imaginary part is marked by blue lines. The black line for the positive value indicates the propagation direction of the ocean wave system. Two wave systems with wavelength of around 300 m and 420 m are observed in the cross spectrum, indicating a mixed sea state consisting of long swells and fully developed wind sea.

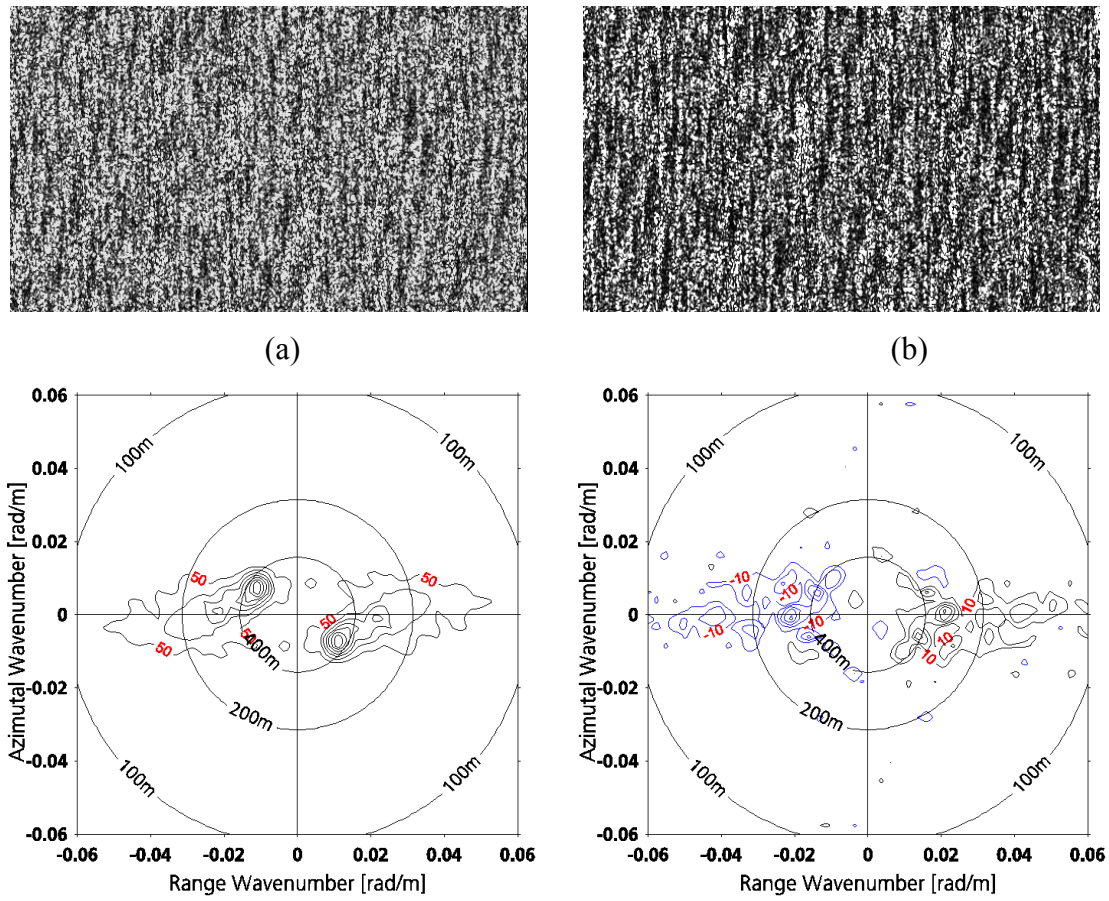

Figure 6. 1 (a) and (b) for two individual looks of one ERS-2 SAR wave mode data acquired on Nov.28th, 1998 over the North Pacific storm. Real part (c) and imaginary part (d) of the cross spectrum are computed from the two looks.

Comparison to the MPI scheme, PARSA has several additional features:

- Three parameters are used for wavelength, wave height and propagation direction in different wave systems. An additional description of the directional spreading of wave systems is included as well.
- The algorithm is based on explicit models for the measurement error, errors in the forward mapping model, and uncertainties in the priori wave spectrum.

Measurement errors:

The following model is used in the PARSA approach for derivation between simulated and observed cross spectrum due to errors in the SAR imaging model.

$$\Phi_k^{obs} = \alpha_1 \exp\left[-k_x^2 \alpha_2\right] \Phi_k^{sim} + \varepsilon_k^F \tag{6.2}$$

α_1 describes errors in the overall energy level of the spectrum. α_2 describes uncertainties in the SAR ocean wave forward model and ε^F is regarded as the error due to the estimation of SAR cross spectrum.

Uncertainties in the priori wave spectrum:

The approach uses the SAR information to adjust the parameters like wavelength, wave height, propagation direction and directional spreading in the priori spectrum F_k from numerical wave model, e.g., the WAM model.

Considering F_k can be split into n_p different sub wave systems S^i using a partitioning scheme, for each sub wave system a stochastic model with vector $(X_E^i, X_k^i, X_\Phi^i, X_{\Delta\Phi})$ is used to quantify the confidence of wave height (energy), wavelength (wave number), propagation direction and directional spreading (the same for all sub system). Therefore, a partitioned priori spectrum S^i is given on a polar grid (k, Φ), the corresponding processes $\tilde{S}^i$ can be written as

$$\tilde{S}^i(\Phi, k) = X_E^i X_{\Delta\Phi} X_k^i S^i\left(\Phi_0^i + \left(\Phi - X_\Phi^i - \Phi_0^i\right) X_{\Delta\Phi}, X_k^i k\right) \qquad i = 0, ..., n_p \tag{6.3}$$

- The algorithm makes use of the phase information contained in the SAR cross spectrum to resolve ambiguities in the wave propagation direction.

The inversion scheme is able to blend SAR information (cross spectrum, Φ_k) and wave model spectrum wave number spectrum F_k in a consistent way based on a maximum posterior approach as given in (6.4).

$$\mathbf{pdf}(F_k, \alpha | \Phi_k) = \frac{\mathbf{pdf}\left(\Phi_k | F_k, \alpha\right) \mathbf{pdf}(\alpha) \mathbf{pdf}\left(F_k\right)}{\mathbf{pdf}\left(\Phi_k\right)} \tag{6.4}$$

The symbol α represents a set of uncertain SAR ocean wave imaging parameters, as introduced in (6.2). A Flowchart for the inversion scheme is given in Fig. 6.2.

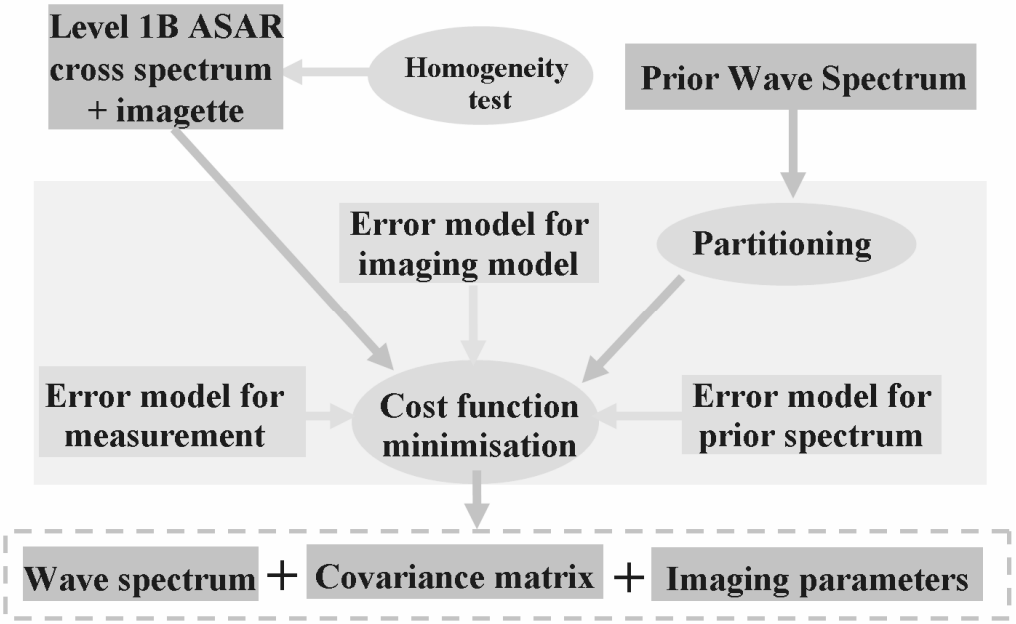

Figure 6. 2 Flowchart of the PARSA algorithm (after *Schulz-Stellenfleth et al.*, 2008)

The maximum posterior approach is equivalent to a cost function minimization, which is solved using an iterative approach to estimates an ocean wave spectrum such that the respective simulated cross spectrum as calculated by the fully non-linear forward model matches best the measured cross spectrum.

The inversion scheme starts with decomposing the priori wave model spectrum F_k into different wave systems, e.g., windsea and swell, and then is transformed to the polar grid by using the transformation given in (6.3). The partitioned model spectra are mapped into the cross spectrum as the simulation results by the forward model given in (3.15) in Chapter 3. The inversion is then carried out by an iterative correction of priori wave spectrum by comparing the simulated cross spectrum to the observed cross spectrum. The adjusted priori wave spectrum leading to a changed cross spectrum and results in reducing the cost function. A straightforward termination for the iteration follows the requirement that the estimated error should be an order of magnitude smaller than the expected error as given by the priori distribution.

6.2. Inversion scheme of WVW

The ENVISAT ASAR WVW products provide two-dimensional ocean wave spectra derived from ASAR wave mode images on a regular basis. They are provided on a log-polar grid with 24 wavelengths and 36 directions. The ESA algorithm uses cross

spectra derived from single-look-complex ASAR wave mode data as described in [*Engen and Johnsen*, 1995].

The methodology for the currently available ASAR wave mode WVW products is briefly introduced. The non-linear transformation between SAR cross spectrum and ocean wave spectrum is given in (3.15). The main idea for the WVW inversion scheme is to divide the SAR cross spectrum into a non-linear (mainly wind driven) part and a quasi-linear (mainly swell driven) part:

$$P = P^{ql} + P^{nl} \tag{6.5}$$

The philosophy of the proposed cross spectra wave retrieval inversion scheme for WVW products is to separate the contribution of wind sea part P^{nl} from the observed full nonlinear cross spectrum P, then the remaining part is the quasi-linear contribution from swell. If the signal-to-noise ratio of the SAR cross spectra is large enough, a unique solution of the wave spectrum can be achieved [*Johnsen, 2001*]. Some features for the implementation of the inversion scheme in the WVW products is given in the following.

- **Estimation of the wind field**

The non-linear part in the SAR cross spectra is assumed to be caused by the wind sea. Therefore the estimation for the wind field is a crucial point in the inversion. For the WVW products, the wind direction is estimated either using the external information, e.g., from numerical atmospheric model, or assuming the wind direction is 45° relative the SAR range direction. Using the assumed wind direction, combining with the conventional CMOD function for surface wind field retrieve [*Stoffelen and Anderson*, 1997; *Lehner et al*., 1998], the wind speed is estimated.

- **Estimation of the inverse wave age**

The wave age is tuned by fitting the measured azimuth shift variance to the corresponding simulated one by the given wind speed and wind direction. The azimuth shift variance is computed from the measured cut-off of the azimuth spectral profile.

- **Estimation of the non-linear part in the cross spectra**

Using the given wind speed, wind direction and wave age, ocean wave spectra can be constructed with the model proposed by *Elfouhaily et al.* [1997]. Then the non-linear part is calculated using the transformation given in (3.15).

Eventually, the estimated non-linear part is removed from the observed cross spectra, and the remained is the quasi-linear part. Thus swell spectra can be resolved uniquely.

Above are the basic elements of the inversion scheme for the current ASAR wave mode WVW products. One can conclude that the most important feature for the WVW schemes is the removing of the non-linear part in the cross spectrum, which is related to the cut-off estimation. Therefore remaining in the full cross spectrum is the wave information contained in the SAR cut-off domain only. The retrieved wave spectra in the WVW products, in fact, yields the information on the two-dimensional distribution of energy density for long waves [*Abadalla et al.*, 2008] contained in the ASAR wave mode data.

In the following validation and intercomparison, the limitations for the current WVW products are shown. First an example over the North Pacific is given.

6.3. Validation of PARSA and WVW schemes

As both algorithms are proposed to yield two-dimensional ocean wave spectra from ASAR wave mode data, the comparison of the retrieved spectra by the two algorithms is presented as first.

Comparison of retrieved two-dimensional ocean wave spectra

In Fig. 6.3, SWH given by the DWD global forecast wave model at 09:00 UTC on Dec.4th, 2006 is superimposed with an ASAR orbit across the North Pacific acquired between 09:15 UTC and 09:31 UTC. Small squares show the location where ASAR wave mode data are acquired with colors presenting the SWH retrieved by the PARSA scheme. One can observe that the orbit passes through a North Pacific storm with SWH above 10 m. Three ASAR wave mode imagettes of this orbit are located in quite different sea state, i.e. A (41º10′*N*/175º33′*W*) 、B (37º38′*N*/174º36′*W*) 、C (19º54′*N*/170º22′*W*) with respective SWH of 7.6 m, 5.8 m and 2.7 m as given by the

PARSA inversion。

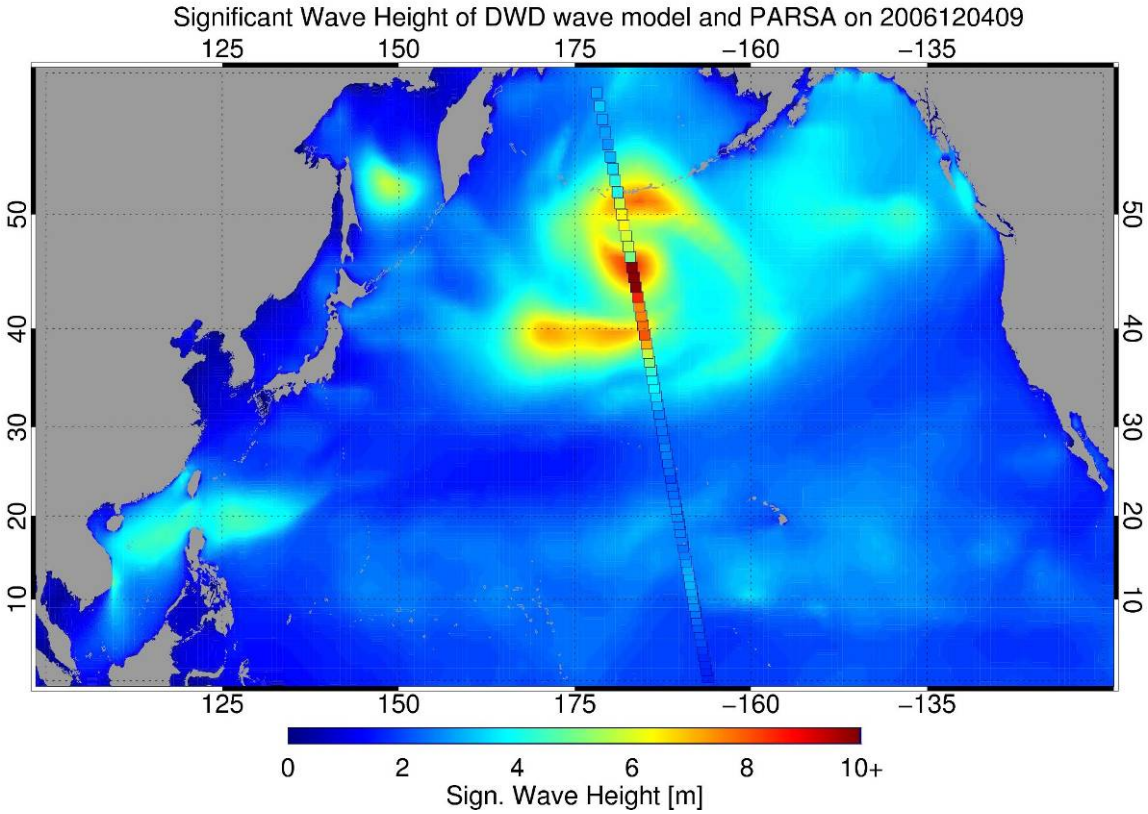

Figure 6. 3 SWH of DWD forecast wave model on Dec.4th, 2006 at 09: 00 UTC superimposed with SWH derived from ASAR wave mode data by the PARSA scheme

Respective retrieved two-dimensional ocean wave spectra for the three ASAR imagettes, as well as the wave spectra derived from ECMWF reanalysis wave model used as priori information for PARSA scheme are shown in Fig.6.4 (a), (b) and (c).

The retrieved PARSA spectra are consistent with the priori wave spectrum given by the ECMWF reanalysis wave model. On the one hand, the ECMWF reanalysis wave model has been assimilated with the ASAR cross spectrum information. The inversion scheme PARSA is proposed using for wave model assimilation, therefore the retrieved wave spectrum should be consistent with the wave model output, though. In the retrieved ocean wave spectrum by the PARSA scheme, the adjusted wave energy, wavelength and propagation direction, as well as the directional spreading using ASAR information are also visible. For ASAR imagette A, two swell systems with peak wavelength of 200 m and 300 m are resolved by the ECMWF reanalysis

wave model. The later swell system with higher energy is adjusted by the PARSA inversion scheme with increased wavelength to around of 400 m. The energy adjustment leads the SWH of 6.8 m given by the ECMWF wave model to be of 7.6 m retrieved by the PARSA scheme. With respect to B, it seems that only the SWH increases slightly from 5.5 m (ECMWF) to 5.8 m as given by the PARSA result. The sea state where C locates is rather complex with four wave systems traveling in different directions. Peak wavelengths for these subsystems are all increased by the PARSA inversion, while the SWH stays consistent for the total sea compared to the priori information. From the three examples for comparison, one can generally conclude that the PARSA scheme blends the ASAR observations into the priori information in a homogenous way with adjustments for partitioned wave systems and these adjustments increase with sea state, e.g., the adjustments of the energy are particularly pronounced in high sea state.

The ocean wave spectra derived from ASAR wave mode WVW products are obviously limited to the ASAR cut-off wavenumber. Only the long wave information contained in the ASAR image are retrieved. On the other hand, one can observe that artificial effects of the SAR ocean wave imaging mechanism are also are visible in the cross spectrum, which needs to be taken care of, when using the SAR look cross spectrum resolving wave propagation direction.

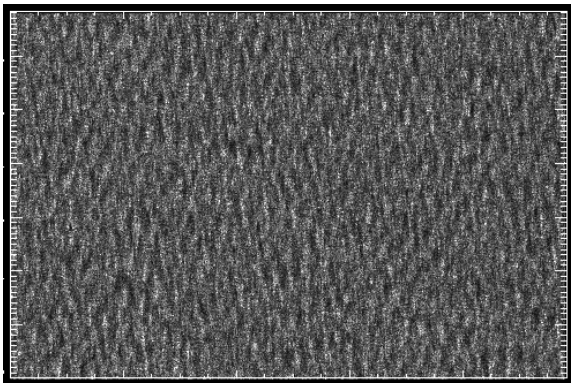

ASAR Wave Mode data (WVI)

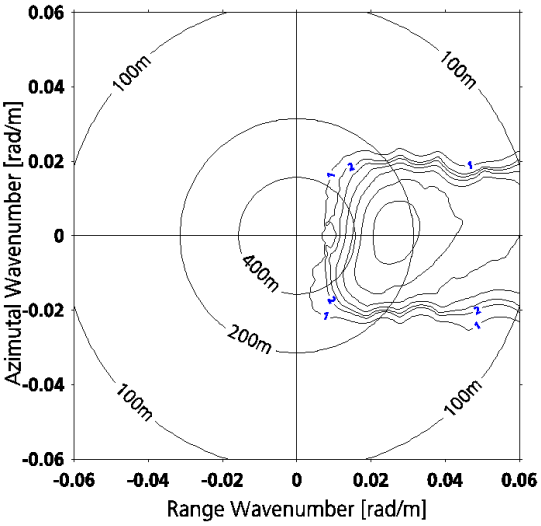

ASAR Wave Mode WVW Product

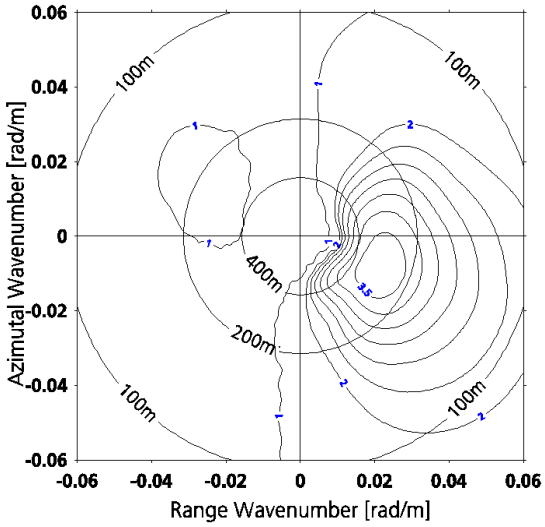

ECMWF reanalysis wave model spectrum

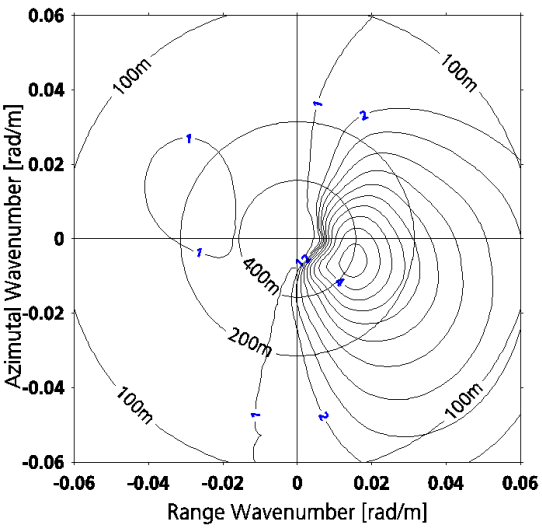

PARSA spectrum

(a)

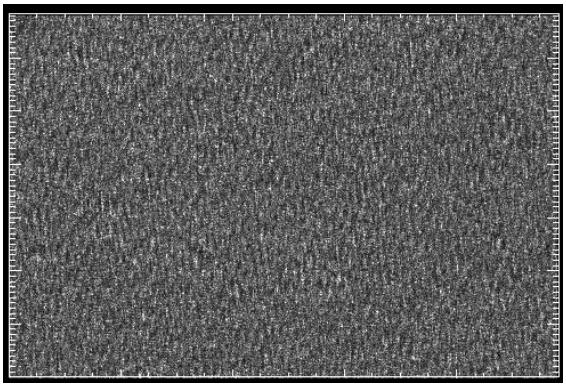

ASAR Wave Mode data (WVI)

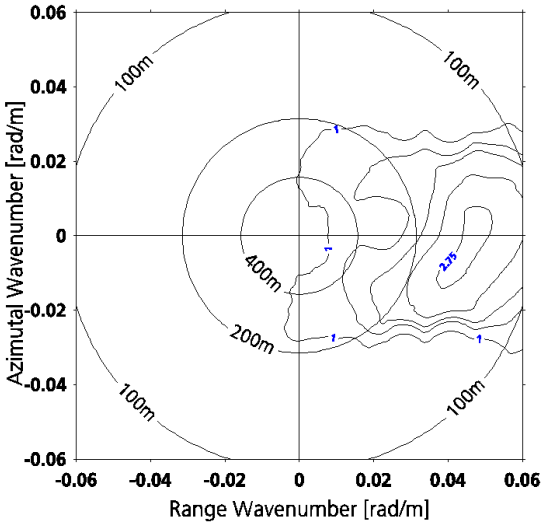

ASAR Wave Mode WVW Product

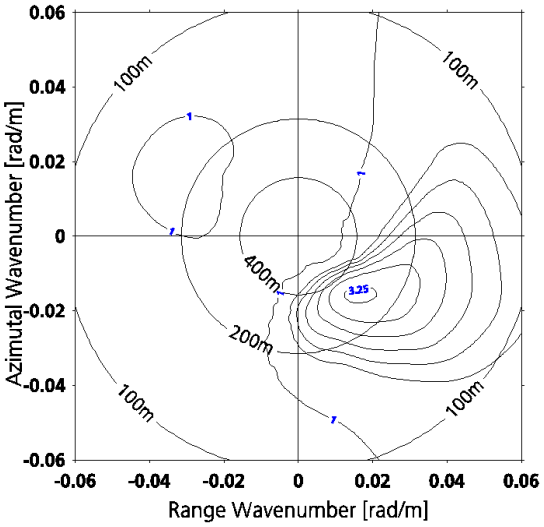

ECMWF reanalysis wave model spectrum

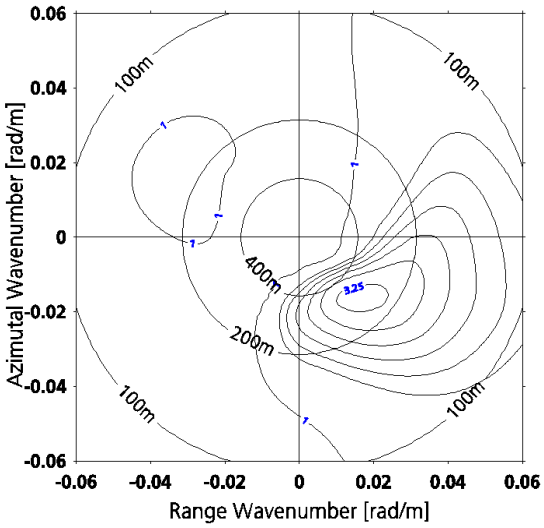

PARSA spectrum

(b)

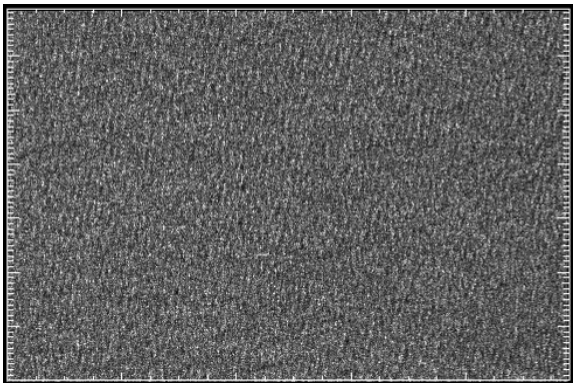

ASAR Wave Mode data (WVI)

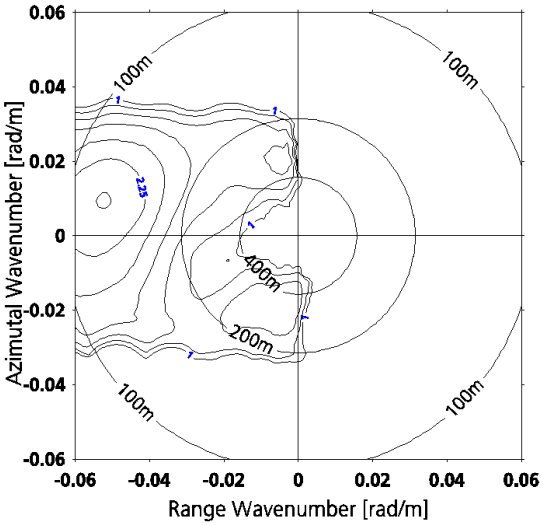

ASAR Wave Mode WVW Product

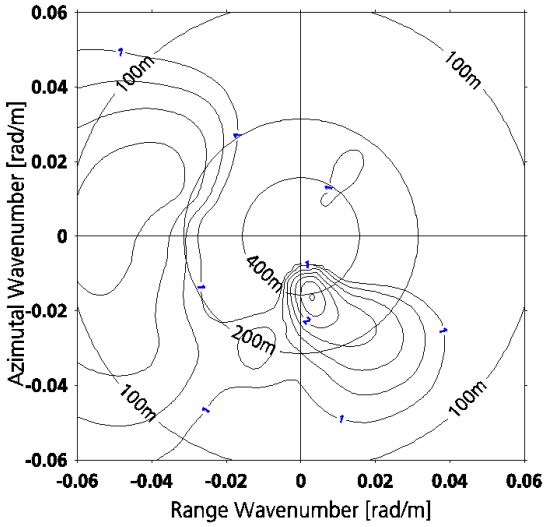

ECMWF reanalysis wave model spectrum

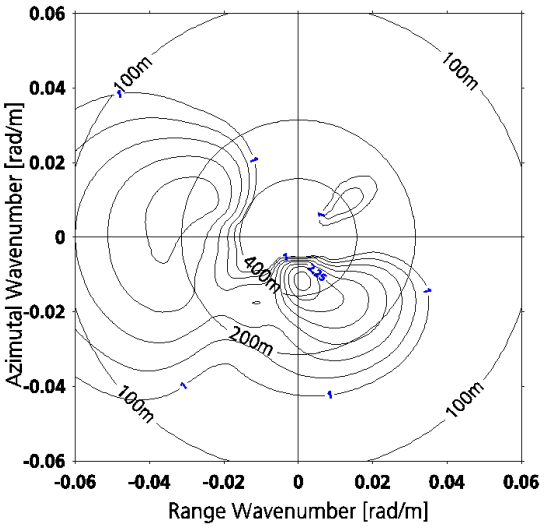

PARSA spectrum

(C)

Figure 6. 4 Comparison of retrieved two-dimensional wave spectrum from ASAR wave mode data using PARSA and WVW algorithm based on three ASAR wave mode data acquired on Dec.4th, 2006 in different sea state

Integral wave parameters from the different sea state, e.g., SWH, mean wave period retrieved by PARSA and WVW schemes are given in the following.

Validation of integral wave parameters

The integral wave parameters, e.g., SWH, zero-upcrossing mean wave period T_{m02} and wave height H_{12} can be derived from the estimated two-dimensional ocean wave

spectrum, according to:

$$SWH = 4\sqrt{\int E(f,\theta)df\,d\theta} \tag{6.6}$$

$$T_{m02} = \sqrt{\int E(f,\theta)dfd\theta \Big/ \int E(f,\theta)f^2 dfd\theta} \tag{6.7}$$

$$H_{12} = 4\sqrt{\int_{f<1/12s} E(f,\theta)dfd\theta} \tag{6.8}$$

The differences between ASAR measurements Y_i and results of other dataset X_i (e.g., buoy or numerical model) are quantified in terms of bias, root-mean-square-error (RMSE) and scatter index (SI), given by (6.9)-(6.11).

$$Bias = \overline{Y_i} - \overline{X_i} \tag{6.9}$$

$$RMSE = \sqrt{\frac{\sum (Y_i - X_i)^2}{n}} \tag{6.10}$$

$$SI = \frac{1}{\overline{X_i}}\sqrt{\frac{1}{n}\sum\left[\left(Y_i - \overline{Y_i}\right) - \left(X_i - \overline{X_i}\right)\right]^2} \tag{6.11}$$

- **PARSA versus buoy**

SWH derived from PARSA spectra in December 2006 and January, February and May in 2007 are used to validate the results against *in situ* buoy measurements. Around 1200 data pairs are collocated. The geolocation of the buoys is given in Fig.4.4 in Chapter 4.

Fig.6.5 (a) and (b) show the comparison result as scatter diagrams. PARSA (a) and ECMWF (b) reanalysis wave model results are compared to buoy data respectively. For the ECMWF comparison, only cases collocated to PARSA retrievals

are considered. Due to the assimilation of ASAR and RA measurements, the correlation of the ECMWF reanalysis model with the buoys is good indicated by the scatter index of 20%. The PARSA results have a similar scatter index of 21% and a RMS error of 0.64 m, slightly higher by 0.06 m relative to the ECMWF reanalysis model results in comparison the buoy measurements.

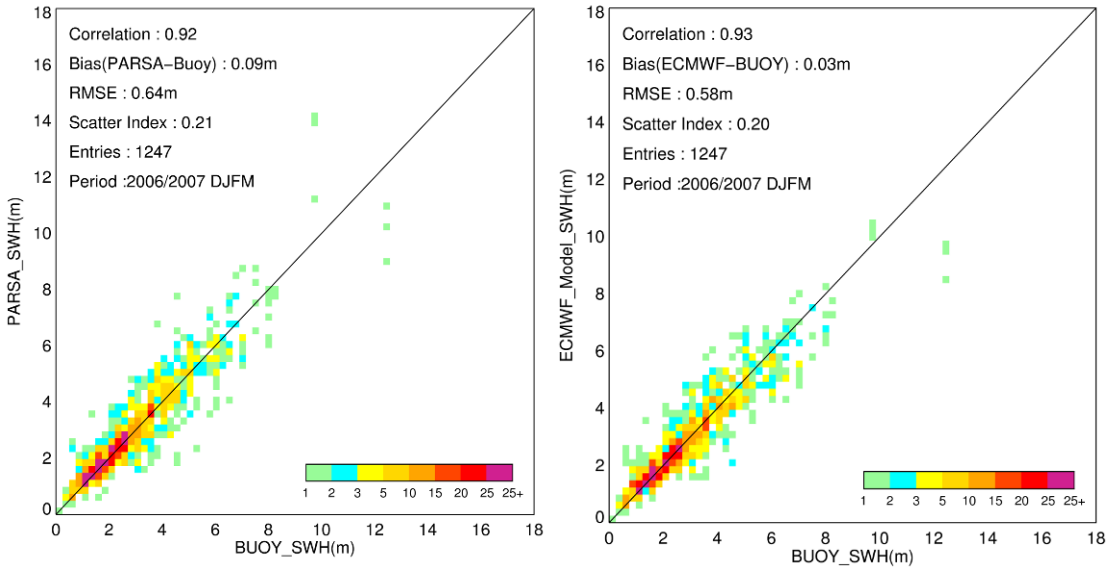

(a) (b)

Figure 6. 5 Scatter diagrams of SWH retrieved by PARSA (a) and collocated ECMWF reanalysis wave model (assimilated with ASAR and RA information) (b) compared to *in situ* buoy measurements

- **PARSA versus numerical wave models**

With regard to the comparisons to results of the numerical wave model, data pairs collected in December 2006, January and February 2007 are used. The SWH retrieved by PARSA compared to the ECMWF reanalysis wave model and the DWD forecast wave model are represented in Fig. 6.6 (a) and (b), respectively.

The comparison shows that the PARSA spectra results have better agreement with ECMWF reanalysis wave model results than compared to the DWD model, e.g., SI is lower than 10% and RMS error is only 25 cm, which might be because the PARSA uses the ECMWF model results as priori information. As the DWD forecast wave model is independent of SAR and RA information, comparison to this model shows independent results for the SAR ocean wave retrieval algorithm.

One interesting point is that SWH derived from PARSA spectra is substantially higher than for both wave models at high sea state. Due to the limited buoy comparison in high sea state (as shown in Fig.6.5), it is difficult to judge the performance of retrieved results by PARSA retrieval and reanalysis or forecast wave model results in this situation. The cross over collocated RA observations over high sea state will be used for comparison.

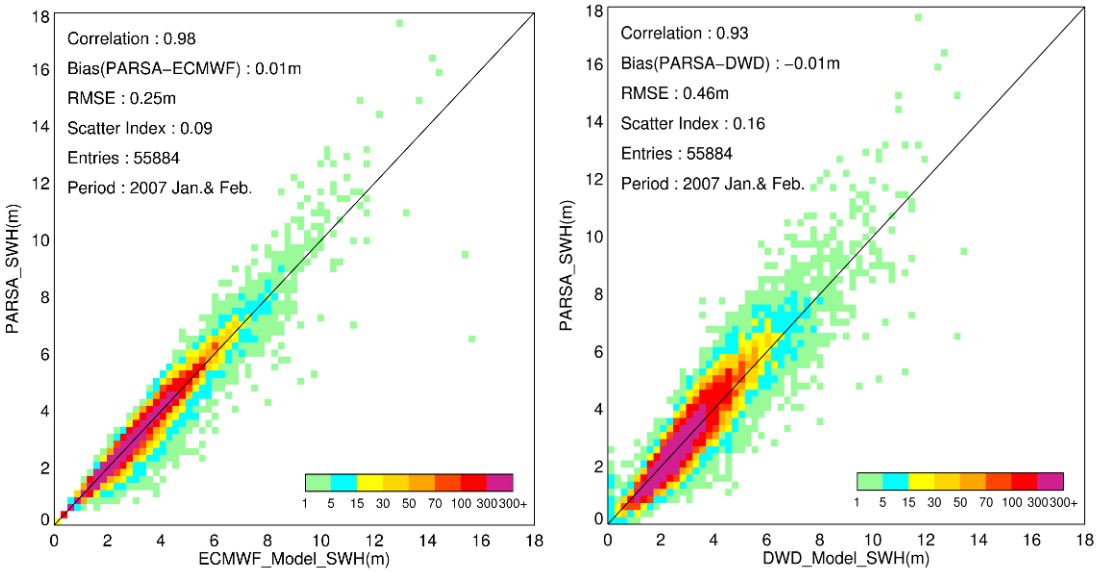

(a) (b)

Figure 6. 6 Scatter diagrams of SWH retrieved by PARSA compared ECMWF reanalysis wave model (a) and DWD forecast wave model (b)

Wave height H_{12} as given in Equ.(6.8) is associated with wave components with wavelength longer than 220 m. Such waves are directly detectable as patterns on the ASAR images. On the other hand, validation results show that SWH derived from numerical wave models, e.g., WAM operated in ECMWF there is a positive bias larger than 0.25 m related to swell events (e.g., wave period in the range of 10-15 s) generated by storms in the Southern Hemisphere winter time when compared to *in situ* buoy measurements [*Janssen*, 2008]. Therefore it is particularly interesting to compare H_{12} PARSA algorithm to model results.

Fig. 6.7 (a) and (b) shows the comparisons to the ECMWF reanalysis wave model for H_{12} and T_{m02} retrieved by the PARSA scheme. Both plots show good correlation higher than 0.90 to the wave model results. For H_{12} comparison, the scatter index is of

24% and RMS error is 0.26 m. With respect to the T_{m02} comparison, a better scatter index of 6% is acquired while correlation is slightly lower of 0.93. The lowest mean wave period retrieved by PARSA is around 3 s, which corresponds to a wavelength of 15 m in deep water. On the other hand, one can observe many entries showing a higher estimation of mean wave period retrieved by PARSA than the ECMWF wave model results. This indicates that the long wave information contained in the ASAR image is blended well into the retrieved spectra by the algorithm.

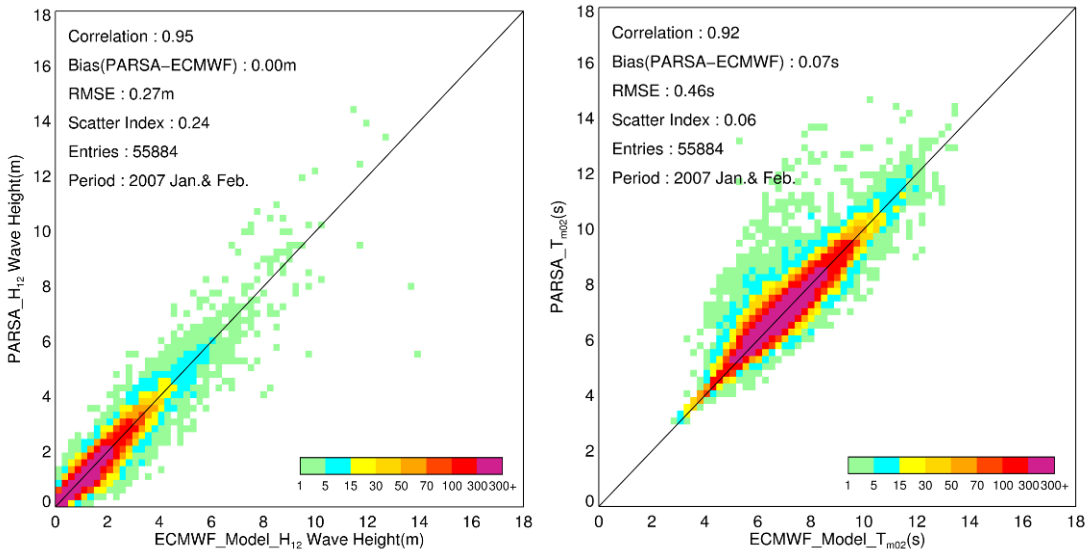

(a) (b)

Figure 6. 7 Scatter diagrams of H_{12} (a) and T_{m02} (b) retrieved by PARSA compared ECMWF reanalysis wave model

Integral wave parameters derived from the retrieved two-dimensional ocean wave spectra by non-linear PARSA scheme are presented above. Validation for the inversion scheme for WVW products is given as follows.

- **Validation of inversion scheme for WVW**

The ESA-ENVISAT WVW products provide two-dimensional ocean wave spectra derived from ENVISAT wave mode images on a regular basis. They are provided on a log-polar grid with 24 wavelengths and 36 directions. The ESA algorithm uses cross spectra derived from single-look-complex ASAR wave mode data as described in [*Engen and Johnsen*, 1995]. In this section, WVW products are compared to wave

models and *in situ* measurements in order to demonstrate the benefits of PARSA with respect to the products currently available. WVW products are intended to deliver particularly precise information for long waves inside the cut-off region of the spectrum. Thus the wave height H_{12} is used for assessment, too.

The same dataset with results from the PARSA inversion compared to *in situ* buoy measurements is used as SWH derived from WVW data for spectral validation. However, it should be noted that in the scatter plot presented in Fig. 6.8 there are 192 entries, around 15% of the dataset for buoy comparison, are located at the origin (0, 0), which demonstrates that there is no SWH data available for cases when the ocean wave spectra cannot be retrieved from the cross spectra based on the quasi-linear inversion scheme adopted for the ESA wave mode products. This can be observed as well when SWH is compared to ECMWF and DWD model results as shown in Fig.6.9 (a) and (b), and H_{12} comparison in Fig.6.10. Many cases, nearly 25%, for triple comparisons are not converted successfully by this scheme and cannot be used for triple comparisons.

Considering all the comparisons of integral wave parameters derived from the ESA WVW spectra, the scatter indices are all higher than 30% and the RMS error are higher than 0.65 m for the SWH comparisons. Another important conclusion from these three figures is the estimation of SWH derived from WVW spectra is significantly underestimating the sea state. This is particularly obvious when the SWH is higher than 4 m, though in the lower sea state it seems that WVW can provide reasonable estimates.

Even if it is argued that the WVW results are only available for the long wave information resolved by the ASAR sensor, it still cannot provide reliable sea state estimations in many cases, as evident from the H_{12} comparison as shown in Fig.6.10, which are in fact results for wave already longer than 220 m.

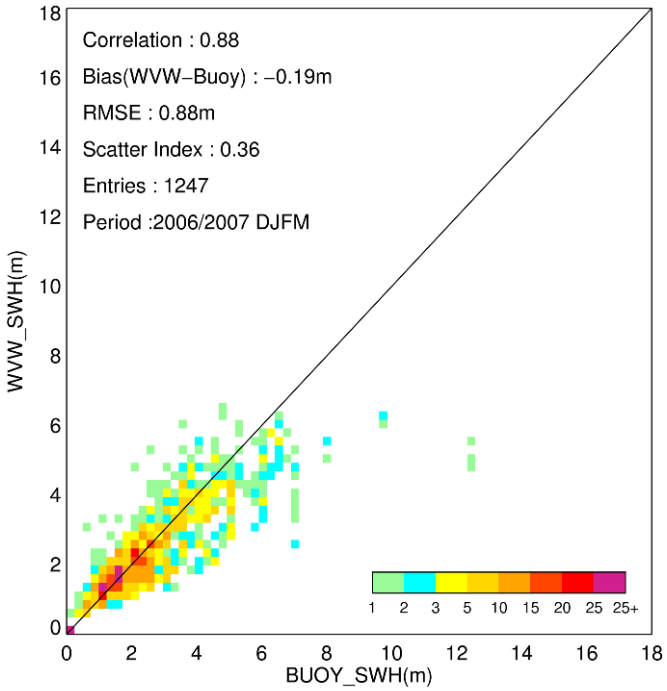

Figure 6. 8 Scatter diagram of SWH derived from ESA Level2 WVW spectra compared to in situ buoy measurements. There are together 192 entries located in the origin (0, 0) demonstrating the cases that WVW spectra are not successfully converted.

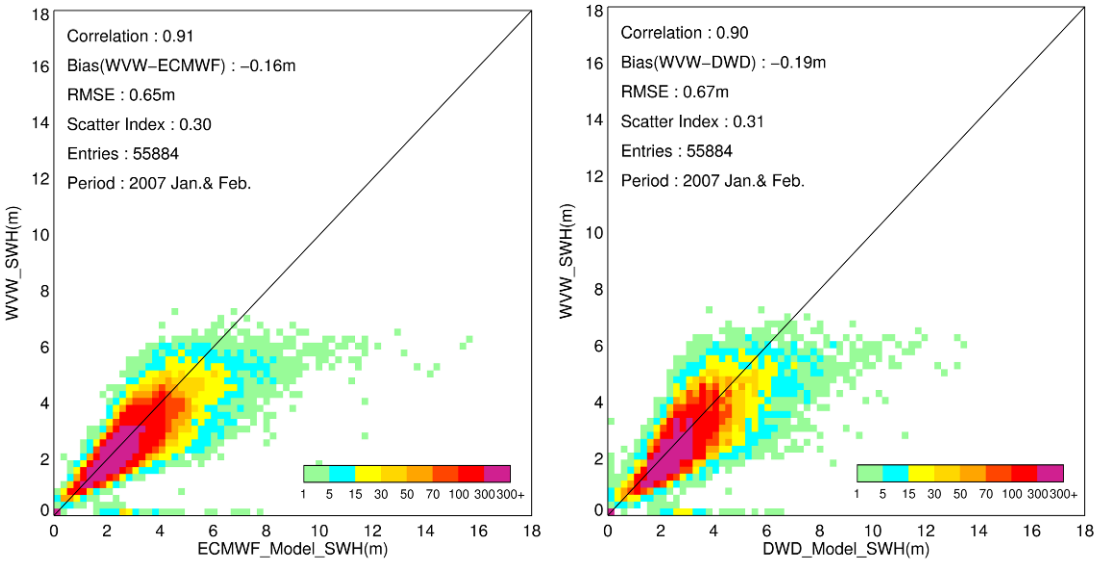

(a) (b)

Figure 6. 9 SWH derived from ESA Level2 WVW spectra compared to ECMWF reanalysis wave model (a) and DWD forecast model (b)

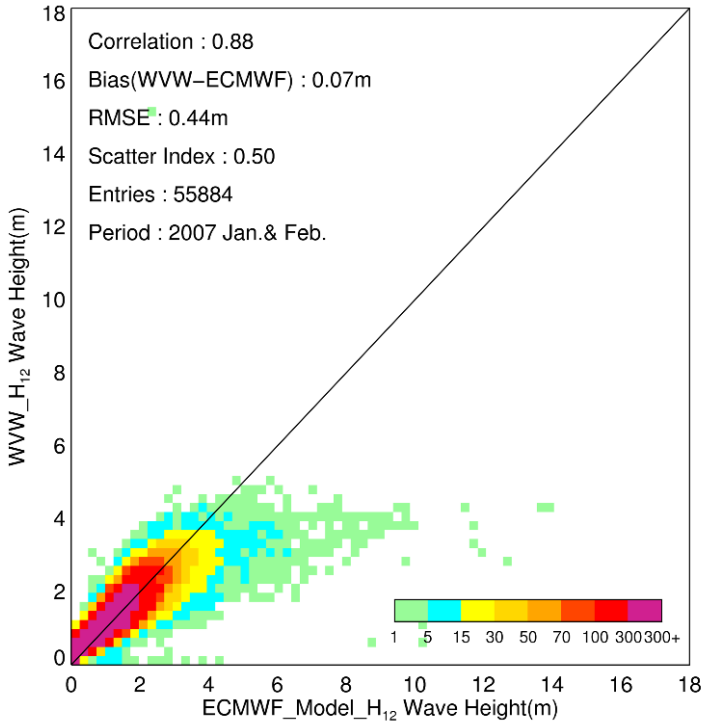

Figure 6. 10 H_{12} derived from ESA Level2 WVW spectra compared to ECMWF reanalyzed wave model

6.4. Conclusions

Results achieved during the validation and intercomparison for the PARSA and WVW schemes are presented in this paper. Three months global data acquired during 2006 December to 2007 February are used for comparisons to the numerical wave models; an additional month of 2007 May is included as well for the buoy comparison.

Comparison of retrieved two-dimensional wave spectra by the PARSA inversion to the ECMWF wave model spectra shows that the inversion blends well the SAR information into the priori wave model results, which leads to the adjustment of the wave direction, wave length as well as wave energy. This change increases with sea state, which is especially obvious for the wave height.

The spectra derived from the ESA WVW products are limited to the cut-off wavenumber domain. Further it seems that the artificial effect of SAR imaging of ocean waves is not considered sufficiently in the inversion.

A summary of the statistical parameters obtained in the analysis of significant wave height is given in Tab.6.1 showing that very good results of SWH can be

achieved with the PARSA inversion scheme.

Table 6. 1 Statistical results of different SAR ocean wave algorithms for SWH compared to *in situ* buoy measurements and results of numerical wave models

	Vs. buoy			**Vs. ECMWF**			**Vs. DWD**		
Algorithm	Bias (m)	RMSE (m)	SI	Bias (m)	RMSE (m)	SI	Bias (m)	RMSE (m)	SI
PARSA	0.09	**0.64**	**0.21**	0.01	**0.25**	**0.09**	-0.01	**0.46**	**0.16**
WVW	-0.19	0.88	0.36	-0.16	0.65	0.30	-0.19	0.67	0.31

Also it should be noted that currently the in situ dataset does not contain any data from the southern hemisphere were there are high sea states observed in large regions throughout the year and where the SAR observations can particularly improve the knowledge on ocean surface waves. Another issue addressed was the fact that most of the buoys are close to the coast and are therefore not fully representative for the sea state (in particular for storm events) in the open ocean. One strategy presented is the use of co-located altimeter measurements. As seen in the North Atlantic storm event case study [*Li, et al*., 2009], while the distance between wave mode images and altimeter measurements of around 300 km is likely to lead to considerable different wave height near the center of a severe storm. Therefore the cross over collocation with altimeter measurements for validation is needed in the future research.

Considering the present level-2 WVW products from ESA, it should give a swell wave height while the comparisons presented in the paper shows the significant underestimation for the sea state, which is also presented by the validation in ECMWF [*Abadalla, et al.*, 2008].

The fact that the priori information from the ECMWF reanalysis wave model used in the PARSA inversion already went through the MPI inversion scheme making use of the level-1b ENVISAT ASAR cross spectrum product will be considered in future studies.

Chapter 7

Empirical Algorithm CWAVE_ENV Development and Validation

After the validation of existing algorithms, in this chapter a new algorithm was developed that yields SWH and mean wave period without the use of a first guess.

Contents of this chapter are based on the paper entitled "***Ocean Wave Integral Parameter Measurements Using ENVISAT ASAR Wave Mode Data***", which is submitted to *IEEE Transactions on Geoscience and Remote Sensing.*

An empirical model consists of a function that fits a given dataset without giving a geophysical explanation. The graph of the function goes through the data points approximately. Thus, although we cannot use an empirical model to explain a system exactly, such a model can be used as a predictor or an estimator. In ocean remote sensing, quite a few empirical models are used in practice to derive ocean physic parameters, e.g. empirical algorithms are widely applied in the processing of the global CZCS data set [*Gondon et al*., 1983]; the CMOD to retrieve wind field from Scatterometer [*Stoffelen and Anderson*, 1997]; and the empirical models are used to measure mean wave period with Altimeter data [*Gommenginger et al*., 2003]. For SAR, integrated wave parameters are estimated as well by an empirical model CWAVE [*Schulz-Stellenfleth et al*., 2007].

Regarding to the current non-linear or quasi-linear algorithms retrieving two-dimensional ocean wave spectra from SAR imagery, either priori information from a numerical wave model is needed e.g., MPI scheme or PARSA scheme as used at weather forecast centers, or like for the ESA WVW products the retrieved wave spectra are limited to waves longer than a certain threshold, as described in the previous chapter.

In this chapter, an extended empirical algorithm called CWAVE_ENV to derive integral wave parameters such as SWH, mean wave period T_{m02} and wave height H_{12} from ENVISAT ASAR wave mode data is presented. It has the calibrated ASAR wave mode images as the only input and does not need additional first guess

information from an ocean wave model. This algorithm thus makes the SAR be an independent instrument measuring integrated wave parameters to Altimeter quality.

For the ERS mission, the empirical algorithm CWAVE_ERS [*Schulz-Stellenfleth et al.*, 2007] was proposed for the reprocessed ERS-2 SAR wave mode data [*Lehner et al.*, 2000]. Validation results show that the performance of CWAVE _ERS is fairly good when compared to the ECMWF WAM model using 6000 collocation data pairs and to 21 buoy measurements during three weeks in 1996. For both comparisons with respect to SWH, results of CWAVE_ERS show a small bias and RMS of 0.44 m and 0.39 m, respectively. While performance of CWAVE_ERS for high sea state, e.g., SWH larger than 6 m, is not evaluated in the comparisons.

Fig. 7.1 shows that the implementation of CWAVE_ERS empirical model on the ENVISAT ASAR wave mode data acquired during January and February in 2007.

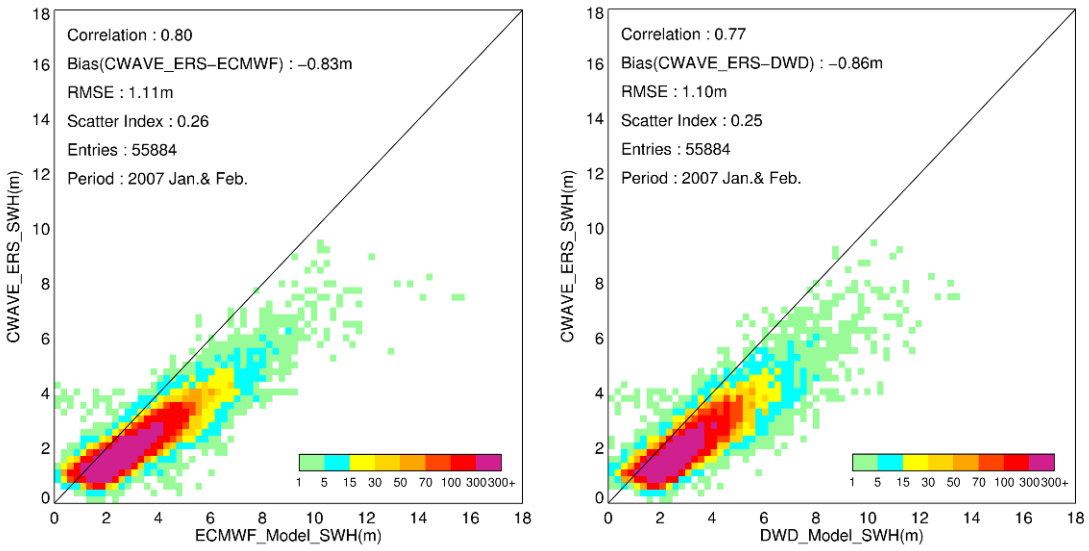

(a) (b)

Figure 7. 1 Scatter diagrams of SWH derived from ASAR wave mode data using the CWAVE_ERS empirical model compared to the ECMWF reanalysis wave model (a) and the DWD forecast wave model (b). This is used to demonstrate that the CWAVE_ERS model is not suitable for the ASAR wave mode data and a new one is demanded.

One can observe the low correlation, high bias and RMSE and scatter indices for the retrieved SWH compared to the ECMWF reanalysis wave model and DWD forecast wave model. Considering that ASAR wave mode data have different spatial resolution, image size, calibration constant and ocean surface imaging performance

with ERS-2 SAR wave mode data, a new tuning of the coefficients for the CWAVE_ENV model is needed. Using new CWAVE_ENV model, a global dataset of about 1000 measurements daily for ocean wave integral parameters from the ASAR wave mode data independent of priori information becomes available.

7.1. Introduction of the parametric model CWAVE_ENV

In this section, the CWAVE_ENV parametric model structure, model fitting procedure and its evaluation using the tuning dataset are described in detail.

Multiple Regression Model

Suppose n parameters or factors S $(s_{1,\ldots,}s_n)$ are thought to affect the expected observation W with coefficients A$(a_{0,\ldots,}a_n)$. A simple linear regression model collecting these parameters in an estimator is given by (7.1), see [*von Storch and Zwiers*, 1999].

$$W = a_0 + \sum_{i=1}^{N} a_i s_i + E_i \tag{7.1}$$

where E_i are random variables with zero mean. Formula (7.1) is the simple linear regression for modeling n data points and independent factors, which corresponds to a straight line. For the CWAVE_ENV empirical model, a quadratic term is added on the right side of Equ. (7.1), i.e., it is a multiple linear model, taking into account the quadratic nonlinearities as well as possible coupling among different variables. Thus the final form of the model is given as,

$$W = a_0 + \sum_{i=1}^{N} a_i s_i + \sum_{i=1}^{N} \sum_{j=1}^{i} a_{i,j} s_i s_j \tag{7.2}$$

The model states that the observation W is expressed as a linear combinations of the factors $S(s_{1,\ldots,}s_n)$. However, the factors themselves can be nonlinear functions of other variables. In the following the variables chosen in the CWAVE_ENV model are described.

ASAR Image Parameters Selection in the CWAVE_ENV Model

Using the model given by (7.2) it is assumed that the *n* variables include all relevant predictor variables. It is often required to select the variables such that no essential information is lost. On the other hand, too many variables will increase the computational effort as well as make the model rather sensitive to minor changes.

In the CWAVE_ENV model, it is assumed that the ASAR parameters S_A ($s_{1,\ldots,}s_n$), i.e. the Normalized Radar Cross Section (NRCS, referred to as well as $\sigma_\circ$ shown in Equ. (7.3)), the variance of the normalized SAR image (*cvar* given in Equ. (7.4), see [*Kerbaol*, 1998]), and other parameters computed from the variance spectrum are regarded as related to ocean surface wave. Former researches state that due to the cut-off effect of SAR imaging mechanism only long wave information is imaged by SAR, which is apparent for high altitude orbit SAR systems like ERS SAR and ENVISAT ASAR, while complete wave parameters still can be retrieved from the SAR image by using the empirical model.

The NRCS of a SAR image is related to ocean surface wind based on the CMOD function [*Stoffelen and Anderson*, 1997; *Lehner et al*., 1998] and thus can represent short wave information.

$$\sigma_0 = 10 * \log_{10}\langle I \rangle - K \tag{7.3}$$

$$c\,\mathbf{var} = \mathbf{var}\left(\frac{I - \langle I \rangle}{\langle I \rangle}\right) \tag{7.4}$$

In (7.3) and (7.4), $\langle I \rangle$ is the mean intensity of ASAR imagettes and K is the calibration constant.

Estimation of the ASAR image spectrum is performed by computing the image periodogram with a two-dimensional FFT algorithm. The raw periodogram is not a good spectral estimation because of spectral bias and the fact that the variance at a given frequency does not decrease as the number of samples used for the computation increases. The variance problem can be reduced by smoothing the periodogram. The idea behind is to divide the entire set with N samples into many sub sets with M samples, compute the FFT of each sub set, square it to get the power spectral density

and then compute the average of the ensemble. This approach applied on the ASAR image spectral estimation is given in Appendix 4.

In both the models CWAVE_ERS and CWAVE_ENV, 20 parameters are extracted from the estimated two-dimensional SAR image spectra. Together with $\sigma_{\circ}$ and *cvar*, there are 22 parameters that are collected into the ASAR image parameter vector S_A ($s_{1,\ldots,}s_n$) as input to the model (7.2).

Although the exact physical meaning behind (7.2) is not easily to be interpreted, the 22 parameters derived from the ASAR image include the essential information relating the image itself to both long wave and short wave information therefore the parametric model is successful in estimating ocean wave integral parameters of the complete spectrum.

Empirical Model Fitting Procedure

A least square minimization approach is used to tune the CWAVE_ENV empirical model as given by (7.5), where W is the integral wave parameter (e.g., SWH or mean wave period) derived from model or other observation data sources collocated to the ASAR image and treated as the "true" or at least very reliable sea state observations. It needs to be pointed out that different integrated wave parameters correspond to respective parametric model coefficients.

$$J_{\mathbf{cost}}(A) = \sum_{j=1}^{N}(W_j - \sum_{i=1}^{k} A_i S_i^j)^2 \tag{7.5}$$

A stepwise regression procedure is used for the least square minimization approach. The 22 parameters defined in the previous section are all included in the tuning approach; however there are possibilities that some parameters will not lead to a significant improvement of the empirical model. To diagnose the performance of every SAR image parameters collected in the vector S_A ($s_{1,\ldots,}s_n$), couples of terms are used to quantify this.

The regression (or explained) sum of squares due to regression is denoted by RSS

$$RSS = \sum_{j=1}^{N}(\sum_{i=0}^{k} A_i S_i^j - \overline{W})^2$$

(7.6)

The error (or residual) sum of squares (ESS) is

$$ESS = \sum_{j=1}^{N} (W_j - \sum_{i=0}^{k} A_i S_i^j)^2 \tag{7.7}$$

The multiple-regression is performed on every ASAR image parameter. The parameter S_{l1} for which RSS_{l1} is largest is chosen as the initial parameter. In the next step, a new parameter S_{l2} is selected, for which the incremental regression sum of squares RSS_{inc} is again largest.

$$RSS_{inc} = RSS_{l2} - RSS_{l1} \tag{7.8}$$

In the third step, the testing of hypothesis that the inclusion of new ASAR parameter S_{l2} significantly reduces the regression sum of squares are performed by computing the test variable of,

$$F^{(i+1)} = \frac{RSS_{inc}}{ESS_{l2} / (N - i)} \tag{7.9}$$

This is compared to the critical value of the distribution $F(1, N-i)$ [*von Storch and Zwiers*, 1999]. The iteration to select ASAR parameters will be terminated if the testing variable $F^{(i+1)}$ is below 0.99 or 99% quantiles and the coefficients in (7.2) are fitted.

7.2. CWAVE_ENV model implementation

In the present study, some filters are implemented on ASAR wave mode data to be used in CWAVE_ENV model tuning and validation.

(1) Only the ASAR wave mode data acquired in IS2 swath with incidence angle at around 23º and VV polarization are used.

(2) It should be noted that only wave mode data acquired between -70º S~70º N are included in the dataset in order to avoid effect due to sea ice coverage.

(3) Homogeneity test is performed on ASAR wave mode data. Two examples of inhomogeneous ASAR data are given in §2.2.3. The inhomogeneous data are excluded both from the tuning and validation dataset. The ratio of image variance and squared image mean is set in 1.05 as the threshold to classify the

ASAR wave mode imagettes into classes of homogenous or inhomogeneous cases [*Schulz-Stellenfleth and Lehner*, 2004].

ASAR wave mode data and collocated ECMWF wave model spectra in December 2006 are used as the tuning dataset.

In the CWAVE_ENV empirical model, the 22 parameters extracted from ASAR wave mode image are used for parametric model tuning approach.

The selection of a training dataset for the empirical model is a crucial point. Its accuracy should be very near to the ground truth and as well be sufficiently representative of different sea state within the global geographical coverage.

In situ buoy measurements are believed to be the "ground truth (with 10% or 0.25 m accuracy for wave height)" and are used generally for assimilation into offshore wave models, validation of global wave forecast models, calibration and validation of satellite wave sensors. Buoy measurements would be the best candidate for the tuning of the empirical model. However the existing sea state reference buoys are limited in terms of global distribution and location (few are located in the open sea and in the South Hemisphere) [*Swail*, 2008].

The SAR/ASAR wave mode data are typically acquired globally in the open sea where only few buoy measurements are available. Therefore in the present study, ASAR collocated ECMWF reanalysis wave model results in December 2006 are used as the tuning dataset. As mentioned in the Chapter 4, the reanalysis ECMWF wave model is assimilated by all available *in situ* and satellite information is the reasonable and available tuning dataset.

Histograms of SWH and Tm_{02} derived from the collocated ECMWF reanalysis wave model are shown in Fig.7.2 (a) and (b), respectively. It can be observed that the tuning dataset includes different sea state and the dominant SWH ranges between 1.5 m ~ 2.5 m contributing around 50% to the entire tuning dataset. The maximum SWH given by the ECMWF model in the tuning dataset is 12.6 m. The Tm_{02} distribution shows that the model measures numerous waves with period between 8 s ~ 9 s and long swell with periods larger than 12 s exist in the tuning dataset, too.

The tuning dataset is used for testing the CWAVE_ENV model parameter fitting approach. Fig. 7.3 shows the comparison results for SWH (a) and T_{m02} (b) of the tuning dataset to the ECMWF reanalysis model results. One can observe that the tuning approach of the CWAVE_ENV empirical model is successful making the

difference between the ASAR measurements derived by the CWAVE_ENV algorithm and the ECMWF reanalysis model results in the tuning dataset quite small with zero bias (as to be expected for the tuning), and low scatter indices of 15% and 7% for SWH and T_{m02} respectively.

Once the coefficients of the CWAVE_ENV model are fitted, it is used for the new complete dataset for the empirical model validation and calibration.

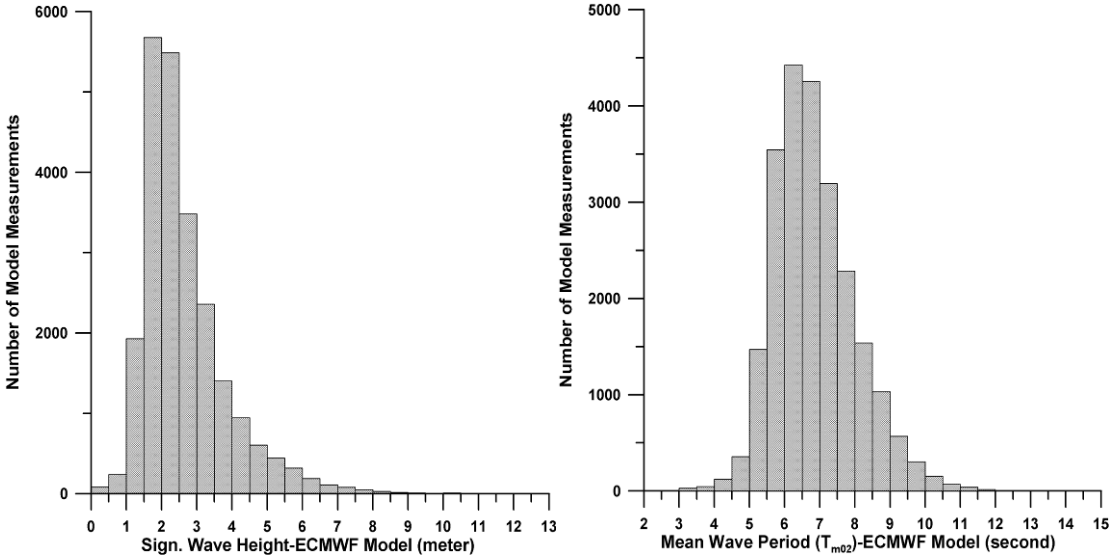

(a) (b)

Figure 7. 2 Histogram of SWH (a) and T_{m02} (b)) derived from the ECMWF analyzed model in December 2006, which are used in tuning dataset of CWAVE_ENV model

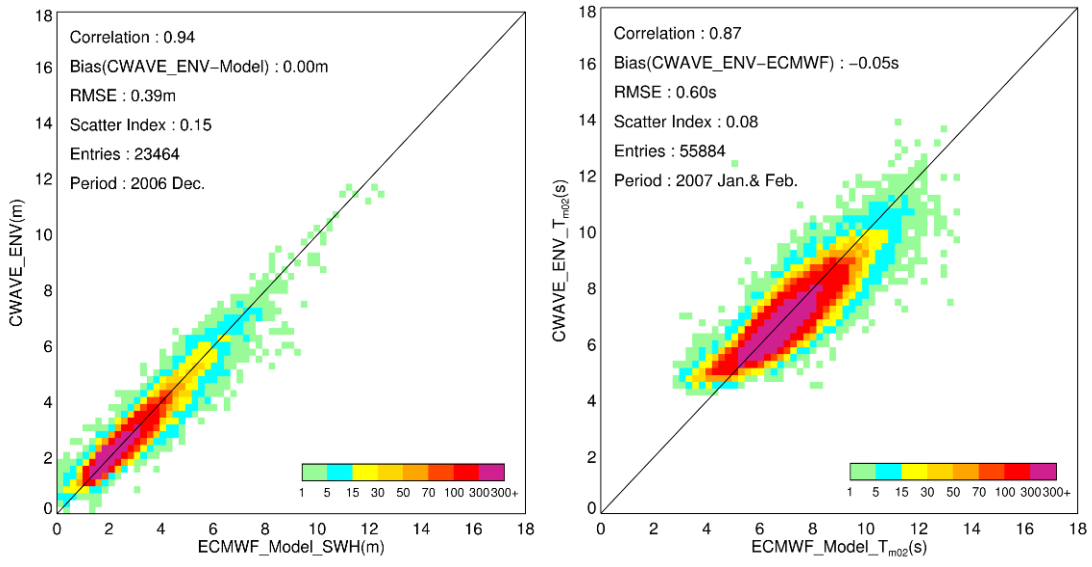

(a) (b)

Figure 7. 3 Evaluation of the tuning datasets consisting of the data in December 2006 for the CWAVE_ENV model

7.3. Performance assessment of the CWAVE_ENV empirical algorithm

In this section, SWH, T_{m02} and H_{12} derived from ASAR wave mode data are validated by comparisons to *in situ* measurements, numerical wave model and RA measurements comparisons on a dataset different to the tuning dataset.

Besides the validation of CWAVE_ENV algorithm, comparisons to the two other SAR ocean wave retrieval algorithms, i.e. PARSA and WVW schemes validated in chapter 6 are presented as well in this section.

- **Compared to *in situ* buoy measurements**

The comparison is discriminated between deep water (depth > 100 m) and shallow water cases, as shown in the scatter diagrams of Fig. 7.4 (a) and (b) respectively.

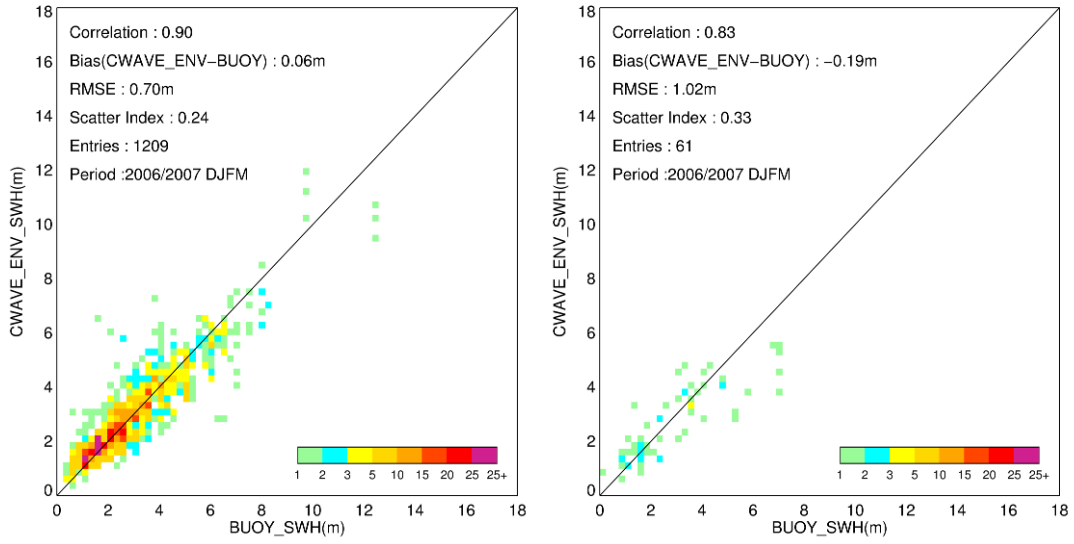

(a) (b)

Figure 7. 4 Scatter Plots of SWH derived by the CWAVE_ENV algorithm compared to buoy *in situ* measurements. (a) is for the comparisons in deep water and (b) is for shallow water

In deep water, SWH derived by the CWAVE_ENV empirical algorithms shows a good agreement against the buoy measurements. One can observe that generally the empirical algorithm can provide reliable retrieved SWH from ASAR wave mode data with nearly zero bias, RMSE of 0.70 m and a scatter index of 24% in deep water. Considering the 61 data pairs in shallow water, the retrieved SWH has a lower

estimation with bias of around 0.2 m and the scatter index becomes rather higher to 33%. As such near shore cases many be very variable and depend on collocation.

The tuning dataset we choose in the present study is the reanalysis numerical wave model, which has a good accuracy and global distribution and location. Taking account the spatial resolution of the reanalysis wave model, the coastal ocean wave processes, e.g., wave shoaling and refraction induced by the bathymetry, cannot be resolved though [*Li et al.,* 2009]. This therefore makes the retrieved results of CWAVE_ENV in shallow water showing a high bias.

To investigate the performance of CWAVE_ENV for different sea states i.e., from smooth to high sea state, a step comparison is carried out. In Table 1, the results of comparison are summarized. Besides the three statistical parameters defined in Chapter 6 (Equ.(6.9)-(6.11)), the bias percent (BP) is used as well, estimating the relative bias depending on the mean value of buoy observations:

$$BP = 100\% * (\overline{Y_i} - \overline{X_i}) \Big/ \overline{X_i} \tag{7.10}$$

Considering the usual measurement for quality, namely the scatter index, it is found that in rough sea state, i.e., SWH > 2.5 m, the CWAVE_ENV algorithm has a better performance with scatter indices lower than 20%. In a sea state with SWH lower than 1.25 m, there is a distinct difference between CWAVE_ENV results and *in situ* measurements. Retrieved SWH is overestimated compared to the buoy measurements and the scatter index in this sea state is 43%. The distinct difference between radar and *in situ* buoy measurements in low sea state is also shown in the validation for the RA measurements, e.g., see [*Cotton et al.*, 1997; *Krogstad and Barstow,* 1999]. This somewhat is induced by the spatial inhomogeneity given by the fact that ASAR is sampling measurements every 100 km spatially while the buoy is averaged within 20 minutes.

In high sea state, namely when SWH is higher than 4m, SWH derived by CWAVE_ENV is underestimated compared to buoy measurements and the bias increases with higher sea state. However, it is interesting to note that the scatter index is lower than 0.15 showing a quite promising agreement with *in situ* measurements in sea states with SWH > 6 m.

Table 7. 1 Statistical results assessing the performance of CWAVE_ENV for SWH in different sea state

SWH (m)	Data Pairs	Bias (m)	BP (100%)	RMSE (m)	SI
(0,1.25)	170	0.45	47.6%	0.60	0.43
(1.25, 2.5)	456	0.20	10.0%	0.63	0.31
(2.5,4)	370	0.07	2.0%	0.69	0.21
(4,6)	208	-0.34	7.0%	0.77	0.14
>6	66	-0.91	12.6%	1.41	0.15
All	1270	0.05	1.7%	0.72	0.24

Further investigation of the CWAVE_ENV algorithm will be considered for cases of very low (< 1.0 m) and extreme sea state (> 10.0 m) when compared to more collocations of *in situ* measurements.

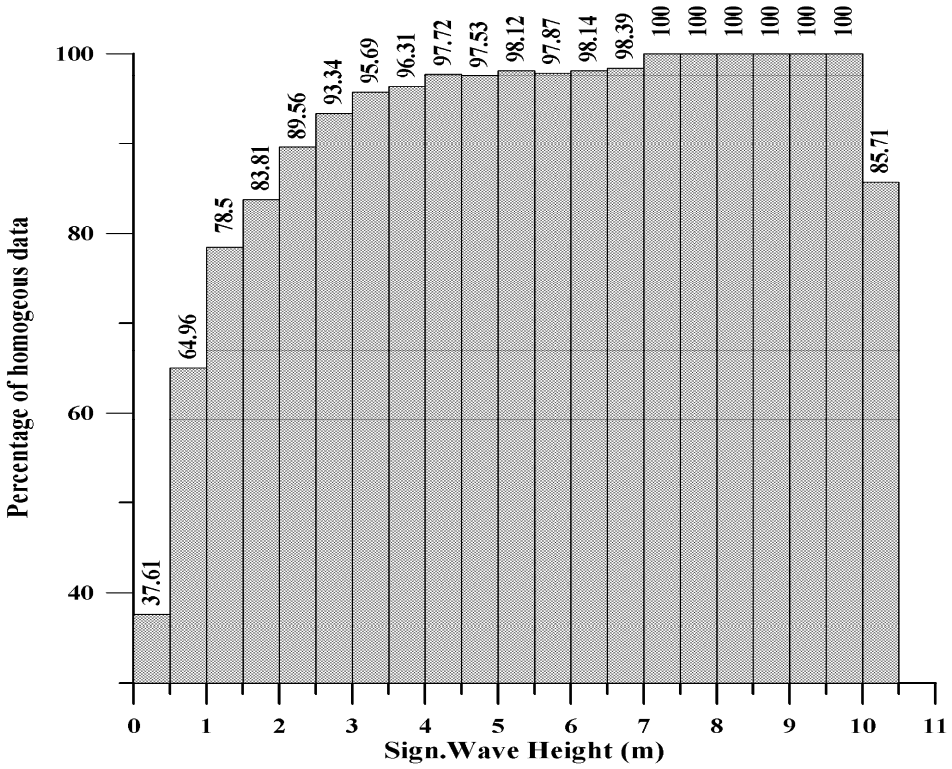

Figure 7. 5 Percentage of ASAR wave mode data that pass the homogeneity test in different sea states acquired during January and February 2007

In the next three sections, data pairs are collected in January and February 2007

for the comparisons to numerical wave models, existing ASAR wave mode level2 WVW products and the crossover radar altimeters. Homogeneity test are performed as well before the comparisons and validations. Figure 6 shows percentages for the ASAR wave mode data that pass the homogeneity test in different sea state during the two months. One can observe that more than 60% data are excluded when SWH is lower than 0.5 m. When SWH is higher than 2.5 m, 90% data are homogenous and can be used for comparisons.

- **Comparison to numerical wave models**

In this section, SWH, H_{12} wave height, T_{m02} as well as wave energy period T_{m-10} are compared to the ECMWF and DWD model results. The scatter plots of Fig. 7.6 (a) and (b) show the SWH comparisons against the ECMWF and DWD wave model results respectively.

Both plots in Fig. 7.6 show that SWH retrieved by the CWAVE_ENV empirical algorithm have good agreement compared to the reanalysis and forecast model with zero bias, 0.43 m and 0.51m of RMSE and scatter index of 16% and 18% respectively. For all statistical parameters, results derived from CWAVE_ENV algorithm compared to the ECMWF reanalysis model have a better agreement than compared to the DWD model. A plausible explanation is that the CWAVE_ENV algorithm is tuned by the ECMWF reanalysis model. In extreme sea state, e.g., when SWH is higher than 10 m, CWAVE_ENV results have a trend lower than the ECMWF model, but higher than the DWD model. As the ECMWF model has been assimilated with the *in situ* buoy and satellite data, thus the DWD forecast results give more independent comparisons.

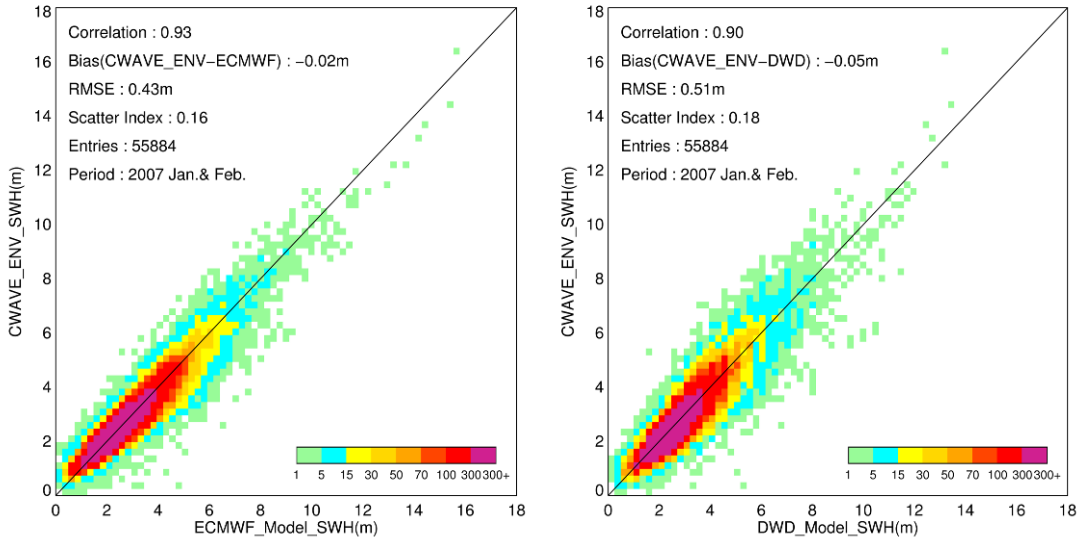

(a) (b)

Figure 7. 6 Scatter Plots of SWH derived by CWAVE_ENV compared to the ECMWF reanalysis Model (a) and the DWD forecast model (b) in January and February 2007

H_{12} and T_{m02} measurements are not available for the model provided by DWD. Results derived from the CWAVE_ENV algorithm for these parameters are compared to the ECMWF reanalysis model, as shown in Fig. 7.7 (a) and (b). The scatter index of the H_{12} comparison is 30% while the bias still remains very low at 3 cm. T_{m02} comparison has a scatter index of 8% and the RMSE is 0.6 s.

Additional to SWH, wave energy period $T_{m-10} = m_{-1} / m_0$ is another key parameter and used to calculate the wave power J via

$$J = 0.49 H_s^2 T_{m-10} \tag{7.10}$$

where J has units kW / m [WMO, 1998]. The wave energy period is also retrieved by the CWAVE_ENV algorithm and compared to the reanalysis ECMWF model, as shown in Fig. 7.7 (c).

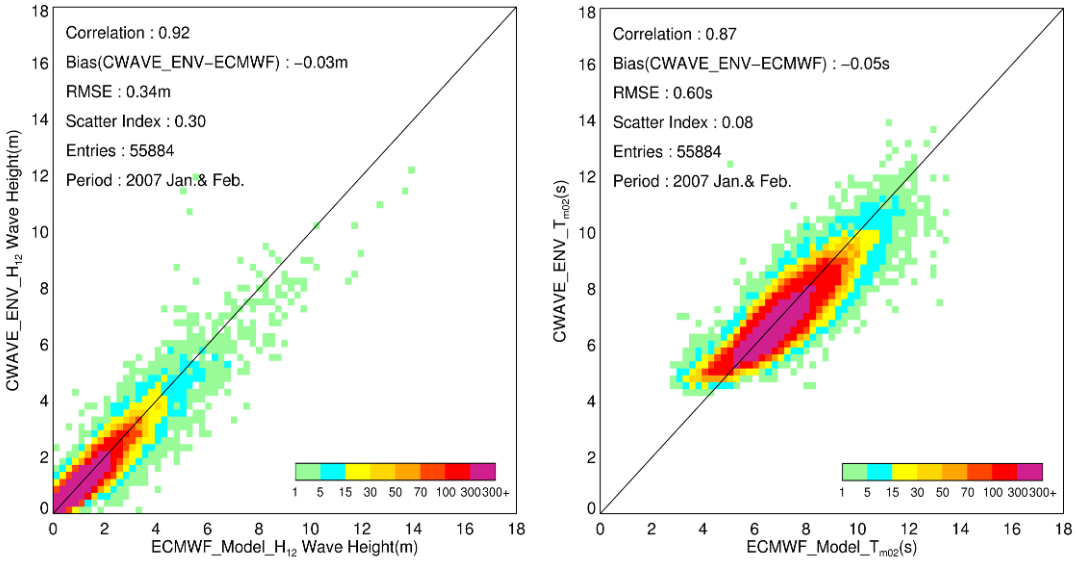

(a) (b)

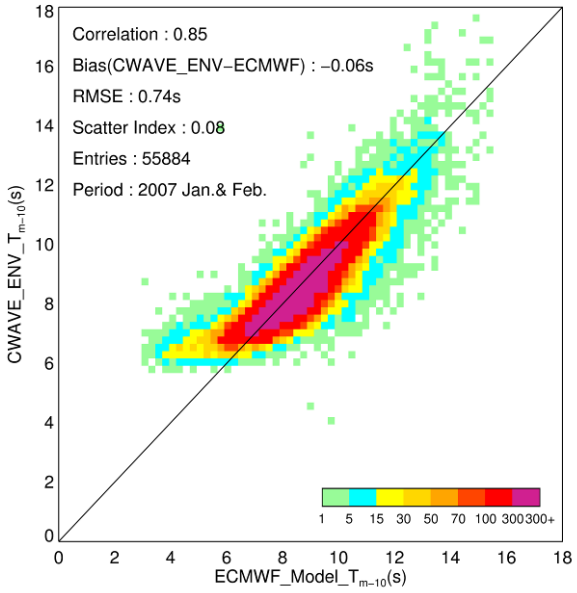

(c)

Figure 7. 7 Scatter Plots of wave height H_{12} (a), T_{m02} (b) and T_{m-10} (c) derived by CWAVE_ENV compared to the ECMWF reanalysis model in January and February 2007

As ASAR images are often requested as well for other modes (e.g. image mode with 100 km by 100 km swath coverage) which is exclusive to the wave mode in offshore regions, we are following the idea of extending the CWAVE_ENV algorithm to image swath ASAR data to retrieve sea state parameters. Thus coastal wave power statistics will become available. This is interesting for many coastal applications.

In Tab. 7.2, the statistics of the comparisons to both wave models are summarized. Integral wave parameters given by CWAVE_ENV have nearly zero bias when compared to models. T_{m02} has the smaller scatter index of 8%, while it has the highest bias of -0.05 s and RMSE of 0.59 s in the triple comparisons.

Table 7. 2 Statistics obtained by the CWAVE_ENV algorithm vs. ECMWF model and DWD model for SWH (m), H_{12} wave height (m), T_{m02} (s), T_{m-10} (m) in January and February 2007. Bias is with respect to observations and SI indicates scatter index.

	CWAVE_ENV vs. ECMWF model				**CWAVE_ENV vs. DWD model**			
Statistical Para.	Cor.	Bias	RMSE	SI	Cor.	Bias	RMSE	SI
SWH	0.93	-0.02 m	0.43 m	0.16	0.90	-0.05m	0.51m	0.18
H_{12}	0.92	-0.03 m	0.34 m	0.30	N/A			
T_{m02}	0.87	-0.05 s	0.60 s	0.08	N/A			
T_{m-10}	0.85	-0.06 s	0.74 s	0.08	N/A			

- **Comparison to the PARSA inversion scheme**

The validation of nonlinear PARSA retrieval approach itself has been demonstrated in chapter 6. In this section, SWH and mean period T_{m02} derived from the two SAR ocean wave algorithms are compared. In Fig. 7.8 (a) and (b) the comparison results are presented. The plots demonstrate that even without first guess information from models the CWAVE_ENV still yields reliable ocean wave parameter estimates, though it seems that there is underestimation in the extreme high sea state. Validation of both SAR algorithms is needed to be carried out with a focus on extreme sea states, where different SAR algorithms and models all have quite different behaviors.

- **Comparison to ESA Level2 Products – WVW**

After the validation of WVW products performance as demonstrated in chapter 6, it is no surprise that there is distinct difference between CWAVE_ENV and WVW retrieved results as shown in Fig. 7.9 (a) and (b) for SWH and H_{12}. In spite it is argued

that the WVW spectra results are only available for the longer wave information resolved by the ASAR sensor, it still cannot provide the reliable sea state measurements in many cases.

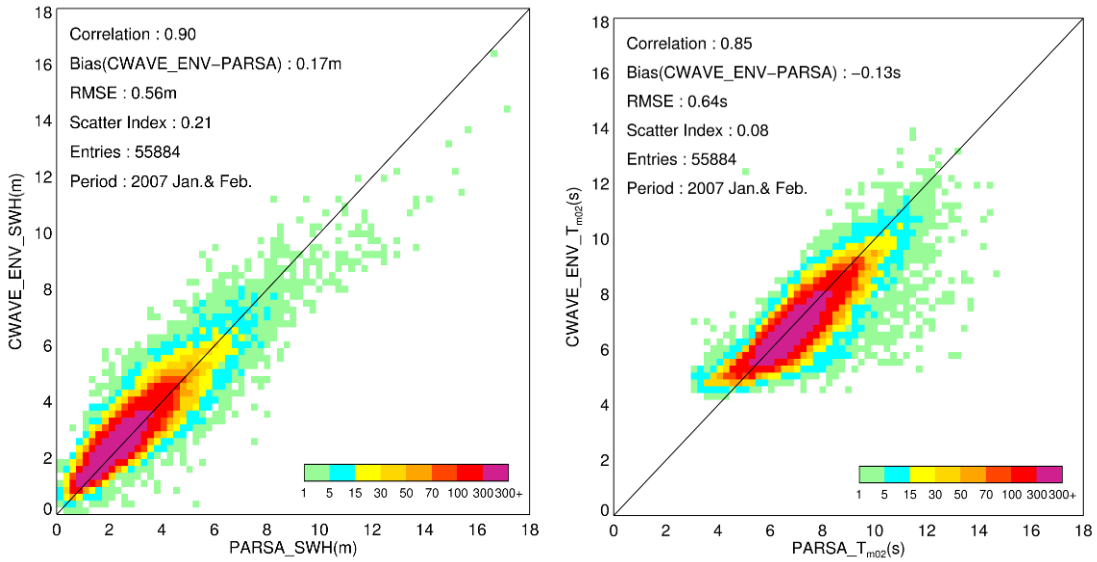

(a) (b)

Figure 7. 8 SWH (a) and T_{m02} (b) derived by the PARSA inversion scheme compared to the CWAVE_ENV algorithm in January and February 2007

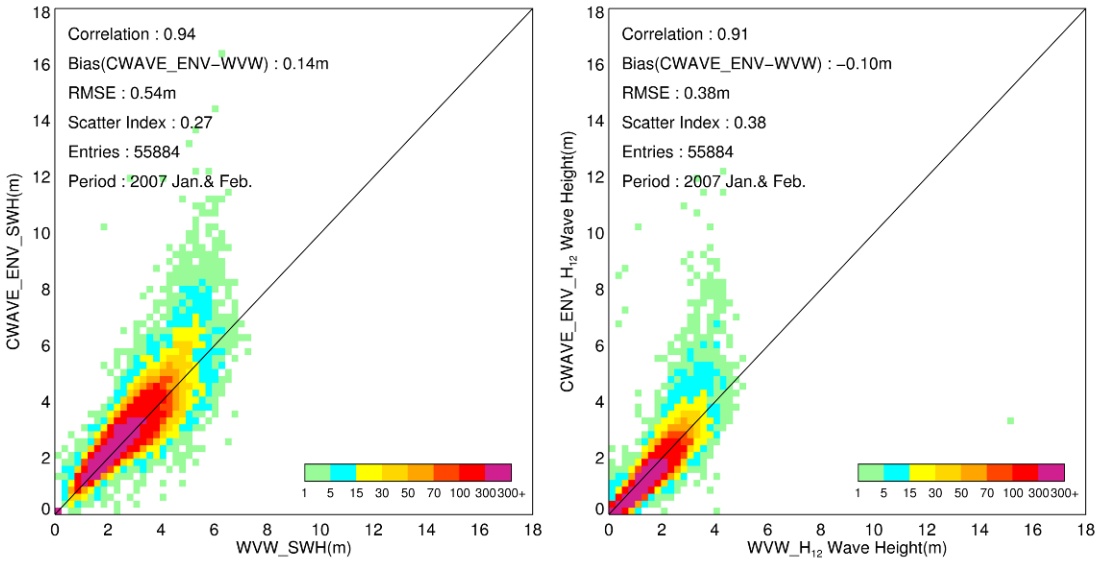

(a) (b)

Figure 7. 9 SWH (a) and H_{12} (b) derived from ESA Level2 WVW spectra compared to CWAVE_ENV algorithm results in January and February 2007

- **Comparison to radar altimeters**

As mentioned in the introduction part, RA is another radar remote sensing instrument that can provide accurate SWH measurements. In this section, cross validation of SWH retrieved by CWAVE_ENV is carried out. Measurements acquired from JASON-1 and GEOSAT Follow on (GFO) missions during January and February 2007 are used. The data are acquired via the CERSAT database and the corrected SWH is used.

For JASON-1, the corrected result is $SWH\_corr = 1.0429 * SWH + 0.0266$ and for GFO, the respective equation is $SWH\_corr = 1.0625 * SWH + 0.0754$ [*Queffeulou*, 2004].

The time window chosen for ASAR wave mode data collocated to RA is 1 hour and the distance is less than 100 km. The crossover sea state measurements derived from GFO and JASON-1 are fully independent for the retrieved SWH from ASAR data. Within an area with a radius of 100 km, several RA single point measurements are collocated to the ASAR wave mode data. Therefore, the averaged SWH during the collocation cells and single SWH from the nearest point are both compared to the result derived by the CWAVE_ENV from the ASAR wave mode data. Fig. 7.10 and Fig. 7.11 are retrieved SWH compared to GFO and JASON-1, respectively.

One can observe that all the comparisons are in very close agreement. The overall bias is around 0.10 m and RMSE is around 0.50 m. The correlation is higher than 90%, and the scatter indices are 17% and 13% for comparisons to GFO and JASON-1, respectively. Thus the SWH derived by the empirical model from ASAR data and altimeter measurements are of the same quality.

In this section, sea state parameters retrieved by CWAVE_ENV algorithms are compared to different datasets. The comparisons show that the integral wave parameters derived from ASAR wave mode data are reliable and independent. It can be used as another dataset for global wave statistical analysis.

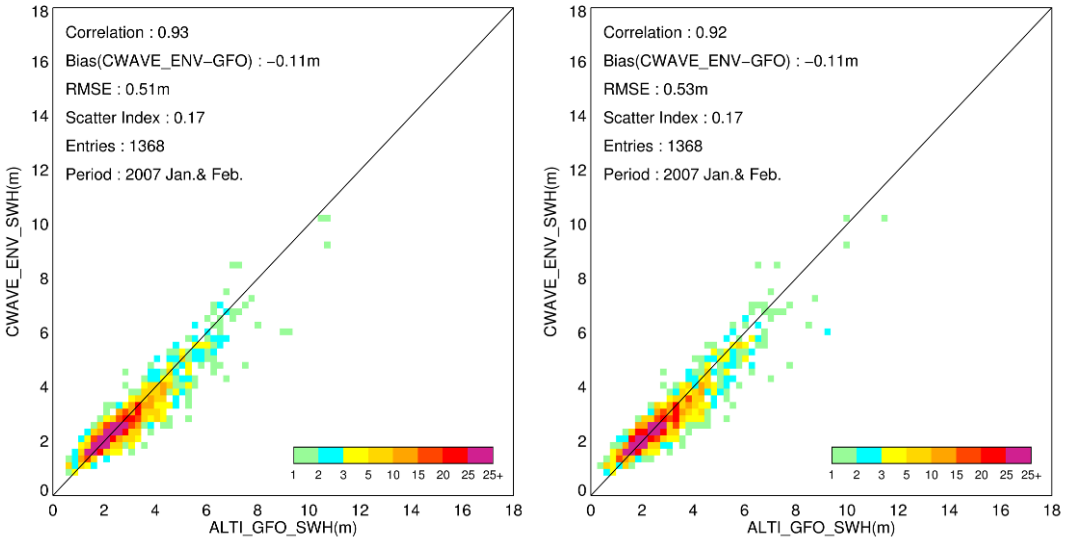

(a) (b)

Figure 7. 10 Scatter Plots of SWH derived by CWAVE_ENV compared to the measurements of RA GFO. (a) is the comparison to the averaged SWH within the collocation cells and (b) is for the single SWH of the nearest point to ASAR wave mode data in January and February 2007

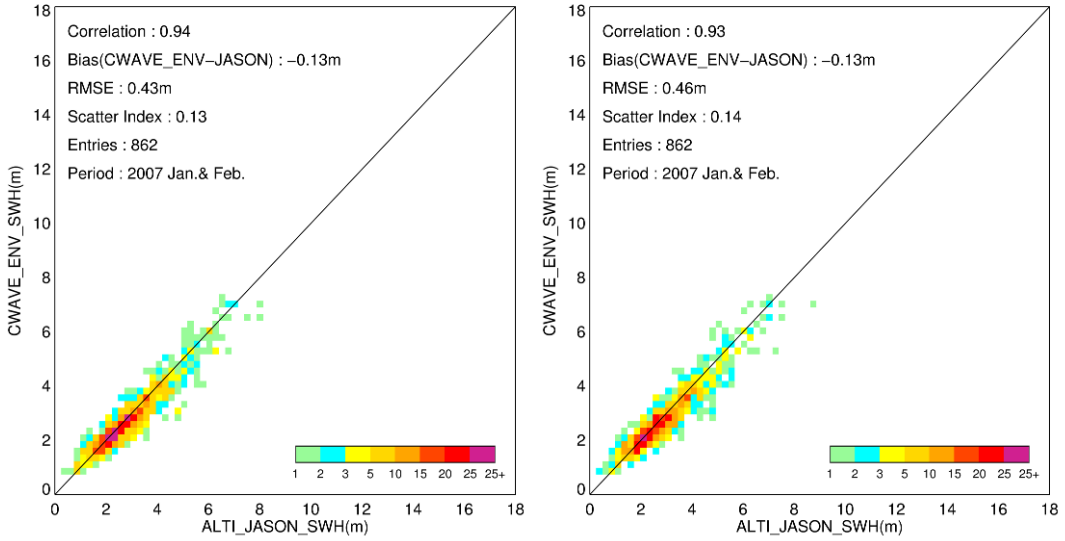

(a) (b)

Figure 7. 11 Scatter Plots of SWH derived by CWAVE_ENV compared to the measurements of RA JASON-1. (a) is the comparison to the averaged SWH within the collocation cells and (b) is for the single SWH of the nearest point to ASAR wave mode data in January and February 2007

7.4. Case studies

Two case studies are investigated in this section, a severe storm that occurred over the North Atlantic on Feb. 10th, 2007; and the La Reunion extreme swell event, which was generated by a distant storm in south of Cape Town, South Africa. Both cases are analyzed using wave model outputs, double tracks of ASAR and RA-2 onboard the ENVISAT satellite. With respect to the storm case, performances of different SAR retrieval algorithms in extreme wind speed and sea state are compared to wave model results. In the La Reunion case study, we investigate ASAR measurements over a storm, which generated high swell across the entire Indian Ocean basin. Based on the empirical swell propagation law, the capability of ASAR wave mode data to be used for early warming system is analyzed as well.

7.4.1 North Atlantic storm event

In this section, a North Atlantic storm event is investigated in detail by using ASAR wave mode data, RA data and DWD forecast wave model results. Fig. 7.12 shows radar measurements and wave model results for the event. In (a) and (c) of the figure, SWH of the DWD forecast model results at 0:00 and 12:00 UTC are shown as the background, on which collocated SWH measurements from the double tracks of ASAR and RA-2 are superimposed. ASAR provides sea surface measurements in right looking mode, thus its surface track is around 300 km away from the nadir measurements of RA-2. At 0:00 UTC, the eastern track is the one of ASAR. Due to ascending and descending orbits, it becomes the western track in the descending case at about 12:00 UTC.

SWH derived from radar measurements and model forecast results through the western high wave system is analyzed in the following. SWH derived from ASAR and RA-2 data along the tracks are represented by different curves in Fig. 7.12 (b) and (d) for 0:00 and 12:00. For SWH retrieved by the ASAR algorithms, estimation by using the CWAVE_ENV algorithm are shown in a blue line, the nonlinear retrieval algorithm PARSA and the Level2 WVW products are shown in brown and yellow ones respectively. The DWD model results collocated with the ASAR track is plotted as well as a pink line.

Estimation of SWH derived from RA-2 Ku-band is also used for comparison. It is represented by green lines in the plot and pink dashed lines used to denote its

collocated DWD model results. As RA-2 has the nadir footprints which are 300 km away from the ASAR measurements, the wave model results collocated to the RA-2 is different to the ones for the ASAR track.

Both curve plots show that SWH derived from ASAR wave mode data and RA-2 have quite good agreement with wave forecast model results when sea state is lower than 6 m. In high sea state, the differences are quite obvious though. At 0:00 UTC, the ASAR track is crossing the area of the wave system yielding high SWH. The PARSA algorithm provides the highest value of 11.4 m while WVW product has a large underestimation and yields only 5.7 m. The differences of using the ASAR algorithms to estimate SWH in high sea state is investigated in detail as follows.

ASAR wave mode data are acquired along the orbit every one hundred kilometres to provide sample and instantaneous measurement over sea surface. To avoid high variations for SWH estimation using ASAR wave mode data in the high sea state, an averaging way is used. In the ascending pass of ENVISAT at around 0: 15 UTC, five data pairs of ASAR measurements and collocated DWD model located in the region between 42.32°N and 45.85°N which is near to the high wave system are linear averaged avoiding the effect of sampling of ASAR measurements. In the descending pass at around 12:40 UTC the area is chose as between 43.47°N to 49.63°N where eight data pairs are located with all wave heights higher than 7.0 m.

The averaged SWH measurements derived from different algorithms and collocated DWD model results for both tracks are given in Tab. 7.3.

Table 7. 3 The averaged SWH estimated from different ASAR algorithms and DWD model results in the higher wave field for ascending and descending pass

	CWAVE_ENV	PARSA	WVW	DWD model
Ascending Pass (at about 0:20 UTC)	8.5 m	9.6 m	5.7 m	8.4 m
Descending Pass (at about 0:20 UTC)	10.9 m	11.4 m	5.1 m	10.2 m

For the both tracks, the CWAVE_ENV algorithm shows the capability to derive reliable measurements even in this extreme sea state, while the WVW products cannot be used to measure high sea state. Even when the SWH is lower than 5 m, the WVW

products have a positive bias compared to other algorithms and model results, which is particularly obvious in the descending pass as shown with the yellow line in Figure 14 (d). Therefore, from this case study, one can conclude that the WVW has a substantial under estimation in high sea state and rather overestimation in low and moderate sea state.

The PARSA algorithm yields higher estimation of SWH in both tracks than the DWD wave model and the CWAVE_ENV results. Moreover the positive bias increases significantly along with the sea state. The PARSA algorithm is implemented using the priori information from the ECMWF reanalysis wave model, in which the ASAR wave mode cross spectral information and RA measurements have been assimilated. The PARSA algorithm might have an overestimation due to instantaneous measurements in comparison to averaged model results. This needs to be further validated.

At around 12:35 UTC, the RA-2 track was very near to the high wave system and yields the an estimation of SWH of 18.9 m, which is 2.9 m higher than the DWD model forecast result. For this high sea state, performance of different ASAR algorithms to derive SWH is investigated in detail, particularly to evaluate the CWAVE_ENV algorithm and the existing WVW Level2 products. CWAVE_ENV results for both passes show reliable measurements of SWH in different and variable sea state.

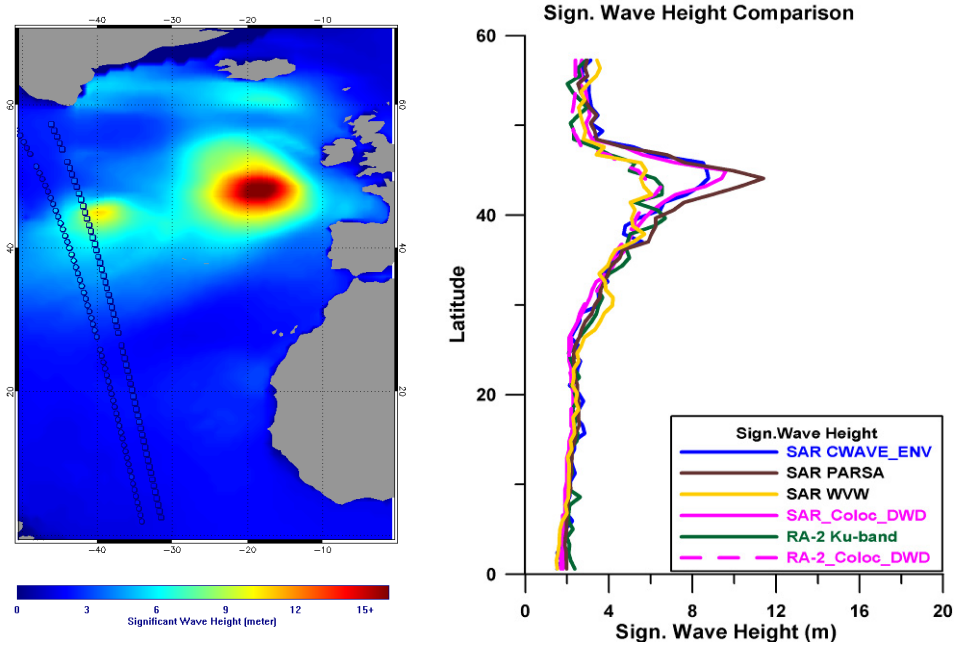

(a) (b)

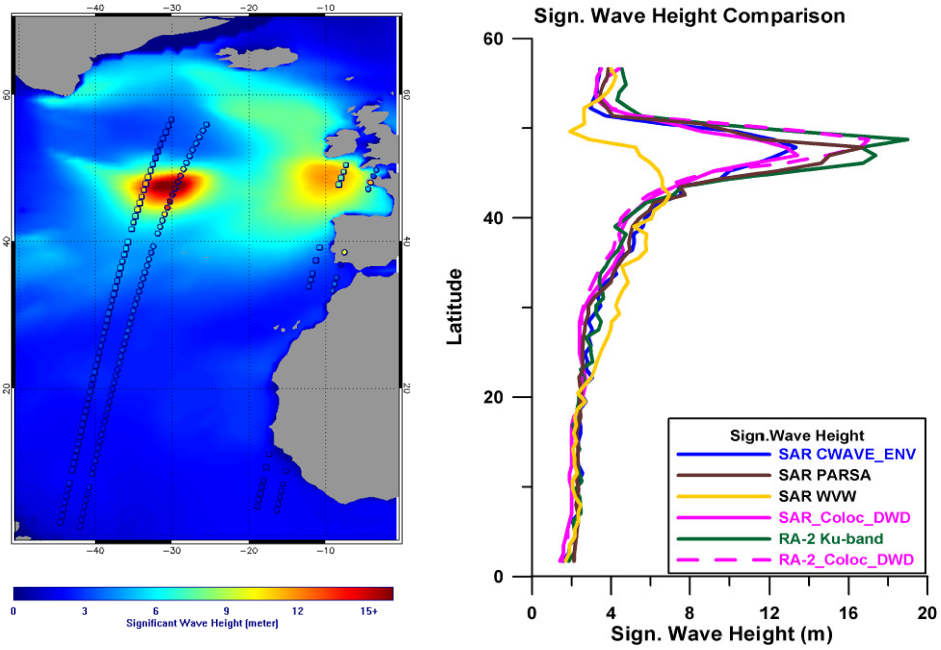

(c) (d)

Figure 7. 12 Comparison of significant wave height derived from DWD forecast model, ASAR wave mode data and RA-2 Altimeter data for North Atlantic Storm on 10 Feb. 2007. (a): DWD forecast model at 0:00 UTC superimposed with ASAR (eastern) and RA-2 tracks; (b) SWH derived from ASAR track using different algorithms, RA-2 and collocated DWD model results at 0: 00 UTC; (c) The same with (a) while at 12:00 UTC; (d) The same with (b) while corresponding to the tracks acquired at 12:00 UTC

This case study shows that quality of retrieved sea state parameters by CWAVE_ENV is comparable to RA measurements and to the SAR nonlinear retrieval approach, although no priori information is used. Double tracks of ASAR and RA can be used jointly to validate the wave model performance as well as for data assimilation under the condition that a suitable algorithm for ASAR is adopted. In respect to the CWAVE_ENV algorithm, one issue that needs to be further investigated is the performance in extreme sea state for extended datasets.

7.4.2. Indian Ocean swells case

On the evening of May 12th, 2007, a series of very high waves damaged the coasts of La Reunion island (21° S, 55°20’ E) and neighboring island in the Indian Ocean. The extreme swell with peak period of up to 19.5 s reached maximum individual height of 11.3 m and 6.4 m of SWH [*Lefèvre and Aouf*, 2007].

The extreme swell is generated by a severe storm around 40°S, 30°E in the south of Africa as shown in Fig. 7.13 with wind (a) and wave field (b) given by the DWD forecast model on May 10th, 2007 at 06:00 UTC. The storm engendered swell, which propagated through the Indian Ocean covering about 1000 km/day, hitting the La Reunion.

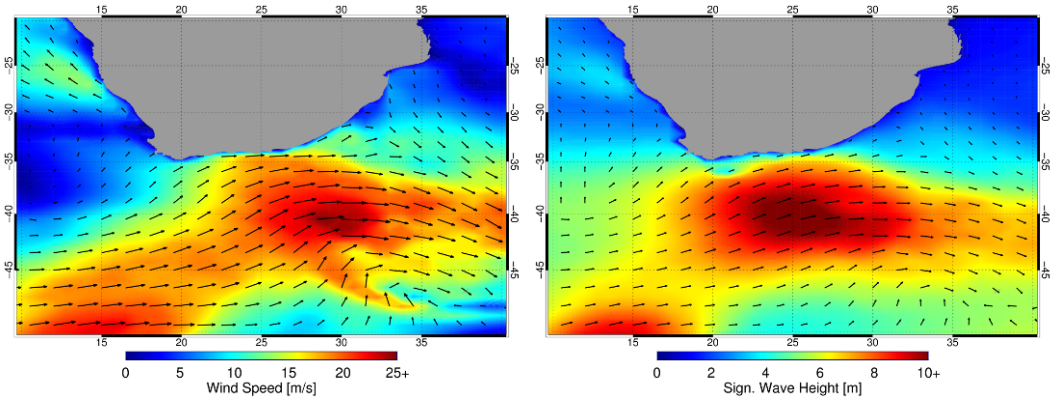

Figure 7. 13 Wind field (a) and SWH (b) with direction of windsea of DWD forecast model on May 11th, 2007 at 6:00 UTC

Early warning of extreme wave using ASAR Wave Mode data

In Fig. 7.14, SWH measurements derived from both tracks of ASAR wave mode data using CWAVE_ENV algorithm and RA-2 data are superimposed on collocated DWD forecast model results. Time difference between the ENVISAT track and the DWD model is around 1.5 hour.

Compared to Fig. 7.13, one can observe that the storm was moving toward northeast and spanned quite a large region of more than 1000 km. The ENVISAT tracks cross the area of the storm at around 19:45 UTC on May 11th. The highest SWH measured along the ASAR track is 9.2 m located at 32.2°S, 4.7°E. A high swell system traveled to the northeast and arrived at La Reunion island on May 12th at around 16 UTC after traveling 1700~2000 km. Using a straightforward wave propagation relationships introduced by *Dietrich et al.* [1975] (as shown in Fig. 2.5 in Chapter 2), about 5 m waves can be forecasted in La Reunion island at around 12:00~16:00 UTC on May 12th. This shows good agreement with in situ and reanalysis model, which yields 6 m [*Lefèvre and Aouf*, 2007].

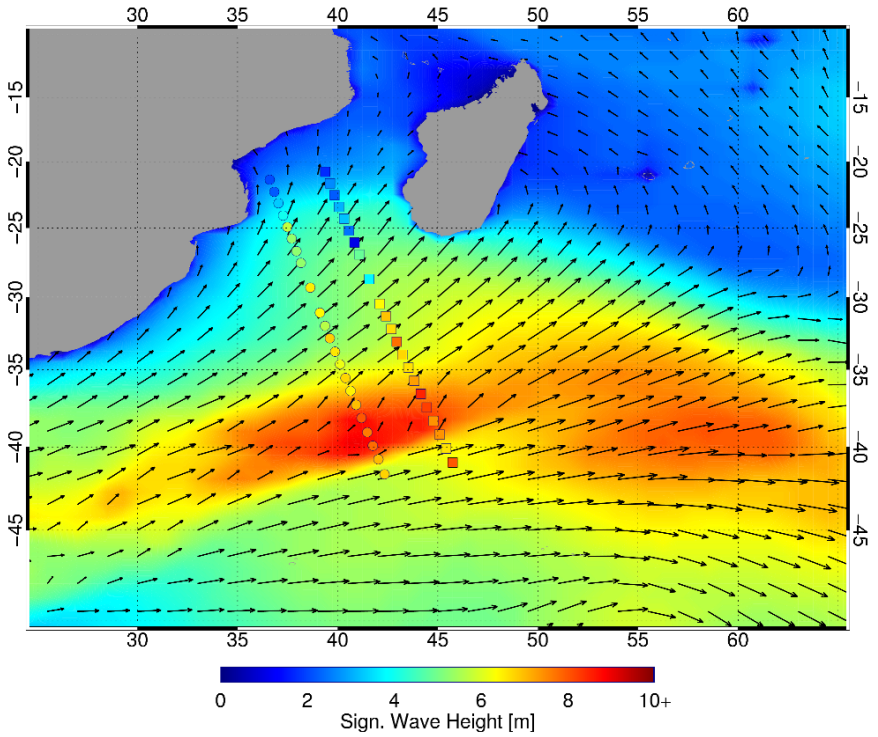

Figure 7. 14 Significant wave height and swell direction of DWD model on May 11th, 2007 at 21:00 UTC. Double tracks of ASAR wave mode (squares) and RA-2 (circles) at around 19:45 UTC are superimposed.

In this case, around 20 hours earlier the extreme swell arriving at La Reunion island can be forecasted by ASAR wave mode measurements derived from the CWAVE_ENV algorithm. The ASAR wave mode data also may be used together to cross validate thus an extreme wave early warning system is possible.

7.5. Conclusions

An empirical algorithm CWAVE_ENV to estimate integral wave parameters from ASAR wave mode data without priori information is presented in this paper. The empirical model function is tuned using globally distributed ASAR wave mode data and collocated ECMWF reanalysis model results. The tuning approach is implemented using stepwise regression method to select ASAR image parameters. The geophysical model coefficients are derived by cost function minimization.

Validation of the CWAVE_ENV algorithm is carried out by comparison against *in situ* buoy measurements, numerical wave model, ENVSIAT/ASAR WVW Level 2

products and crossover RA measurements. Validation results show that the accuracy of integral wave parameters retrieved by the CWAVE_ENV algorithm has the quality of the RA measurements and is near to *in situ* buoy measurements. Brief summary of the algorithm validation is given in following.

(1) SWH retrieved from ASAR data compared to buoy *in situ* measurements are divided into comparisons in deep water and shallow water. In deep water, retrieved SWH has a good correlation of 0.9 to buoy measurements, a reasonable RMSE of 0.70 m and 24% for SI. The comparison in shallow water yields rather high RMSE of 1.0 m and SI of 33%, due to the limitation of the reanalysis wave model data in the empirical model tuning.

Investigating the comparison of the CWAVE_ENV algorithm in different sea state demonstrates that the algorithm has good performance in rough sea state (with SWH higher than 2.0 m), while has an overestimation around half meter in the rather low sea state for SWH less than 1.25 m.

(2) SWH, H_{12} wave height and T_{m02} compared to the ECMWF reanalysis models are also presented. CWAVE_ENV results have a low bias of -0.02 m and -0.03 m for SWH and H_{12} and RMSE of 0.43 m and 0.34 m respectively, while the wave period comparisons show a very low SI of 8%.

As the DWD wave model is independent of ASAR information, comparison of SWH estimated by the CWAVE_ENV to the DWD wave model, with a small bias of -0.05 m and SI of 18%, shows more realistic results than the comparison to the ECMWF reanalysis wave models, which is using the in situ measurements and satellite data in the assimilation scheme.

(3) Retrieved results of SWH and H_{12} by the CWAVE_ENV are also compared to the ASAR wave mode Level2 products. The comparison results reveal that the existing Level2 products significantly underestimate SWH and the measurements vary with the change of ASAR cut-off wavelength.

(4) RA measurements from GFO and JASON-1 missions are also used for the validation of the CWAVE_ENV algorithm. Crossover measurements from the RA are collocated to the ASAR wave mode data. Bias of around -0.1 m and RMSE of around 0.5 m are found for both comparisons. Low scatter indices of 13% and 17% are achieved when compared to GFO and JASON-1 respectively. Few cases over extreme

sea state with SWH of around 10 m have consistent results from the ASAR wave mode and GFO data.

The results of the two case studies for extreme wave conditions thus demonstrate that the CWAVE_ENV algorithm performs well under extreme sea states.

In the North Atlantic storm event case, the SWH given by ASAR and RA-2 are compared to the DWD forecast wave model. All measurements derived from radar and models agree well along the orbit, but for the extremely high sea state within the storm there are distinct differences. CWAVE_ENV results agree well with the DWD model results, but are around half meter higher for SWH above 7 m. Both RA-2 and ASAR PARSA results are higher than the wave forecast with a bias of more than 1 m in extreme sea state. The ASAR standard Level2 products WVW show a significant underestimation of wave height in storm areas.

The analysis of the high swell case at La Reunion island demonstrated that ASAR wave mode data can be used as a forecasting tool for extreme waves contributing to a global early warning system.

Despite of the overall good quality of integral wave parameters derived by CWAVE_ENV algorithm, the assessment is based on a three months period. Therefore, a more intensive validation by *in situ* buoy measurements, cross over RA measurements is needed to confirm its performance under extreme sea state conditions.

Chapter 8

Investigation of Coastal Surface Wave Using TerraSAR-X Data

The content of following Chapter has been published entitled "***Investigation of Ocean Surface Wave Refraction Using TerraSAR-X data***", in *IEEE transaction of Geosciences and Remote Sensing*.

In the previous chapters, surface wave measurements are performed globally by using SAR wave mode data, which are typically acquired over the open sea and the individual SAR images have small coverage of only 5 km by 10 km. In the open sea, water depth is large enough that has little effect on the surface wave signatures. However in the near-shore regions, where depth is much smaller and changes rapidly, effect the wave propagation, shape and height. In this chapter, coastal waves are investigated using wide swath SAR data.

As a scientific and technological continuation of the X-SAR and SRTM missions, the new X-band SSAR TerraSAR-X was launched on June 15, 2007. Since then it has provided numerous high-quality data over land and ocean operationally.

In the present study, surface wave refraction and diffraction is investigated using TerraSAR-X imagery acquired over the coast of Terceira island situated in the North Atlantic. Peak wavelength and wave direction are determined by SAR two-dimensional image spectra and compared to measurements of X-band marine radar and results of the numerical wave model WAM. SWH in the near-shore shallow water region is estimated from TerraSAR-X data following the wave refraction laws and using the developed XWAVE empirical algorithm. Image spectra of the TerraSAR-X scenes in the full-coverage region are given to investigate significant changes of wave direction and length.

By analyzing another TerraSAR-X image acquired in StripMap mode, a shadow zone in the lee side of Terceira island is identified. It is influenced jointly by wave refraction and diffraction. Furthermore, a cross sea pattern revealed in the image spectra is investigated. The cross sea is generated by the diffracted wave rays from the

northern and southern coasts of the island. Less wave directional spreading for the cross sea situation is observed as well when compared to the image spectra at the origin of diffraction.

8.1. Introduction of TSX data

In June 2007, the TerraSAR-X (TSX) satellite reached its orbit and from January 2008, data and products were provided operationally to scientists (http://sss.terrasar-x.dlr.de/). TSX has a sun-synchronous, near-polar dusk-dawn orbit with a mean altitude of 514 km. It can be operated in four different modes, i.e. ScanSAR, StripMap, Spotlight and High-Resolution (HR) Spotlight. Technical details of the different modes are summarized in Tab.8.1.

Table 8. 1 Imaging characteristics of TSX in different modes

	ScanSAR	**StripMap**	**Spotlight**	**HR Spotlight**
Swath Width (ground range)	100 km	30 km	10 km azimuth x 10 km ground	5 km azimuth x 10 km ground
Incidence angle	20°-45°	20°-45°	20°-55°	20°-55°
Azimuth Res.	16 m	3 m	2 m	1 m
Ground Range Res.	1.7 m-3.5 m	1.7 m-3.5 m	1.5 m-3.5 m	1.5 m-3.5 m

Because of its flexible swath coverage and high resolution as well as the interferometric and polarimetric abilities, various oceanic and atmospheric applications can be investigated using TSX data, for example, the preliminary studies of ocean surface wind, coast lines, and surface waves as described in [*Lehner et al.*, 2008].

As a unique sensor to image sea surface in two dimensions independent of weather and sunlight conditions, airborne or spaceborne SARs are suitable for investigating the spatial variations of surface waves, particularly in near-shore regions, where the local bathymetry, surface wind and surface currents have active interactions with oceanic gravity waves. SAR data have been used to study the ocean wave refraction mechanisms in coastal regions caused by, e.g. bottom topography [*Lodge*, 1983], ocean currents [*Irvine and Tilley*, 1998; *Li et al.*, 2002] and ice edges [*Liu et al.*,

2001; *Schulz-Stellenfleth and Lehner*, 2002].

In the present study, Terceira island is chosen as the area of interest (AOI) for observation of coastal waves by making use of TSX images acquired in different modes. Terceira island is located in the Azores archipelago between latitudes 37º to 40º N and longitudes 25º to 31º W. At the north of the Azores, the dominant wave direction is from north/northwest, as generated by high-latitude storms in the North Atlantic. Distributions of these waves change locally in shoaling, refraction and diffraction processes because of the quickly varying bathymetry at a short distance from the coast line.

The volcanic island Terceira has an elliptical form approximately 29 km in the E-W direction and 18 km in the S-N direction as shown in Fig.8.1. Three quick looks of TSX images acquired over the island operated respectively in ScanSAR, StripMap and Spotlight mode overlaid on top of each other are shown as well in the figure. The ScanSAR image has the largest area coverage of 140 km and 100 km in azimuth and range direction, respectively, with a pixel size of 8.25 m. Wind streaks are visible in the ScanSAR image, and surface wind blowing toward northwest is inferred by the shadow zone behind the Santa Barbara volcano (1021 m) at the NW end of the island. Details on the retrieval of the surface wind field from X-band SAR data are discussed in [*Lehner et al.*, 2009]. The ScanSAR image yields an overview of sea state and wind field for the entire oceanic region around Terceira island.

Inside the black rectangle, a quick look of a StripMap image acquired on January 15, 2009 in the eastern coast of Terceira island is shown. A Spotlight image represented in the white rectangle was acquired on March 26, 2008. The Spotlight image covers the area limited to 5 km in azimuth and 12 km in range over the harbor of Terceira island. Spotlight mode data are particularly suitable for investigation of near-shore processes, harbor monitoring, and comparison to in situ measurements. It can be observed that the StripMap mode scene covers the whole eastern part of the island and can be used for investigating spatial variations of wave refraction when approaching the coasts.

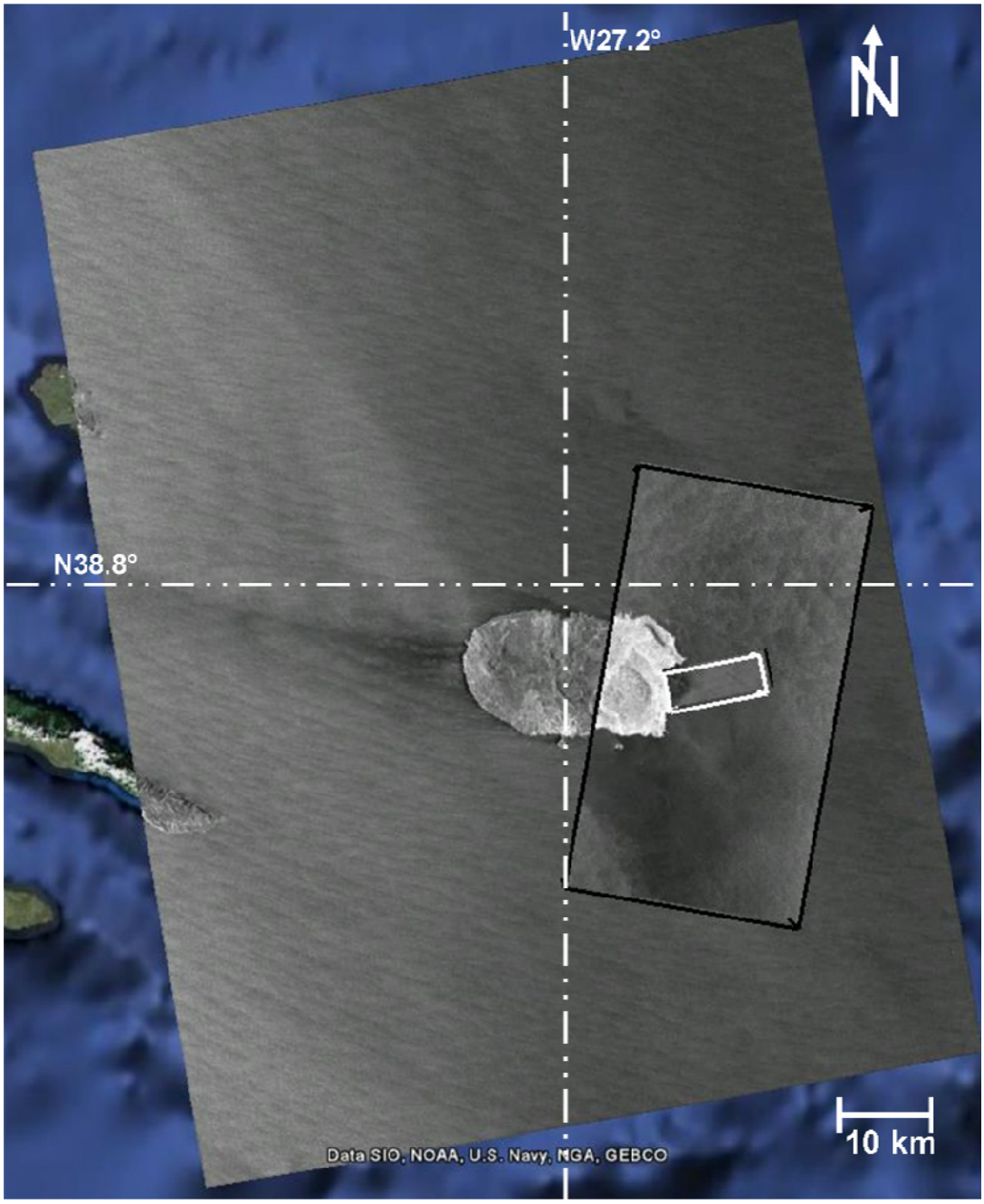

Figure 8. 1 Overlay of TSX ScanSAR (largest one) image acquired on March 20, 2008, StripMap image (in the black rectangle) acquired on January 15, 2009 and Spotlight mode image (in the white rectangle) acquired on March 26, 2008 over Terceira island (map in background © Google earth)

Wave refraction caused by the change of bottom topography around the Terceira island coasts is investigated using TSX image spectra and measurements of X-band marine radar. The image spectrum extracted from the TSX Spotlight image in offshore direction shows a swell system with peak wavelength of 181 m and peak

wave direction of -34° (clockwise relative to the TSX azimuth direction) generated by a high-latitude storm whereas the one in the near-shore region shows a rotation of peak wave direction of 36° and the peak wavelength decrease of 128 m, induced by the wave refraction.

The spatial variations of wave diffraction around the entire island are investigated using a TSX image acquired in StripMap mode on January 15, 2009, and compared to the variation in bottom topography.

8.2. Auxiliary data

8.2.1. WaMoS Marine Radar

In the present study, local sea state measurements are derived from the second-generation marine radar WaMoS II, which is an operational wave monitoring system to survey the sea surface wave field in time and two-dimensional space. The system consists of a conventional marine radar, an A/D converter to digitize the analog radar echo signal and a standard PC to store and process the data in real time. It is used onboard ships, oil platforms, and on shore to determine two-dimensional wave spectra and integrated sea state parameters, such as wave peak, propagation direction and SWH. The technique as presented in [*Young et al.*, 1985; *Nieto et al.*, 1999; *Nieto et al.*, 2004] has been used operationally in many locations.

The WaMoS II located on Terceira island was installed in Praia da Vitória Bay (38.7°N, 27.0°W) with a scanning radius of 2.2 km. The blue dash line demonstrates the coverage of WaMoS marine radar over the port superimposed on the subscene of the StripMap mode image shown in Fig. 8.2.

WaMoS provides a local sea state measurement, whereas the numerical wave model gives an estimation of sea state over a large spatial scale. To verify ocean wave characteristics observed in the TSX image, the numerical wave model WAM is used to provide synergetic observations.

8.2.2. Topography Dataset

Bathymetry data used in the present study for investigating coastal wave processes are extracted from the National Geophysical Data Center (NGDC) ETOPO1 global relief

model [*Amante and Eakins, 2008*] in grid points. The spatial resolution of ETOPO1 model is 1 arc-minute.

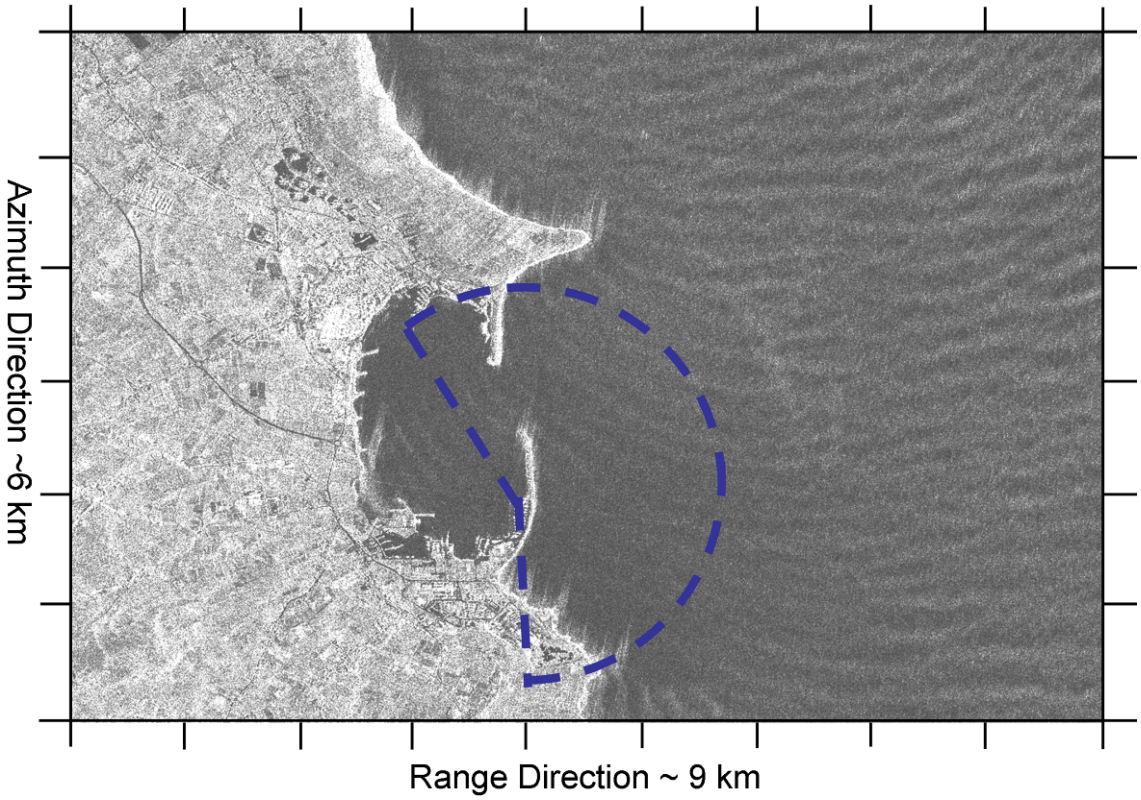

Figure 8. 2 Demonstration of the location and scanning coverage of WaMoS marine radar at the port of Terceira island (Blue dash line superimposed on subscene with coverage size about 6 km by 9 km of TSX StripMap shown in Figure 8.1.)

8.3. Observation of wave refraction and diffraction in TSX images

General mechanisms of wave refraction and diffraction in shallow water have been introduced in Chapter 2. In the following, detail analyses for coastal wave processes observed by TSX are presented.

8.3.1. Observation of wave refraction and diffraction by TSX

In this section, TSX observations of wave refraction and diffraction are demonstrated. A TSX Spotlight image acquired on March 26, 2008, is used first for analyzing the wave refraction.

In Fig. 8.3 (a) SWH of the total sea, peak wavelength, and wave direction of swell and windsea wave components derived from the DWD GSM model on March 26,

2008, at 18:00 UTC is shown. The model results are approximately 1.5 hour earlier than the acquisition of the TSX Spotlight image.

The gray areas on the map indicate the position of the Azores archipelago. SWH in this region is in the range of 2.0 m to 2.5 m as given by the wave model. One storm with SWH higher than 6 m located approximately 1000 km northwest generates long swell propagating toward southeast. Swell (marked with a dash-dot line) with wavelength around 180 m is observed in the local region of Terceira island as shown in Fig. 8.3 (b), where the windsea becomes as low as 0.5 m. The sea state of Terceira island at this time is dominated by a swell wave system.

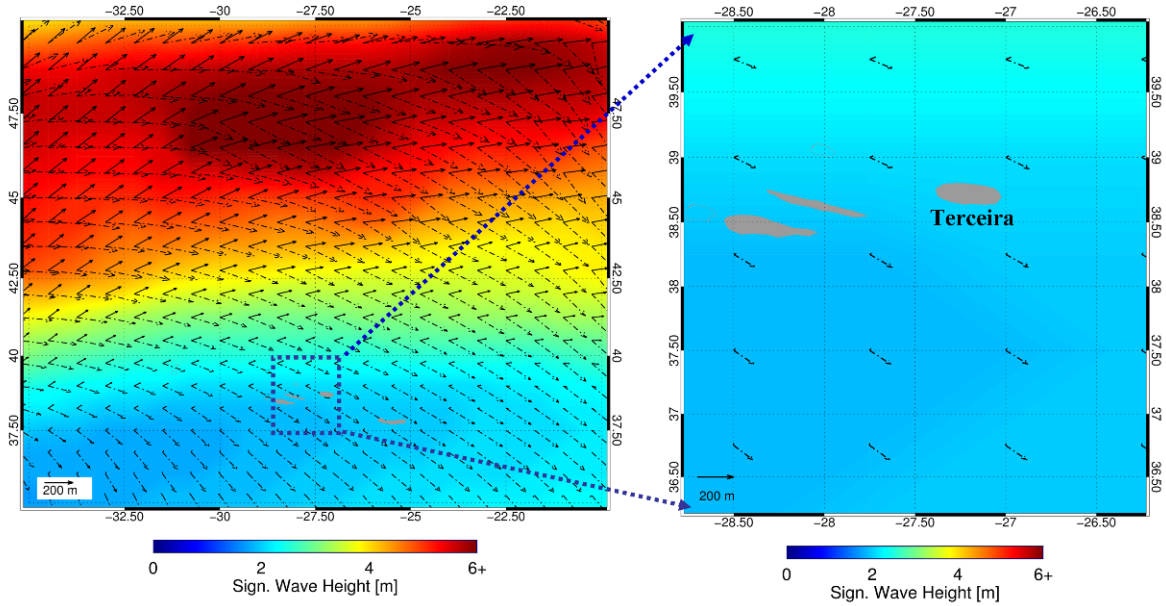

(a) (b)

Figure 8. 3 SWH (background), Peak wavelength and direction for windsea (solid line) and swell (dash-dotted line) derived from the DWD GSM wave model for large coverage (a) and for the subscene of Azores Islands (b) on March 26, 2008 at 18:00 UTC.

In Fig. 8.4, the TSX Spotlight image acquired over the Terceira eastern coast in an ascending orbit is superimposed with topography data derived from the ETOPO1 model. The coverage of the TSX Spotlight image is approximately 5 km in azimuth and 12 km in range with a resolution of 2.8 m and 3.5 m, respectively, at a pixel size of 1.25 m. Five subscenes A, B, C, D and E with 1024 by 1024 pixels covering an

area of around 1 km by 1 km shown on the TSX image are used for demonstration of the spectral analysis. A standard Fast Fourier Transform (FFT) method is used for the estimation of image spectrum. Between B and D, the TSX image is divided into four rows and six columns, with the same size of 1024 by 1024 for every subscene. The image spectra for the subscenes are shown in Fig. 8.5 to follow the spatial variations of gravity waves in the near-shore region. For the plots in Fig. 8.5, the spectral density value is scaled relatively to the reference maximum.

The spatial resolution of the DWD GSM wave model is 0.75º x 0.75º, and the estimation for the integrated wave parameters to the nearest grid in the TSX image is located at 39°N, 27°W, which is approximately 30 km away from the TSX image subscene D. SWH, peak wavelength and direction as estimated by the DWD GSM model is 2.1 m, 176 m, and -45° (clockwise to the TSX azimuth direction), respectively. The same peak resolved by the DWD model is observed as well in the TSX image, as shown in its image spectra D in Fig. 8.5, denoted by **P1.** Peak wavelength and direction derived from the TSX image spectra of D is 181 m and -34°, respectively, which is comparable to the numerical wave model results.

From right to left in the first row of Fig. 8.5, peak wave direction and wavelength show a significant change as observed in the spectra. Spectrum D agrees with model results in offshore with peak wave direction of -34°, whereas along the distance toward the inshore, the peak undergoes a clockwise rotation as observed in the spectrum B for peak wave direction of 14°. Because of the coarse spatial resolution of the numerical wave model, it cannot describe the coastal processes in detail.

The WaMoS marine radar located in the Bay of Terceira has a similar scanning coverage as TSX subscene A. The TSX simultaneous measurement of the WaMoS marine radar was acquired at 19:30 UTC. The two-dimensional spectrum retrieved from the intensity backscatter of WaMoS is represented in Fig. 8.6 (left). This spectrum is rotated to show the same coordinate direction with the TSX image heading direction, i.e. 348.6° clockwise relative to North. Peak wave direction and wavelength estimated by the marine radar are 50° (clockwise relative to the TSX azimuth direction) and 117 m, respectively. Both parameters derived from the nearest TSX subscene image spectrum A are 36° and 128 m, respectively. The slight difference may be caused by the larger scanning region of the marine radar than the coverage of subscene A over the inhomogeneous sea surface near the coast.

By comparing the results of numerical wave model and marine radar, it can be observed that the peak wave direction has a rotation of approximately 70° from the TSX image spectra of subscenes D, C, B and A along the shoreward direction, as summarized in Tab. 8.2, for the peak **P1**.

Table 8. 2 Peak Wave direction and length of P1 derived from TSX image spectra of subscenes A, B, C and D shown in Fig. 8.5 and Fig. 8.6

No. of subscene of TSX image	Peak wavelength (m)	Peak wave direction (clockwise relative to azimuth direction)
A	128	36°
B	155	14°
C	155	-14°
D	181	-34°

Examining the water depth estimation given by the ETOPO 1 model shown in Fig. 8.5, from D to A, bathymetry changes significantly, particularly from deeper than 200 m to shallower than 30 m. When the swell propagates toward Terceira island, because of the change of underwater topography, wave refraction occurs in the nearshore region. As the approaching swell has an angle with the bottom topography contours, wave crests bend parallel to the coast as observed by the rotation of peaks in the TSX image spectra from D to A. Furthermore, wave refraction also leads to the bending of crest parallel to the eastern coast of Terceira island. It can be observed in the second column of Fig. 8.6 how the peak rotates from -14° of C to nearly 0° traveling in the azimuth direction.

Using TSX data, the spatial variability of near-shore wave behavior is resolved well. On the other hand, the spectral information can be used to deduce situation on underwater topography. It should be noted that a limitation of using SAR intensity image spectra is 180 º ambiguity for ocean wave propagation direction. If complex data are available, this can be resolved using a cross-spectral approach.

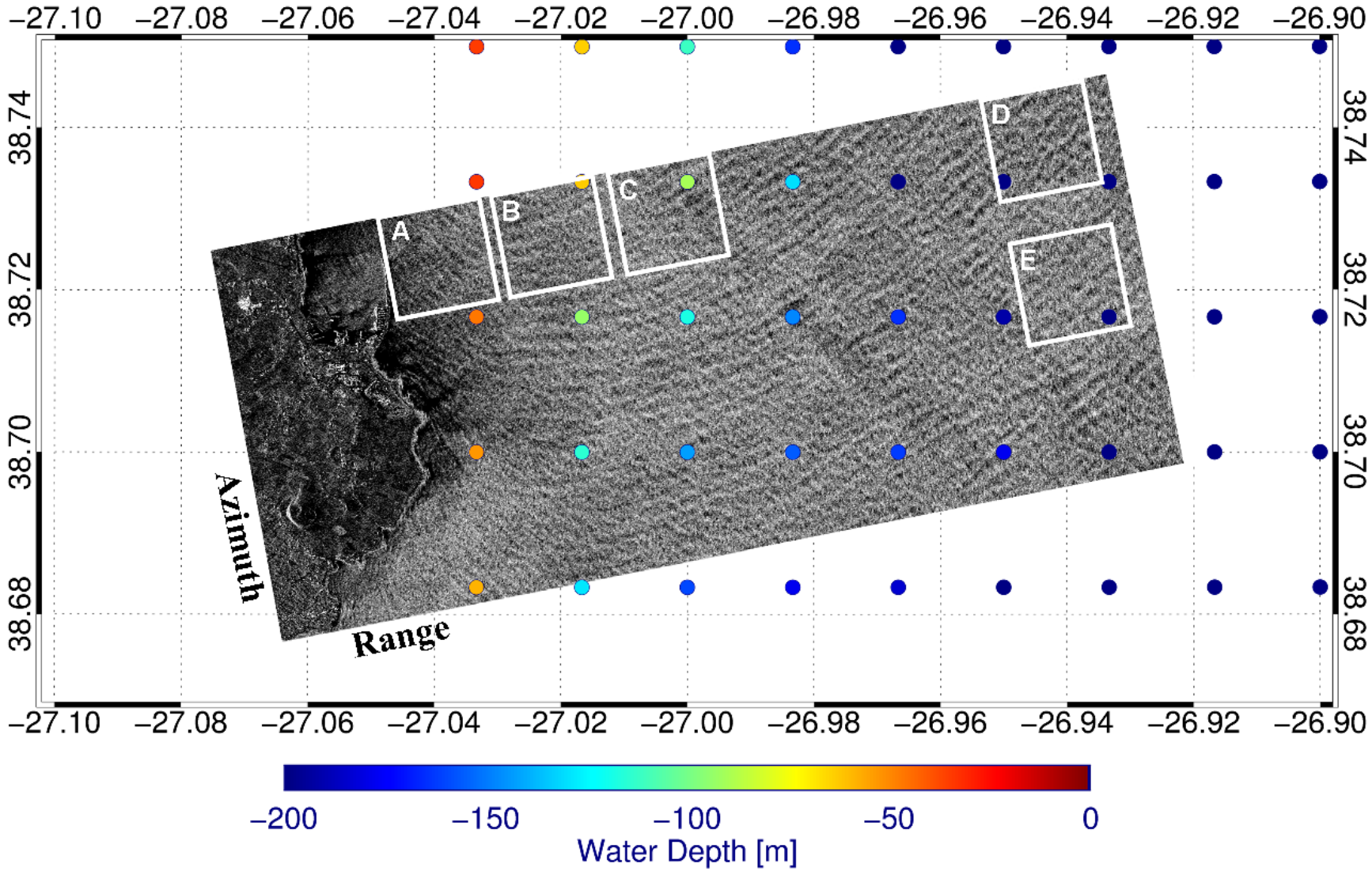

Figure 8. 4 TerraSAR-X Spotlight image acquired over Terceira island on March 26, 2008, at 19:32 UTC. Five subscenes marked as A, B, C, D and E are used for spectral analysis. Bottom topography given by the ETOPO 1 model is superimposed on the TSX image in grid points.

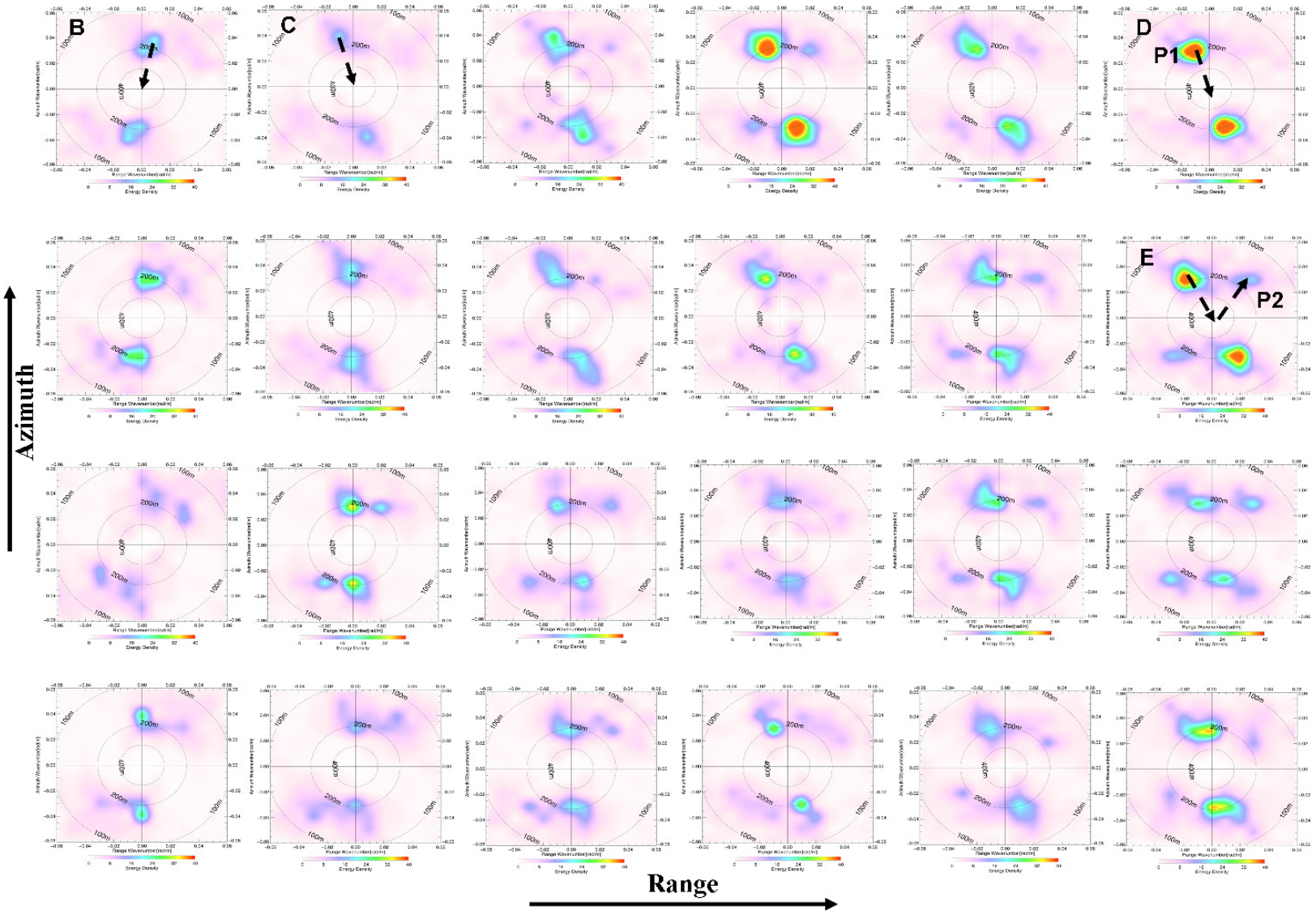

Figure 8. 5 Image spectra for the subscenes of TSX image divided by four rows and 6 columns between B and D. Each spectrum corresponds to a subscene of 1 km by 1 km.

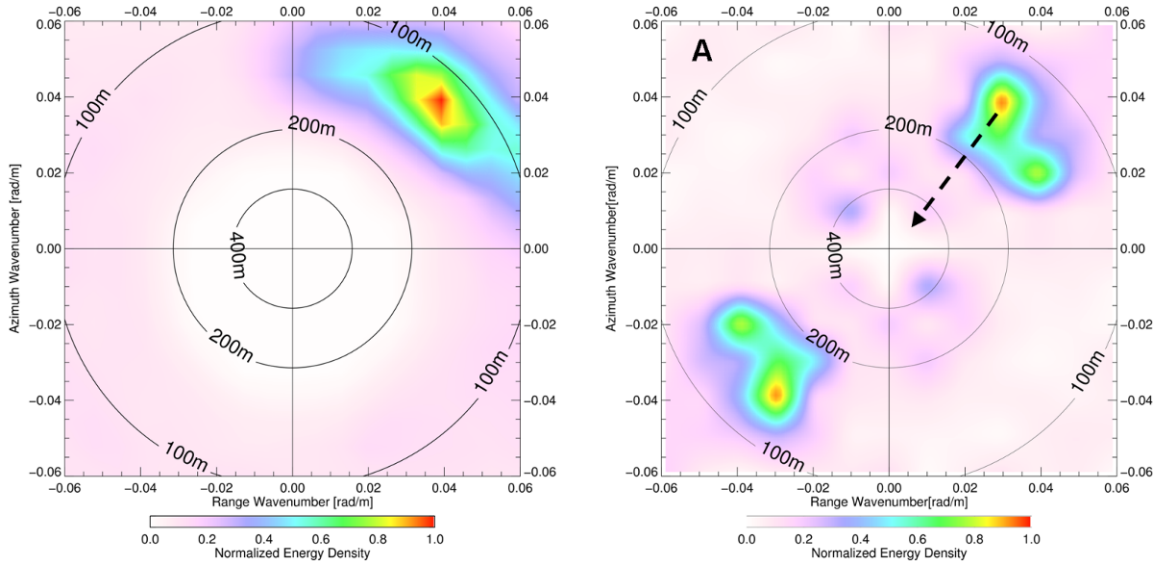

Figure 8. 6 TSX image spectra corresponding to the subscene A shown in Figure 8.4 with normalized energy density scale (right) and the spectrum estimated by the marine radar (left) with normalized energy density

As introduced in part A of this section, when wave refraction occurs, besides the change of wavelength and wave direction, the transformation of wave height occurs as well. Here we first estimate wave height from the TSX image based on wave refraction law.

The DWD GSM model gives, in deep water, a SWH H_d of 2.1 m, peak wavelength λ_d of 176 m, and angle between wave propagation and bottom topography contour α_d of 54° (assuming the water depth contour is parallel to the north-south direction) are used as the reference measurements in deep water. Parameters determined from the TSX image spectra used for estimating SWH for subscenes of A, B, and C are listed in Tab. 8.3.

Following Equ. (2.21) given in Chapter 2, the shoaling effect caused by water depth is estimated for the site of subscene A. Water depth h for site A is 33 m. Then the shoaling coefficient D_A (subscript used to denote subscene A) is calculated to be 0.928, and via Equ. (2.22), the refraction coefficient K_A is estimated to be 0.805. Thus one can estimate the SWH in the TSX subscene A to be 1.6 m through Equ.(2.20). Implementing the same method for subscene B and C, the SWH estimated

from the TSX image is given in the first column Tab. 8.4. For the calculations, H_d, λ_d and α_d are derived from the DWD model results of 2.1 m, 176 m, and 54°.

Table 8. 3 Parameters determined from the TSX image spectra used for estimating SWH for subscenes of A, B and C

No. of subscene in TSX image	Angle between wave and bottom topography α	Peak wavelength λ (m)	Water depth h (m)
A	25°	128	33
B	3°	155	62
C	25°	155	90

Table 8. 4 SWH estimated from TSX data in subscene of A, B and C using wave refraction laws and empirical algorithm

No. of subscene in TSX image	SWH (m) by refraction law using DWD model results as the measurements in deep water	SWH (m) by refraction law using XWAVE results as the measurements in deep water	SWH (m) by XWAVE empirical algorithm
A	1.6	1.7	1.9
B	1.7	1.9	2.2
C	1.8	2.0	2.3

An empirical algorithm XWAVE was developed to estimate integral wave parameter, SWH, from TSX data. Expression of the geophysical model function of the XWAVE algorithm is given in equation

$$SWH = a * 4.0 * \sqrt{E * (1.0 + \cos(\alpha))} + b \tag{8.1}$$

In the equation, E is total energy calculated from the TSX image wave number spectrum $\mathbf{F}(\vec{k})$ via

$$E = \int \mathbf{F}(\vec{k}) d\vec{k} \tag{8.2}$$

α represents the angle between peak wave direction (with 180° ambiguity) and SAR azimuth direction and also is determined from the image spectra. Two coefficients a and b are tuned by using hindcast results of the DWD wave model. *In situ* buoy

measurements will be used as the ground truth for further tuning.

In this case, SWH estimated by XWAVE for subscene D is 2.4 m, which is slightly higher than the DWD GSM model result of 2.1 m. Choosing the result for SWH from D estimated by using the XWAVE algorithm as the initial value for deep water, the SWH for subscenes of A, B and C are determined by using the wave refraction law. Results are given in the second column of Tab. 4. The SWH measured by the WaMoS marine radar is 1.2 m, which is lower than other estimations from the model and TSX data.

SWH for the three subscenes calculated directly by using XWAVE algorithm are given as well in the third column in Tab. 8.4. It shows a slightly higher estimation than using the refraction law. Further tuning for the coefficients in Equ. (8.1) is under investigation including cases of low sea state.

In this case study, the GSM wave model provides regional view of the incoming swell system and the TSX data as well as its image spectra show good agreement of the swell system in the offshore region when compared to the model. Interaction of surface gravity waves and bottom topography are depicted by the TSX image, which cannot be resolved in the model because of limitation of spatial resolution. The WaMoS provides simultaneous measurement for a small scanning area near the coast. This is particularly suitable for harbor monitoring. The TSX data are an effective tool to derive the spatial variations of wave behavior and processes (e.g. refraction, shoaling and breaking) in the near-shore region.

In the SAR spectrum of E shown in Fig. 8.5, another peak denoted by **P2** can be observed, at an angle of around 45° to peak **P1** and thus generates a cross sea [*Li, et al.*, 2009]. Because of the limited spatial coverage of the TSX Spotlight image used, we cannot tell where the second wave component is from. Therefore, in addition, a large coverage StripMap image is used to examine the generation of cross sea. In the following, the StripMap data acquired on January 15, 2009, as marked by the yellow rectangle in Fig. 1 is used for the analysis.

Sea state situation derived from the DWD GSM model on January 15, 2009, at 9:00 UTC is chosen as the synergetic observation together with the StripMap mode image. The wind field of the GSM model is shown in Fig. 8.7 (a). The nearest model grid point to the TSX image is located in 39°N, 27°W, where the wind speed is 6.0 m/s from northeast. SWH together with peak wave direction for windsea and swell is

shown in Fig. 8.7 (b). At 39°N/27°W, the swell and windsea wave height is 5.2 m and 0.1 m respectively, and the swell peak wavelength is 285 m in the direction toward southeast. Therefore the sea state around the Azores is thus dominated by strong swell during the acquisition time of the TSX StripMap image.

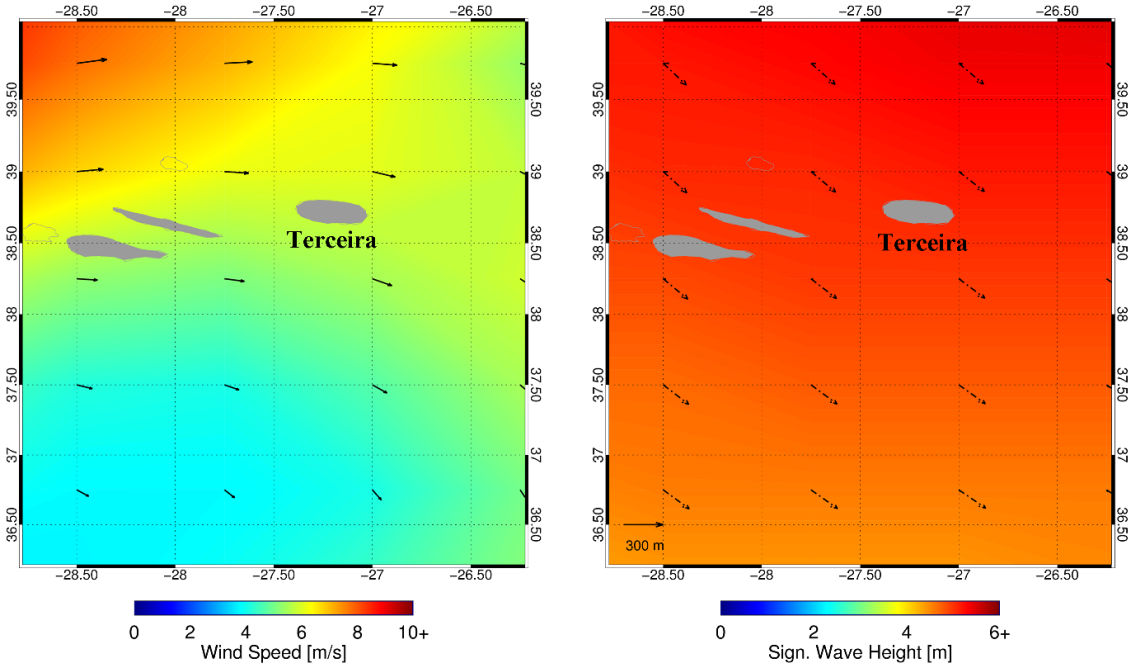

(a) (b)

Figure 8. 7 (a) Wind field and (b) SWH (background) with peak wave direction of swell and windsea derived from the DWD GSM wave model around Terceira island on January 15, 2009 at 9:00 UTC.

Fig. 8.8 shows the TSX StripMap image acquired over the eastern Terceira island on January 15, 2009 at 7:55 UTC. Ground coverage of the StripMap image is 30 km in range and 60 km in azimuth with a spatial resolution of 3.0 m in both directions. Like the Spotlight image shown in Fig. 5, the bottom topography derived from the ETOPO1 model is superimposed as well on the StripMap TSX image. Only grid point measurements of water depth shallower than 150 m are superimposed on the TSX image. One can observe that in the offshore region approximately 18 km south of Terceira island, water depth is deeper than 150 m, which is different from the northern coast. In the northern coastal region of the island, as previously analyzed, long swell crests bend parallel to the coast line caused by refraction. While in the southern coast,

the crest wave direction does not change significantly which is mainly due to the steep gradient in the bottom topography resulting in less refraction of the long waves.

Six subscenes marked by white squares on the StripMap image are used for analyzing the spatial variability of the surface waves induced by interactions with the bottom. The corresponding image spectra of the subscenes are shown in Fig. 8.9. Subscenes A and B are chosen in the North and South around 30 km away from the island in deep water (water depth deeper than 200 m). These areas are used to determine the sea state of the wave trains approaching the island.

In the image spectra of A and B, one can observe that swell with peak wavelength of around 300 m propagate toward the island, as comparable to the results of the DWD GSM wave model. Narrower energy peaks are found in the image spectra of B than in A. This indicates that less directional spreading of waves exists near the southern coast.

A sheltered region located at the southeastern edge of the island is quite distinct in the TSX image. When long waves are intercepted by a barrier such as the Terceira island in the present case, a shadow zone will appear in the lee side of the island. Subscenes of C, D and E are chosen in the shadow zone and F is out of the region. As shown in the spectrum of Fig. 8.9, swell component propagating along the southern coast almost disappears in image spectra of C. The spectral density value for this swell component increases gradually further away from the coast, as observed in image spectra of D and E, as well as the backscatter intensity in the TSX image subscenes.

The generation of shadow zone and penetration of wave energy into the region to the lee of the island are determined by wave refraction, diffraction, and variability in direction of wave travel. The influence of these factors is investigated separately in [*Arthur*, 1951], although they are not independent. In the present case, the water depth in the region between B and C changes significantly from less than 10 m to deeper than 200 m, whereas the peak wavelength in the region B is approximately 300 m. This may lead to less wave refracting in the C region. Therefore, the sheltered region in the lee side of Terceira is influenced jointly by the wave diffraction and refraction.

Furthermore with respect to D, in addition to the wave component that propagates along the southern coast of the island, the spectra also indicate another wave component. This wave component propagates in the direction of south-north parallel

to the Terceira eastern coast, where the water depth is shallower than 100 m. Therefore the second wave component observed in D is the refracted wave propagating from the north of the island.

In the SAR image spectrum and subscene of F, the cross sea feature becomes distinct. Nevertheless, generation of this cross sea is different from the one observed in D. In addition to the same wave component coming from the south of Terceira island, the other one is the diffracted wave from the north. Both wave refraction and diffraction can cause a change in wave traveling direction. The former tends to be parallel to the coasts in the shallow water, whereas the wave direction is bent surrounding to the obstacle in diffraction.

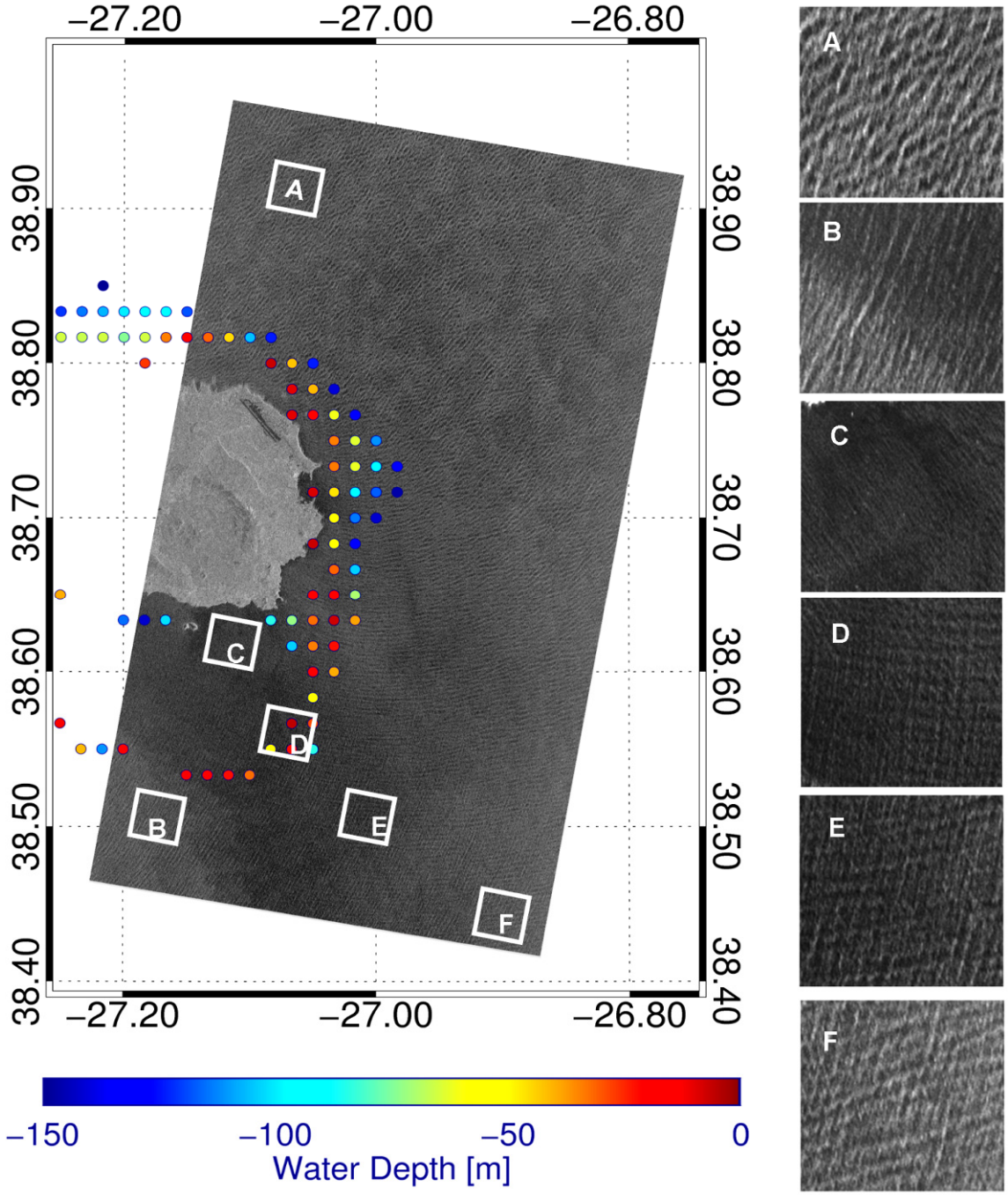

Figure 8. 8 TerraSAR-X StripMap mode image (around 30 km by 60 km) acquired over Terceira island on January 15, 2009 at 7:55 UTC. Six subscenes marked as A, B, C, D, E and F are used for spectral analysis. Bottom topography derived from the ETOPO 1 model is superimposed on the TSX image in grid points. The right panel shows the enlarged subscenes.

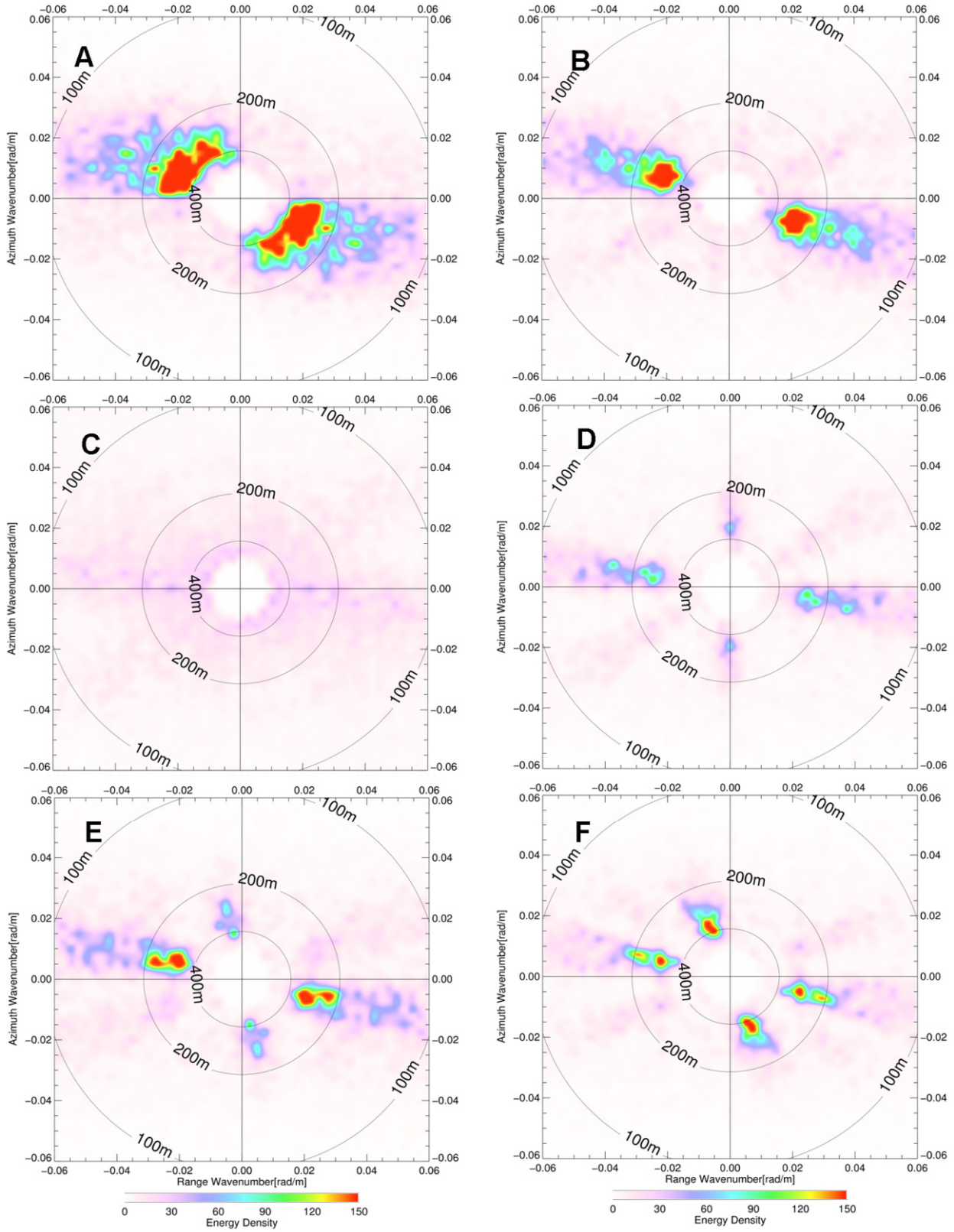

Figure 8. 9 SAR Image spectra derived from the subscenes of A, B, C, D, E and F as represented by the white squares in the Fig. 8.8. Spectral intensity value is scaled in respect to spectrum A

8.4. Conclusions

In this study, we demonstrate the capability of different TSX modes to image surface gravity waves. Compared to conventional ERS SAR and ENVISAT ASAR, TSX has a lower R/V value, which provides the possibility to analyze ocean wave information directly using TSX image spectra.

To demonstrate the capabilities of TSX imaging of surface gravity waves in detail, a case study of wave refraction-diffraction occurring around Terceira island is analyzed. It is performed by using TSX Spotlight and Stripmap mode image together with other auxiliary data, i.e., numerical wave model, simultaneous measurement of X-band marine radar and ETOPO 1 topography data.

In the northern coast of Terceira island, wave refraction is caused by the rapid change of bottom topography that bends the crests of incoming long swell parallel to the coastal line. Simultaneous measurement of marine radar WaMoS in Praia da Vitória Bay shows the near-coast peak wave directions different from the numerical wave model of DWD. By analyzing the two-dimensional SAR image spectra derived from the Spotlight image, how the incoming long swell wave crests bent parallel to the coast can be observed. Along the direction toward the shore, four TSX subscenes image spectra are compared showing that the peak wave direction is rotated from 36° clockwise relative to the azimuth direction of -33° while the wavelength decreases from 181 m to 128 m during the wave refraction process.

In the present case, variability of SWH during the refraction process is investigated through two different methods. Following the wave refraction laws, when the results of the DWD GSM model as the initial value for deep water were taken, SWH is estimated to be 1.6 m near the coast, which is around 0.4 m higher than the measurement of WaMoS marine radar. Empirical algorithm XWAVE is developed to derive SWH directly from TSX data. Retrieved SWH in the present case for near coast is 1.9 m, which is rather higher than the measurement from WaMoS. While when taking the XWAVE result in deep water as initial value and following the wave refraction law, the estimated SWH in near coast is 1.7 m. The comparison results indicate that the retrieved results by using XWAVE algorithm is reasonable while needing further improvement including the different sea state.

When considering the role of the entire Terceira island in the ocean wave variability, it can cause e wave diffraction occur when long swell approaches. The

phenomenon is analyzed by using a TSX StripMap mode scene with coverage of 30 km by 60 km. Image spectra derived from the StripMap show the wave behavior before and after diffraction. Two subscenes of 3 km by 3 km in the TSX StripMap image located in the north and south of the Terceira island show that long swell with peak wavelength about 300 m approaches the island. The shadow zone is identified in the lee side of the Terceira island. This sheltering effect is found to be influenced by wave refraction and diffraction jointly. A cross sea feature observed behind the island is generated by refracted and diffracted waves, whereas in the seaward, it has strongly been affected by the diffracted waves surrounding the island.

As Terceira island is located at high latitude in the North Atlantic, ocean swell constantly arrives from distant storms or cyclones. Therefore, the TSX images can capture wave refraction-diffraction in this situation.

The TSX images with high resolution and suitable coverage size will be particularly used as a good tool to observe spatial variability of coastal ocean wave behavior. This will contribute to coastal engineering, infrastructure protecting and local numerical wave model development.

Chapter 9

Global Sea State Analysis Using ASAR Wave Mode Data

Validation and comparison of CWAVE_ENV algorithm to other dataset are presented in detail in chapter 7. By comparison to *in situ* buoy measurements, numerical wave model results and cross over measurements of the radar altimeters, it is proven that the estimation of integral wave parameters derived from ASAR wave mode data using the CWAVE_ENV algorithm is reliable and independent. Therefore, this makes SAR an additional radar observation contributing to the global statistical analysis of surface waves.

In this chapter, ocean wave integral parameters of SWH and T_{m02} retrieved by the CWAVE_ENV algorithm for one full year ASAR wave mode data acquired between June 2006 and May 2007 are used for such a global statistical analysis of sea state.

9.1. Distribution of retrieved SWH by CWAVE_ENV

The long-term variability of SWH is an important descriptor for wave climate. Different approaches have been proposed to describe the variability, with emphasis on the prediction of extreme waves, i.e. the return of extreme values for the long term. The general idea is to fit different probability density functions (PDF) using all the collected SWH measurements and then to derive the return value from the fitted model. Various PDF models have been adopted for fitting long-term SWH distributions, e.g., Weibull distribution for fitting the long-term shipborne wave recorders in the North Sea and Irish Sea [*Battjes*, 1972], as well as for the *in situ* buoy measurements acquired along the Portuguese Coast [*Guedes Soares and Henriques*, 1996]; lognormal distribution [*Jaspers*, 1956]; Gamma [*Ochi*, 1992] or Beta distributions [*Ferreia and Guedes Soares*, 1999]; or the combination of different distributions [*Haver*, 1985]. Apart from the standard statistical distribution models, the so called Peak-Over-Threshold (POT) method, e.g., in *Coles* [2001]; *Ferreira and Guedes Soares* [1998] and *Caires and Sterl* [2005], is also used to estimate the return wave heights.

One has to notice that the estimation of return value strongly depends on the tail of the probability distributions, which vary for different PDF models. The choice of a PDF model, on the one hand, depends on the data set, e.g., derived from *in situ* measurements, numerical wave model or satellite remote sensing. On the other hand, there is no PDF model that can describe the entire data set accurately, which can only be determined by the accuracy of the fitting.

In this section, a one-year SWH data set derived from the ASAR wave mode data is fitted to different PDF models and the return value for extreme SWH is given. Although, it is not sufficient to such an investigation based on one-year data only, it demonstrates the possibility of using long time series SAR wave mode data for global sea state analysis.

The histogram of retrieved SWH by using CWAVE_ENV algorithm for one-year (2006 June to 2007 May) is shown in Fig. 9.1. There are more than 500,000 measurements available in the dataset. Dominant SWH is distributed between 2.0 m and 2.5 m. The maximum retrieved SWH in the data set is 16.7 m. Four types of PDF models, i.e. normal distribution, Weibull distribution, extreme distribution and lognormal distribution, are fitted to the retrieved SWH. One can observe that generally the extreme and lognormal distributions fit the entire data set well, except the underestimation of the peak.

The Weibull distribution has been widely used for probability distributions of wave height and wind speed. It seems though that the Weibull distribution does not fit well the present dataset. The tail of the fitted different PDF models is shown in Fig. 9.2. For SWH above 5.0 m, the behavior of the tail of the models is quite different. The Weibull distribution can provide a better tail for SWH between 5.0 m and 5.5 m. While for SWH higher than 5.5 m, it decreases sharply and strongly underestimates.

The lognormal distribution also estimates high sea state well, while in the extreme sea states it gives a better fit than all other models. Therefore, the lognormal distribution model is used for estimating return periods of extreme SWH based on the one-year dataset. The model function for the lognormal distribution is given by Equ. (9.1)

$$p(x) = \frac{1}{x\sigma\sqrt{2\pi}} \mathbf{exp}\left(-\frac{(\mathbf{ln}\, x - \mu)^2}{2\sigma^2} \right) \tag{9.1}$$

where μ and σ are the mean and standard deviation of the variable's natural logarithm (μ (mean) = 0.909 and σ (variance) = 0.404). The 10-year return value thus estimated to be 23.4 m.

In the present study, the PDF is used for fitting a global dataset, whereas further studies should use distributions of SWH in different oceanic basins and fit PDFs to them.

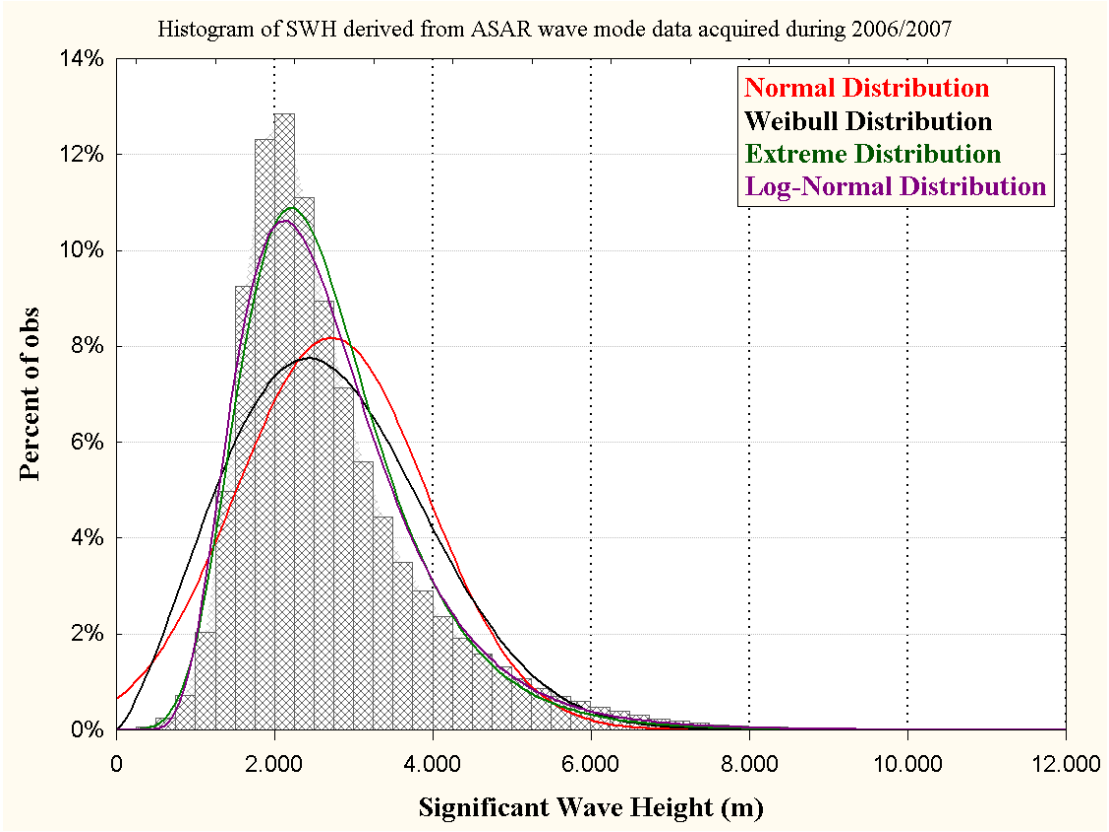

Figure 9. 1 Histogram of retrieved SWH superimposed with fitted PDF models

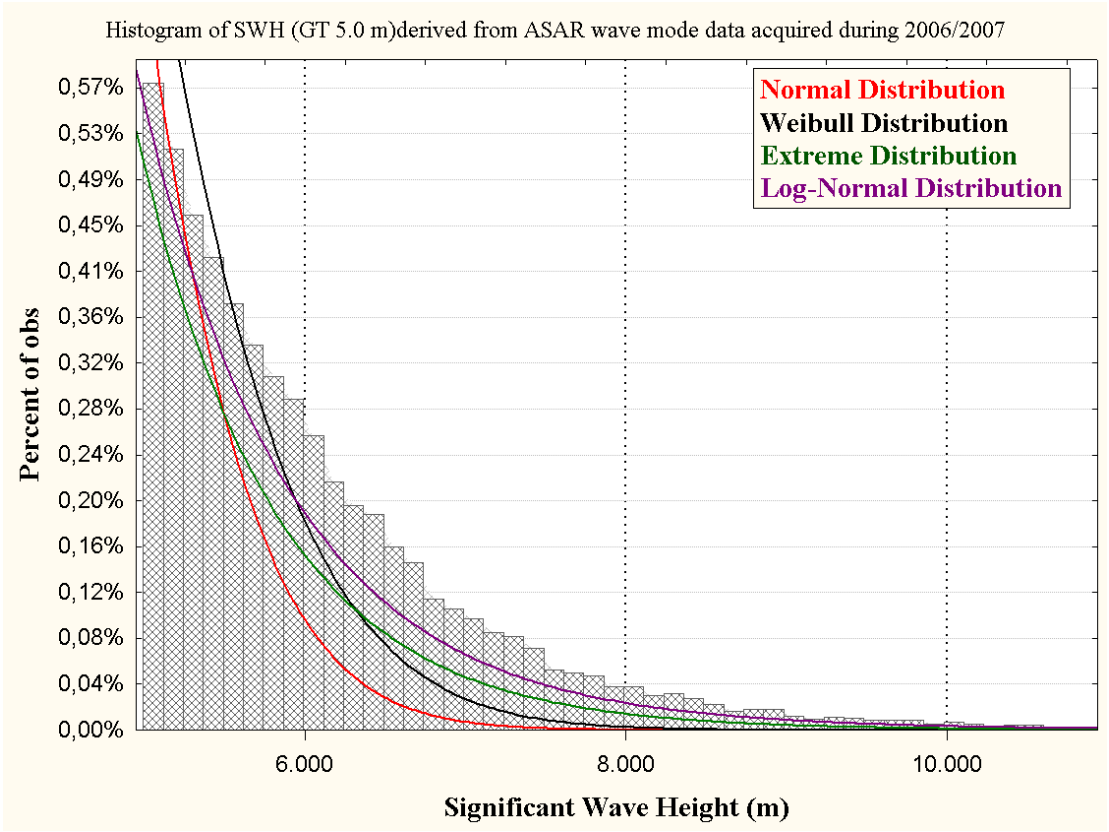

Figure 9. 2 Histogram of retrieved SWH (above 5 m) with superimposed fitted PDF models

Joint Distribution of SWH and T_{m02}

Fig.9.3 shows SWH as a function of mean wave period, derived from the one-year ASAR wave mode data. Three lines indicating different wave steepness are superimposed on the diagram. Wave steepness is one of the key parameters describing sea state. It is defined as ratio of SWH to wavelength, which is related to wave period via dispersion relationship. Therefore, the wave steepness can be expressed by Equ. (9.2)

$$S = \frac{2\pi H_s}{gT_{m02}^2} \tag{9.2}$$

One can observe there are some cases with S higher than 0.06, which might indicate some dangerous sea state. The compiled global wave steepness map is given in next section.

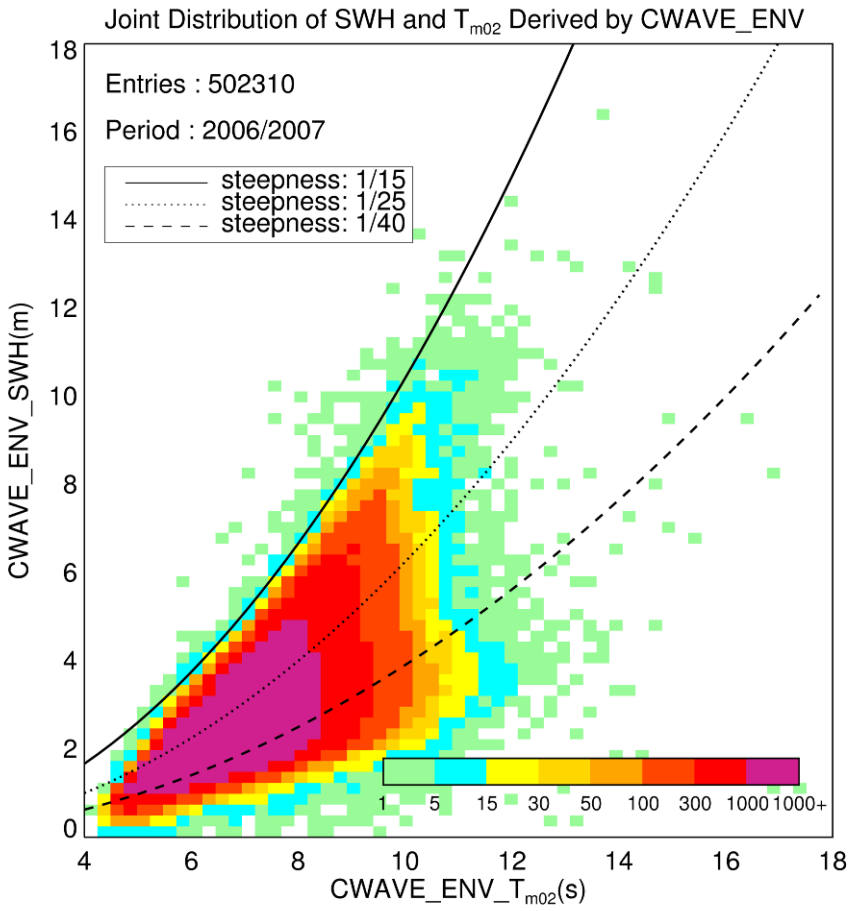

Figure 9. 3 SWH as a function of T_{m02} derived from one-year ASAR wave mode data using the CWAVE_ENV algorithm. Colours indicate the number of cases found. Bin size is chosen as 0.25 (m and s) for statistics.

9.2. Wave maps compiled by ASAR

Seasonal Analysis

SWH and T_{m02} in all four seasons during 2006/2007 are compiled into maps in Fig. 9.4 and Fig. 9.5, respectively. These maps are compiled with resolution of 1.5 by 1.5 degrees.

In the North Pacific and the North Atlantic, the highest global sea states are found in the winter season. Particularly between 40º-60ºN and 0º-50ºW winter storms often lead to SWH higher than 6 m. In the North Atlantic, high waves with average SWH above 5 m almost cover the entire basin, while the mean wave period builds up continuously towards the east. This shows that the North Atlantic is a fetch limited basin with steeper waves towards the west. Storm systems of high forward speed generate high waves, which are not fully developed in the western basin.

In the Southern Hemisphere, high sea state is found in the region between 40°S~60° in all seasons and particularly high in the season JJA, with mean SWH > 6.0 m. Extreme swells in the Southwest of Australia with mean wavelengths > 200 m are also observed in the winter season of the Southern Hemisphere. These long swells are generated by Antarctic storms and propagate across the Indian Ocean and the Pacific. These waves, together with high SWH, can cause coastal hazards, e.g., the extreme swell in 2007 May at the La Reunion coast [*Lefèvre and Aouf*, 2008; *Li et al.*, 2009].

In summer, the monsoon influence on sea state is observed in the western Indian Ocean with mean SWH around 4.0 m and above 4.5 m along the west coast of India. Furthermore, one can observe that SWH increases gradually from west to east.

Comparing the SWH and T_{m02} maps in different seasons, one can observe that high SWH coverage is smaller than the one of high mean wave period. Long swells exist approximately from 20°N to 60° N while high SWH exceeding 6 m only covers the 40ºN- 60ºN belt. In the Southern Hemisphere, the phenomenon is even more obvious in its winter season. Windsea with high SWH are generated by storms or cyclones and swell can propagate long distance without the influence of strong wind field. This phenomenon observed in the maps indicates that the SAR sensors are particularly powerful for investigation of swell propagation, e.g. the dissipation.

It has to be pointed out that the effect of coarse sampling of the ASAR instrument. One can observe the “washboard” patterns in these maps which are caused by the coarse sampling rate. Although the main sea state signals are represented in these maps, probably some details are still missed. When dealing with the global sea state analysis using the satellite remote sensing, the sampling rate has to be considered.

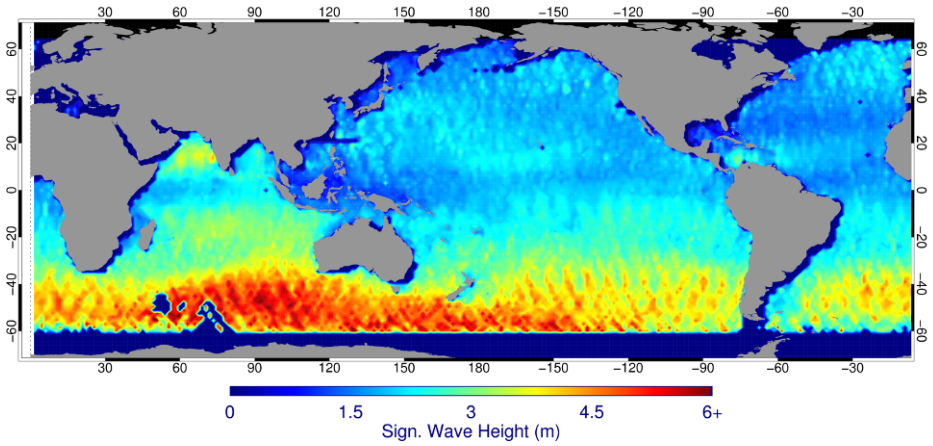

2006 JJA

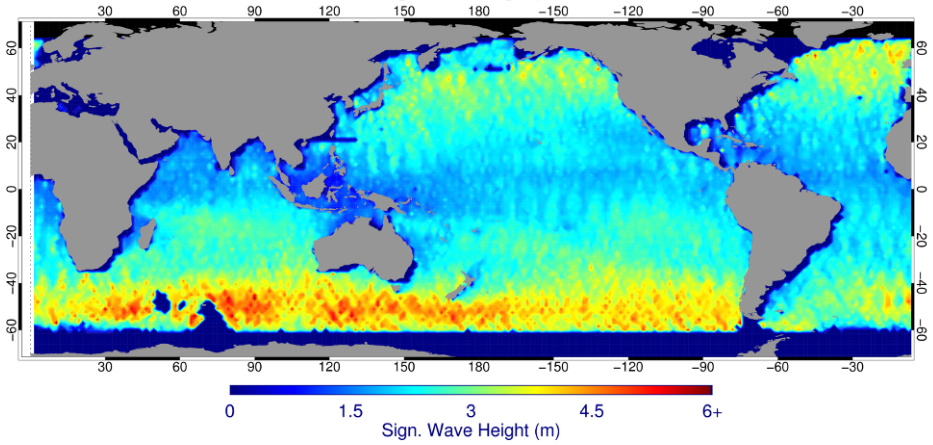

2006 SON

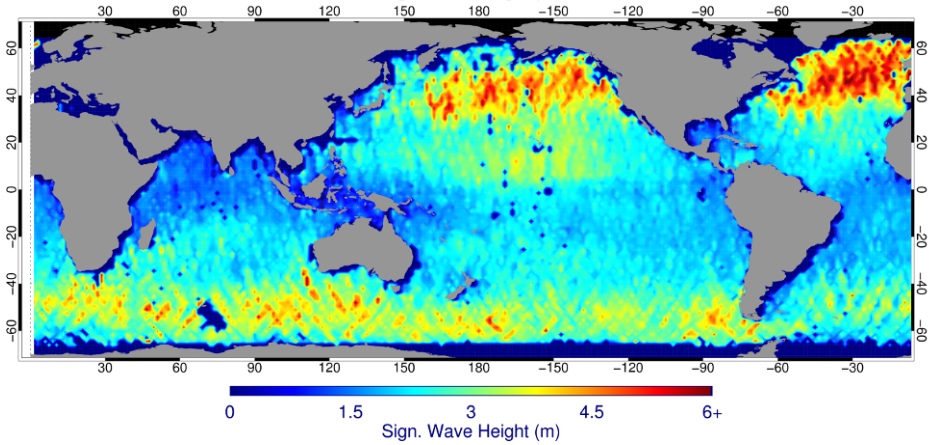

2006/2007 DJF

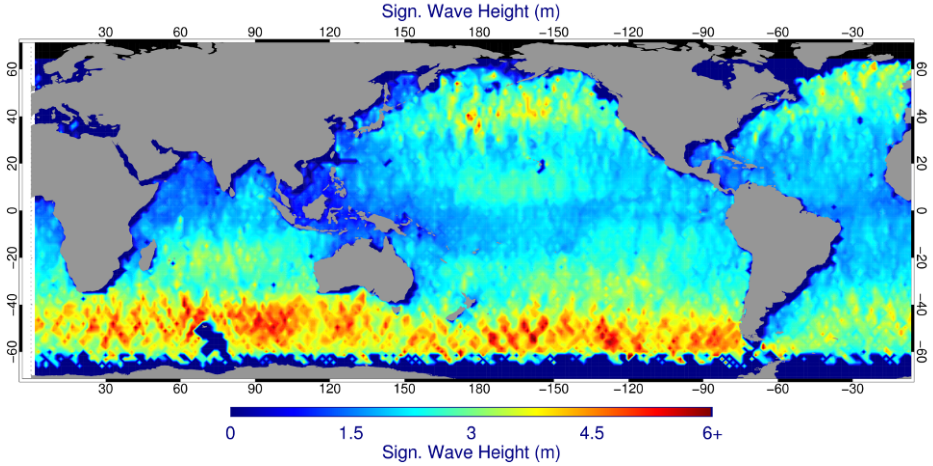

2007 MAM

Figure 9. 4 SWH maps from summer 2006 to spring 2007 for all seasons derived from the ASAR wave mode data with the CWAVE_ENV algorithm

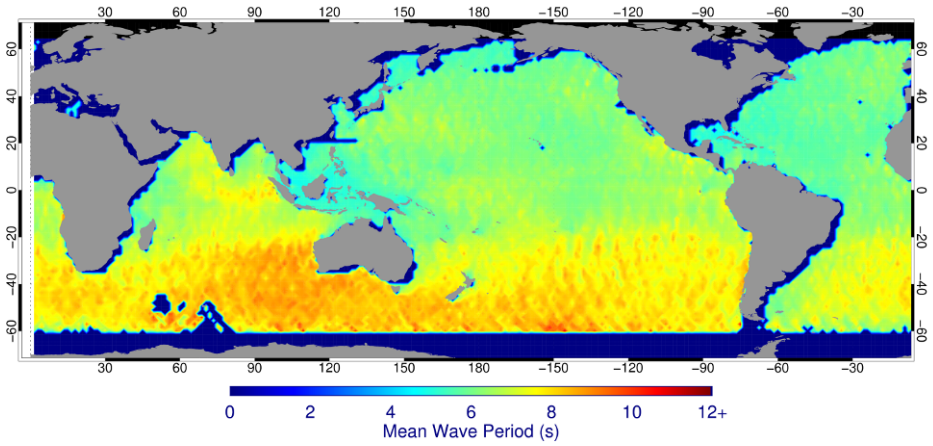

2006 JJA

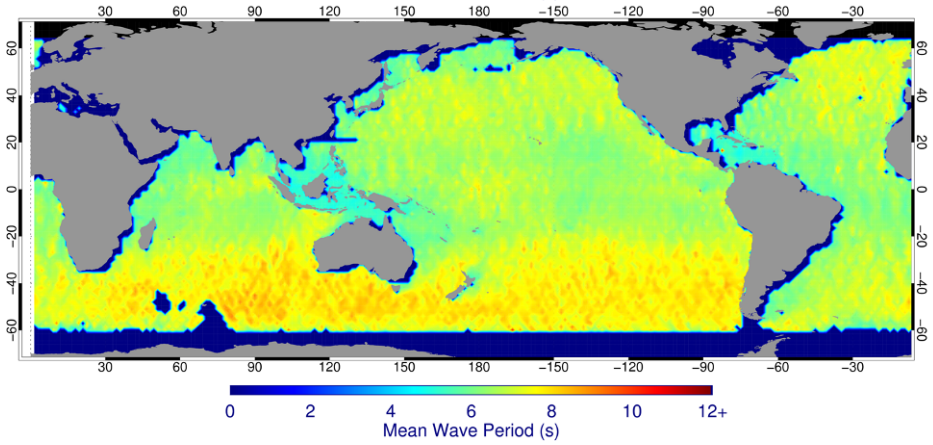

2006 SON

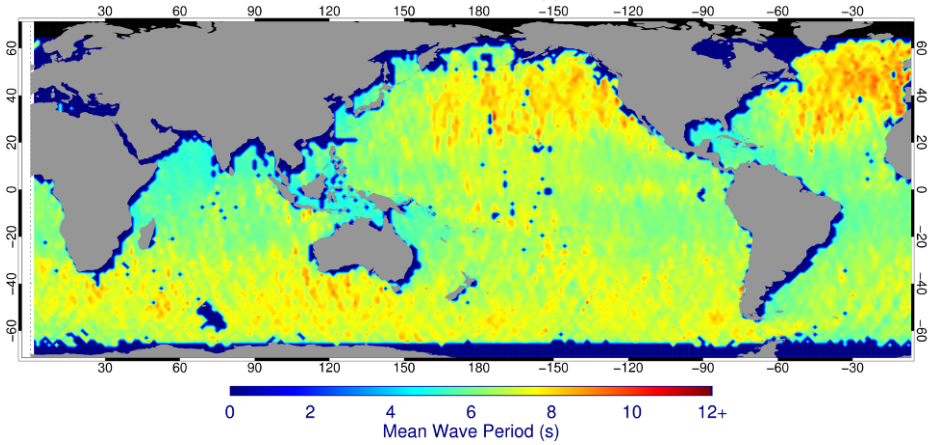

2006/2007 DJF

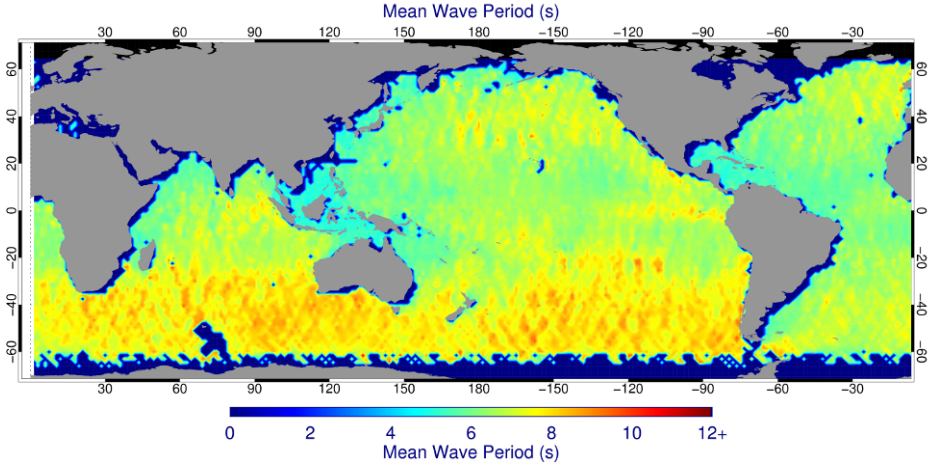

2007 MAM

Figure 9. 5 T_{m02} maps from summer 2006 to spring 2007 for all seasons derived from the ASAR wave mode data with the CWAVE_ENV algorithm

Annual Mean

The global maps of SWH and T_{m02} for the annual mean are presented in the Fig. 9.6 and Fig. 9.7, respectively. In addition, the wave maps from the ERA-40 data during 1971-2000 (http://www.knmi.nl/onderzk/oceano/waves/era40/license.cgi) are shown for comparison of the main patterns.

Generally, one can observe that the annual mean SWH derived from ASAR is very similar to the corrected ERA-40 (C-ERA, see Appendix 2 in Chapter 11) wave model data, while the ASAR results are affected by the sampling.

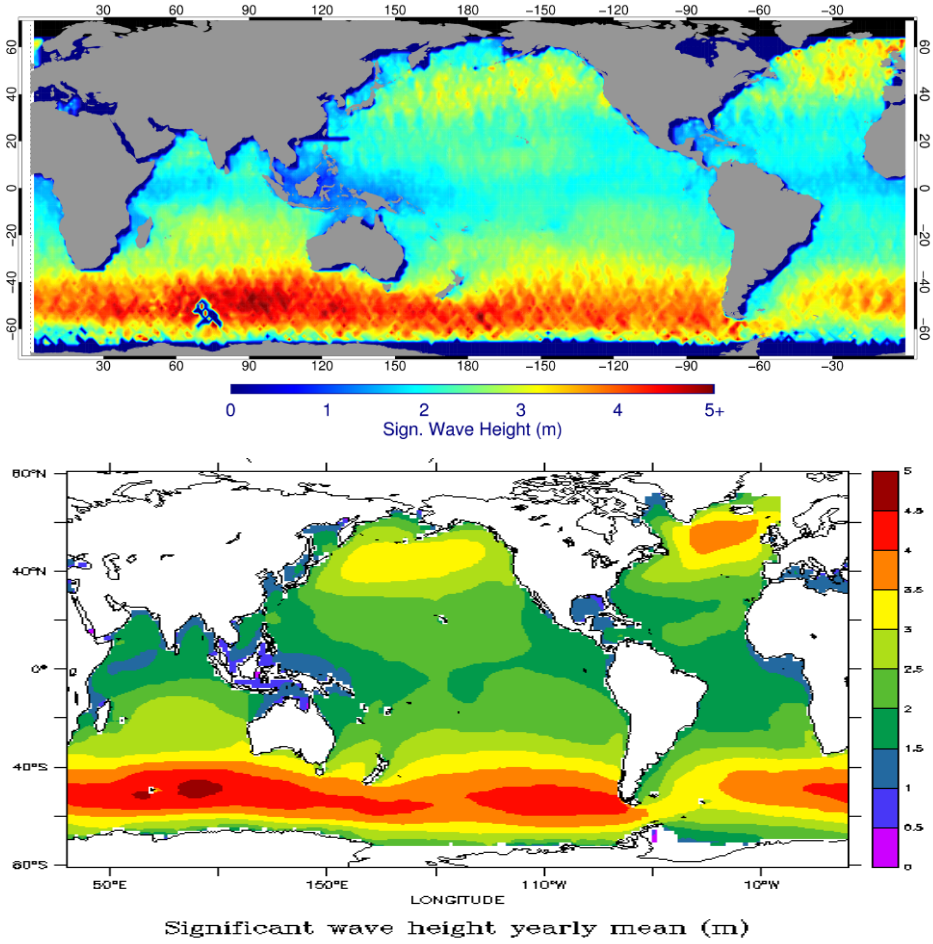

ASAR
2006 June
~2007 May

C-ERA40
1971~2000
©KNMI

Figure 9. 6 Annual mean SWH map from June 2006 to May 2007 derived from the ASAR wave mode data with the CWAVE_ENV algorithm; (upper panel); SWH map derived from the ERA-40 wave model data during 1971~2000 (lower panel)

Both plots of SWH show the region of 40°S - 60°S as the one with strongest wave systems, i.e. mean SWH > 4 m, and even in some regions over 4.5 m. In the North Atlantic, probably because of some ASAR wave mode data globally acquired in HH polarization (during 24/01/2007 ~ 30/01/2007) and/or with incidence angle of 33° (during 24/01/2007 ~ 06/02/2007 and 06/03/2007 ~ 13/03/2007) are excluded from the dataset, a slightly lower estimation of around 0.5 m is observed. In the North Pacific, dataset give a mean SWH of 3.0 m – 3.5 m.

Besides the similar patterns, one still can find differences, the most obvious one in the western Indian Ocean. Mean SWH estimated by ASAR is over 2.0 m, whereas the C-ERA40 shows an underestimation by1.5 m – 2.0 m.

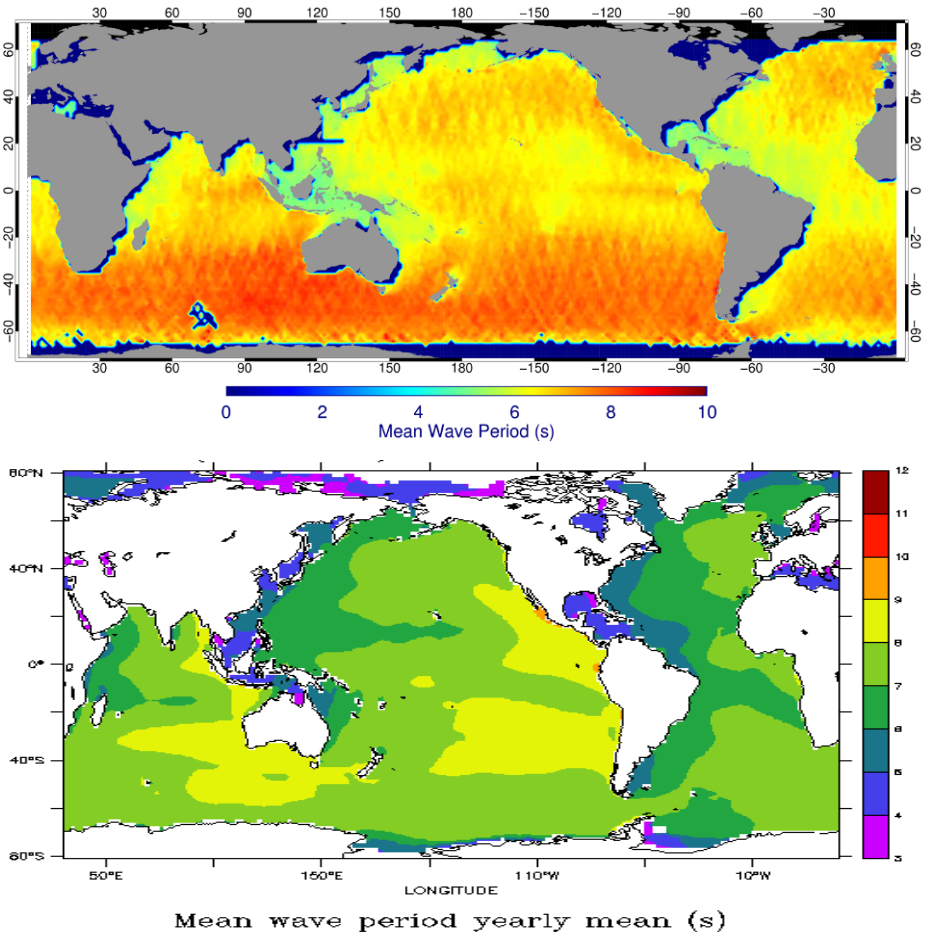

ASAR
2006 June
~2007 May

ERA40
1971~2000
©KNMI

Figure 9. 7 Annual mean wave period map from June 2006 to May 2007derived from the ASAR wave mode data as computed by using the CWAVE_ENV algorithm (upper panel);
Mean wave period map derived from the ERA-40 wave model data during 1971~2000 (lower panel)

With respect to the mean wave period, long swells with mean period over 10 s are observed in the ASAR maps, in the basin southwest of Australia, while the model underestimates it by around 1 s. This also indicates that the SAR sensors are particularly sensible for swell detection, which probably is an advantage compared to the radar altimeters.

In Fig. 9.8, the mean wave steepness based on the full year dataset is shown. Besides the basins with high waves and long swell as analyzed above, also other regions show high steepness. Most obvious is in the regions around Hawaii Islands in the North Pacific and the region between Madagascar and the west coast of Australia.

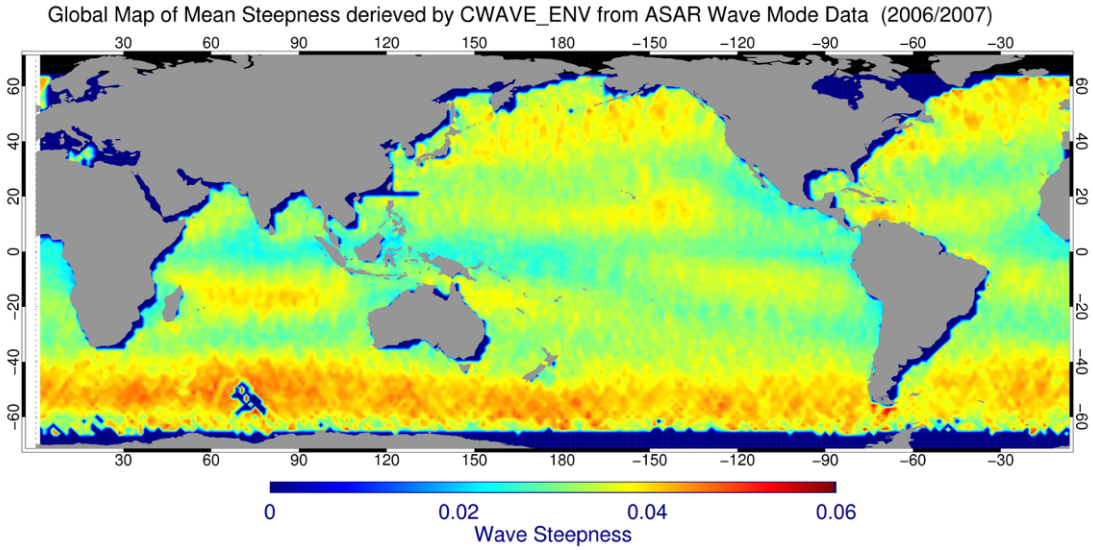

Figure 9. 8 Global map of wave steepness derived from one-year ASAR wave mode data acquired during 2006 June to 2007 May

9.3. Summary

In the present study, full year ASAR wave mode data is processed using the new CWAVE_ENV algorithm. Distribution of wave height derived from ASAR wave mode data is investigated. The lognormal PDF function is used for a first estimation of the returned period for extreme SWH.

Global wave maps are compiled using the retrieved integral wave parameters and seasonal variations for SWH and T_{m02} are discussed. The seasonal maps represent the variations of sea state during 2006 June~2007 May. The annual mean SWH and T_{m02} are also compared to the results derived from reanalyzed ERA-40 wave model data.

A global wave steepness map based on the one-year data is given as well, pointing to areas with high steepness outside the storm regions. This is a new result for studying the global wave steepness using the spaceborne radar sensor, which also indicates the advantages of using SAR wave mode data for sea state analysis; On the one hand, SAR is sensible for the swell detection and on the other hand the developed new empirical algorithm CWAVE_ENV can yield reliable integral wave parameters.

In principle, ERS SAR wave mode data are available since 1991 and ENVISAT ASAR since 2002. Inter-annual variability would be derived from this dataset using the CWAVE empirical algorithm for nearly two decades. With further missions, global wave climatology from space observations is in sight.

Chapter 10

Summary and Conclusions

This study focuses on the development and validation of SAR ocean wave retrieval algorithms, particularly those proposed for the ASAR wave mode data from the ENVISAT mission. A global sea state analysis using the results of CWAVE_EVN algorithm has been performed. Summaries for the different parts are given in the following sub-sections.

- **Validation of two-dimensional wave spectrum retrieval schemes using SAR complex data**

In the first part of the thesis, existing algorithms, i.e. PARSA and ESA WVW, for the retrieval of two-dimensional wave spectra from ASAR wave mode complex data are compared and validated. Both algorithms use the SAR cross spectrum as the input while the PARSA scheme needs also a priori information, e.g. from numerical wave model WAM.

The full wave spectra are retrieved using the PARSA scheme whereas the results derived from the ESA WVW products are limited to the wavelength longer than the cut-off of SAR data, usually around 200 m. Therefore the wave parameter SWH integrated from the WVW spectra has a significant bias of -0.19 m and a large scatter index of 36% when compared to *in situ* buoy measurements. Even when it is argued that the wave height retrieved by the WVW scheme is only the swell SWH, this still shows a scatter index of 50% for H_{12} wave height as compared to the reanalyzed ECMWF wave model. Furthermore, the underestimation of wave height increases with sea state.

On the other hand, the integrated wave parameter SWH derived from the PARSA spectra agrees well to the *in situ* buoy measurements with a bias of only 0.09 m and a scatter index of 21%. Compared to the forecast wave model of DWD, the bias of -0.01 m is negligible and the scatter index is as low as 16%.

- **Development and validation of the empirical algorithm CWAVE_ENV**

As the ESA WVW scheme does not include a priori information for the retrieval of

ocean wave spectra, the results are limited to frequencies lower than the cut-off and therefore cannot be used for measurements of the full SWH. Therefore the new empirical algorithm CWAVE_ENV has been developed to retrieve the integrated wave parameters, e.g. SWH and mean wave period, from ASAR wave mode data while not using a priori information. This makes the SAR to an altimeter like wave parameter measuring instrument.

Validation, particularly by comparison to the independent *in situ* buoy measurements and radar altimeters, proves that reliable and accurate sea state measurements can be achieved, with a bias of only 0.06 m and a scatter index of 24% for buoys in deep water, and a bias of -0.11 m and -0.13 m at a scatter index of 13% and 17% for crossover measurements by the radar altimeters onboard GFO and JASON, respectively.

The CWAVE_ENV algorithm also has limitations, for instance a rather high bias for very low sea state, with SWH < 1.0 m, when backscatter is close to the noise level of the instrument.

On ERS and ENVISAT satellites, the SAR and RA are onboard the same platform. Because of the independent and reliable measurements of sea state from ASAR wave mode data using the CWAVE_ENV algorithm, both sensors can be used jointly with a spatial distance of around 300 km. This is useful as the SAR can yield additional validation for the numerical wave model, particularly for sea state observation in storms. Two cases of extreme sea state are investigated using ASAR wave mode data using different algorithms, additionally to the radar altimeter data. The case studies show that the single track of ASAR can provide wave height as well as wave direction information. Together with the nadir track of the RA, both SAR and altimeter can be used jointly validating the numerical wave models. Therefore new assimilation schemes could be developed to achieve higher accuracy in sea state forecasting.

- **Global sea state statistics using ASAR wave mode data**

Based on the full year dataset from June 2006 to May 2007, ASAR wave mode data were processed using the CWAVE_ENV algorithm. A 10-year return period of global extreme SWH is estimated to be 18.8 m using the lognormal PDF.

Seasonal and yearly wave maps for SWH, mean wave period, and wave steepness are compiled. Strong storm regions with high waves and long swells can be observed in the maps. The summer monsoon leads to mean SWH of 4.0 ~ 4.5 m over the

Northwest Indian Ocean. Annual mean comparison to the results of ERA-40 shows that regions with high wave systems, e.g. the North Pacific and the North Atlantic, are measured correctly by the ASAR measurements. In addition, a much stronger signal caused by the monsoon is found in the ASAR results and extreme swells are additionally found in the southwest of Australia.

ASAR measurement of global wave steepness is a new contribution to the sea state statistics. Besides the basins with high waves and long swell, also some other regions with high steepness are shown in the maps, e.g. the region between Madagascar and the west coast of Australia.

- **Observation of coastal wave processes using TerraSAR-X data**

In the last part of the thesis, high resolution wave measurements using the new TerraSAR-X sensor are investigated.

When surface waves propagate from deep water into shallow water regions, wavelength, direction and height of the waves change, e.g. caused by the underwater topography, and surface currents. While the SAR wave mode data are useful for global wave studies, SAR data with higher resolution as well as larger coverage are needed in coastal regions to investigate spatial changes of sea state.

A new empirical algorithm XWAVE was developed for high resolution TerraSAR-X data, yielding the peak wavelength and wave direction for the analysis of wave refraction and diffraction as caused by the rapid changing bathymetry around Terceira island in the North Atlantic.

A cross sea situation is identified in the TerraSAR-X Stripmap mode image, which is generated by the refracted and diffracted waves. An effect of less wave angle spreading effect is observed in this situation, which may indicate the change of sea state.

- **Outlook**

The present study shows that the newly developed empirical algorithm CWAVE_ENV is suitable for global integral wave parameter analysis. This opens the potential of global SAR wave mode measurements of ocean wave parameters on tracks parallel to the altimeter. The result can be used for wave climate research.

By combining the SAR measurements with the radar altimeters onboard the same

platforms, both the spatial and temporal sampling is increased as measurements on parallel tracks are available This will improve the retrieval of seasonal and annual variations for global sea state.

Chapter 11

Appendices

Appendix 1: Principle of radar altimeter

Radar altimeters on board the satellite permanently transmit signals at high frequency (Topex-Poseidon - over 1700 pulses per second) to the Earth, and receive the echo from the sea surface. This is analyzed to derive a precise measurement of the round-trip time between the satellite and the sea surface. The time measurement, scaled by the speed of light (at which electromagnetic waves travel), yields a measurement of the satellite-to-ocean range R . As electromagnetic waves travel through the atmosphere, they can be decelerated by water vapor or by ionization. Once these phenomena are corrected for, the final range R is estimated within 2 cm. The ultimate aim is to measure the sea level. This requires independent measurements of the satellite orbital trajectory, i.e. exact latitude, longitude and altitude coordinates. If the height of the satellite, H_{sat} , is known relative to a reference level, then the height, h , of the sea above the reference level is simply determined .

$$h = H_{sat} - R \tag{11.1}$$

The radar altimeter receives the reflected wave, which varies in intensity over time. Fig. 11.1 illuminates the interaction of the radar pulse of duration τ with a smooth sea surface. The reflected wave's power increases sharply from the moment the leading edge of the radar signal strikes the surface. In practice, sea surface is rough rather than flat. In this case the conditions in Fig. B2 apply. As a result, the first reflection of energy commences when the leading edge of the pulse reaches the topmost crests of the waves at A, earlier than for the flat surface in position B, but the reflected energy does not achieve its maximum until the trailing edge reaches the lowest wave trough at C, [*Robinson*, 2004]. In this way, the radar altimeter is able to average out the effect of the ocean waves and consequently integral wave parameters, like significant wave height can be derived from the waveforms.

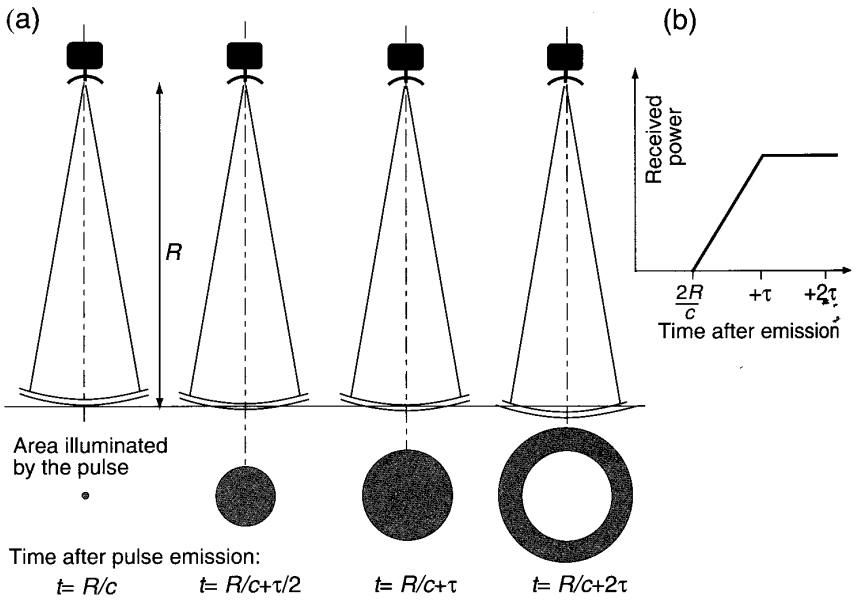

Figure 11.1 Interaction of a pulse of duration τ with a smooth sea surface. (a) The illuminated surface geometry. (b) The resulting power of the reflected pulse.

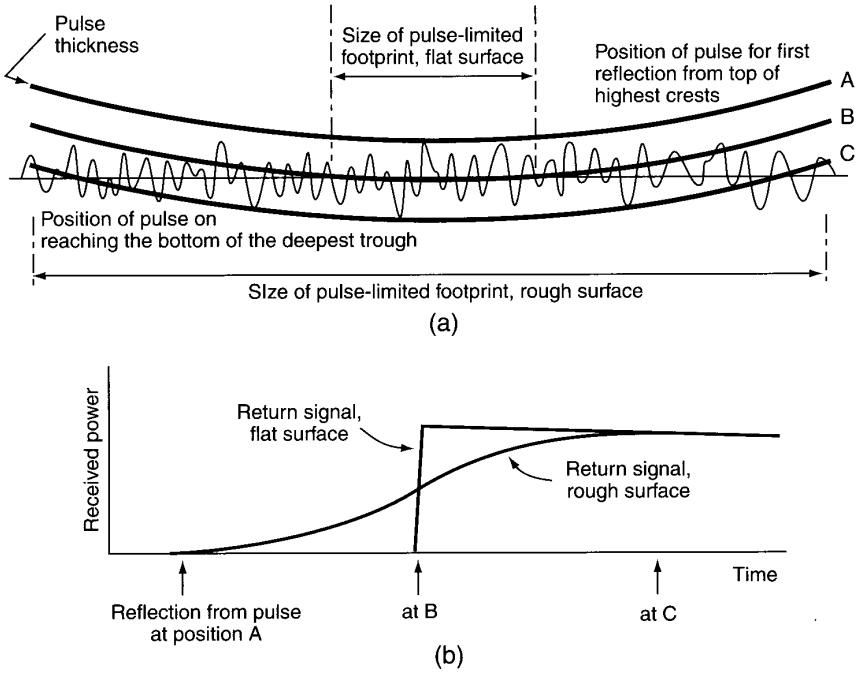

Figure 11.2 Interaction of a pulse with a rough sea surface. (a) The illuminated surface geometry. (b) The resulting power of the reflected pulse.

(Fig. B1 and B2 are derived from [*Robinson*, 2004])

Appendix 2: Numerical wave models data

In the present study, WAM cycle 4 operated in different meteorological centers are used, i.e. ECMWF reanalyzed model, and forecast model results from Deutscher Wetterdienst (DWD, German Weather Service). Details about these models are given as follows.

ECMWF reanalysis wave model

This model is provided with full two-dimensional spectra on a polar grid with 24 direction bins and 30 frequency bins beginning from 0.03452Hz with logarithmic increment of 1.1Hz and achieved at the four main synoptic hours 00, 06, 12 and 18 UTC. They are collocated with the ASAR wave mode data and collected from the CERSAT collocation system (http://www.ifremer.fr/cersat/en/data/data.htm).
It needs to be pointed out that the collocated WAM model results have been assimilated with inverted ASAR wave mode level 1b products and its performance has been assessed by [*Abdalla*, 2008] with global validation.

DWD Forecast wave model

The numerical wave forecast model provided by the DWD includes a global (GSM: Global Sea wave Model) and regional wave models for North Sea and Baltic Sea (LSM: Local Sea wave Model).

Since the area of interest for this investigation is the northern part of Europe, the forecast results obtained by the wave model LSM are used to check whether the extreme storm events in the North Sea and in the Baltic Sea are predicted for several cases [*Behrens and Günther*, 2008]. The LSM runs on a model grid situated between 40.55º N to 66.05ºN and 3.75ºW to 30.75ºE, with a spatial resolution of 0.1º by 0.167º (around 10 km) and 3h temporal resolution which is the same with GSM model. GSM model has a coarse spatial resolution of 0.75º by 0.75º.

Fig. 11.3 shows SWH derived from DWD LSM (left panel) and GSM (right panel) model on January 26, 2008 at 18:00 UTC in North Atlantic. One can see that the due to the higher resolution that fine wave field structure is visible in LSM model. On the other hand, LSM model shows higher value in high sea state (i.e. storm Paula in Norwegian coasts) and lower in low sea state (i.e. Mediterranean ocean).

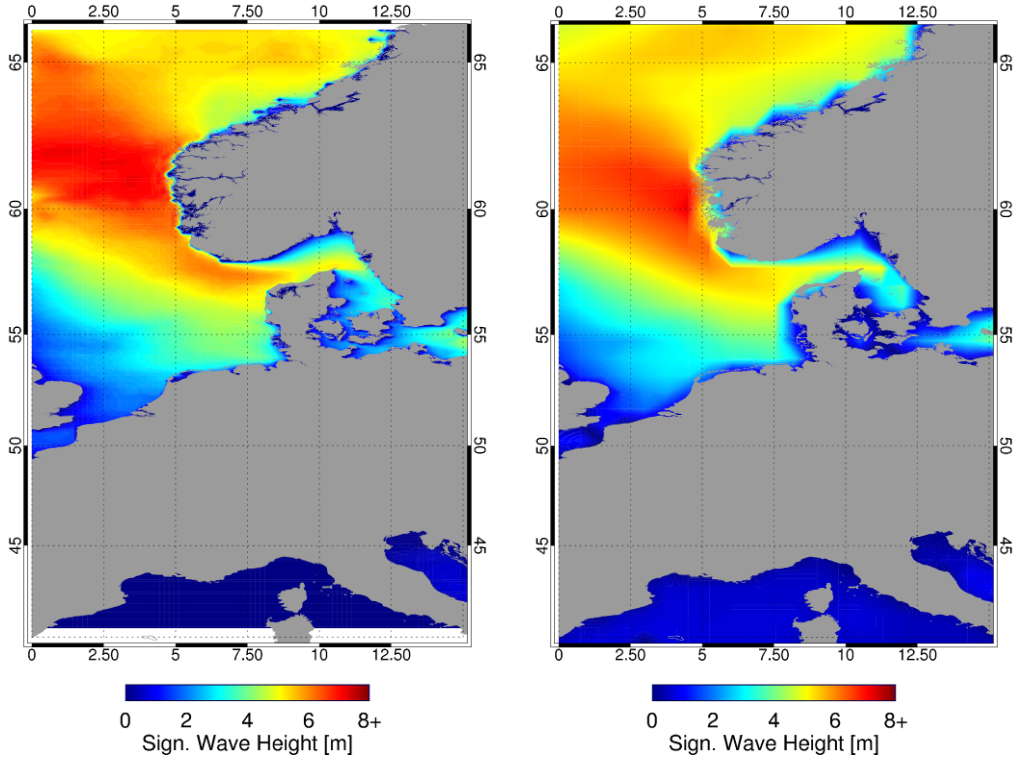

DWD LSM Model DWD GSM Model

Figure 11.3 SWH of DWD LSM model (left) and GSM model (right) on January 26, 2008 at 18:00 UTC in North Atlantic

KNMI C-ERA-40 wave model

As introduced in the above paragraph, the validation results show that ERA-40 SWH reveals some underestimation in higher sea state. On the other hand, the ERA-40 SWH has inhomogeneous time series due to assimilation of different altimeter dataset. Thus a non-parametric method [*Caires and Sterl*, 2005] that predicts the bias between ERA-40 SWH data and TOPEX altimeter measurements was implemented in ERA-40 wave field to create a new 45-year global 6-hourly SWH dataset - the C-ERA-40 dataset with spatial resolution of 1.5° by 1.5°.

Appendix 3: List of buoys used for validation and comparison

Name, latitude and longitude of buoys used for validation of SAR ocean wave algorithms is given in Tab. 11.1. The positions of the buoys are shown in Fig. 4.4

Table A1. Name, Latitude and Longitude of buoys used for validation, corresponding to the red cross marks shown in Fig. 4.4

Station	Latitude	Longitude	Station	Latitude	Longitude
NODC_41001	34°44'N	72°41'W	**NODC_51001**	23°26'N	162°13'W
NODC_41002	32°19'N	75°22'W	**NODC_51002**	17°11'N	157°47'W
NODC_41009	28°30'N	80°10'W	**NODC_51003**	19°13'N	160°49'W
NODC_41010	28°57'N	78°29'W	**NODC_51004**	17°31'N	152°29'W
NODC_42001	25°54'N	89°40'W	**NODC_51028**	0°01'S	153°52'W
NODC_42002	25°10'N	94°25'W	**NODC_fpsn7**	33°29'N	77°35'W
NODC_42003	26°04'N	85°56'W	**NODC_46063**	34°16'N	120°42'W
NODC_42019	27°55'N	95°22'W	**NODC_46066**	52°42'N	154°59'W
NODC_42020	26°56'N	96°42'W	**NODC_46084**	56°35'N	136°10'W
NODC_42035	29°14'N	94°25'W	**MEDS_C44137**	42°17'N	62°00'W
NODC_42036	28°30'N	84°31'W	**MEDS_C44140**	43°45'N	51°45'W
NODC_42039	28°47'N	86°01'W	**MEDS_C44141**	43°00'N	58°00'W
NODC_42040	29°11'N	88°13'W	**MEDS_C44251**	46°26'N	53°23'W
NODC_44004	38°29'N	70°26'W	**MEDS_C44255**	47°17'N	57°21'W
NODC_44008	40°30'N	69°26'W	**MEDS_C44258**	44°30'N	63°24'W
NODC_44011	41°07'N	66°35'W	**MEDS_C46004**	50°56'N	136°05'W
NODC_44014	36°37'N	74°50'W	**MEDS_C46036**	48°21'N	133°56'W
NODC_44025	40°15'N	73°10'W	**MEDS_C46131**	49°55'N	124°59'W
NODC_46002	42°36'N	130°16'W	**MEDS_C46132**	49°44'N	127°56'W
NODC_46005	46°01'N	130°58'W	**MEDS_C46134**	48°40'N	123°29'W
NODC_46011	34°53'N	120°52'W	**MEDS_C46145**	54°22'N	132°25'W
NODC_46012	37°22'N	122°53'W	**MEDS_C46146**	49°20'N	123°44'W
NODC_46013	38°14'N	123°19'W	**MEDS_C46183**	53°37'N	131°06'W
NODC_46014	39°12'N	123°58'W	**MEDS_C46184**	53°55'N	138°51'W
NODC_46015	42°45'N	124°51'W	**MEDS_C46185**	52°25'N	129°49'W
NODC_46022	40°47'N	124°32'W	**MEDS_C46204**	51°22'N	128°45'W
NODC_46023	34°42'N	120°58'W	**MEDS_C46205**	54°10'N	134°17'W
NODC_46025	33°45'N	119°05'W	**MEDS_C46206**	48°50'	126°00'W
NODC_46027	41°51'N	124°23'W	**MEDS_C46207**	50°53'N	129°55'W
NODC_46028	35°44'N	121°53'W	**MEDS_C46208**	52°31'N	132°41'W
NODC_46029	46°08'N	124°31'W	**EUROP_41100**	15°54'N	57°54'W
NODC_46035	57°03'N	177°35'W	**EUROP_41101**	14°36'N	56°12'W
NODC_46042	36°45'N	122°25'W	**EUROP_62001**	45°12'N	5°00'W
NODC_46047	32°26'N	119°32'W	**EUROP_62029**	48°42'N	12°30'W
NODC_46050	44°38'N	124°30'W	**EUROP_62081**	51°00'N	13°24'W
NODC_46053	34°14'N	119°52'W	**EUROP_62105**	55°24'N	12°24'W
NODC_46059	38°02'N	130°00'W	**EUROP_62108**	53°30'N	19°24'W
NODC_46061	60°14'N	146°50'W	**EUROP_62163**	47°30'N	8°24'W
			EUROP_64045	59°06'N	11°42'W

Appendix 4: SAR image spectrum estimation using periodogram method

A two-dimensional ASAR image with the size of B_x and B_y size in range and azimuth direction are divided into nb_x and nb_y subscenes respectively. The relation is given by,

$$nb_x = B_x / n_x \ , \ nb_y = B_y / n_y \tag{11.2}$$

Where n_x=256 and n_y=512 are taken to be the subscene size used to divide the entire samples of B_x and B_y in range and azimuth direction. The two-dimensional FFT is performed on every subscene, i.e., normalized subscene G with pixel size n_x and n_y.

$$F_G = fft_{nx*ny}(G) \tag{11.3}$$

The power density spectrum for every subscene denoted by P_S,

$$P_S = (F_G)^2 \tag{11.4}$$

Summing the subscenes power density spectrum and averaging to reduce the variance, the entire ASAR image spectrum P is given by,

$$P = \frac{1}{nb_x * nb_y} \sum P_S \tag{11.5}$$

The Fourier transform theory states that the integral of the image in the frequency domain equals to the image variance in the spatial domain. The Cartesian spectrum computed in step (11.5) needs to be normalized to ensure this case. The normalized ASAR image spectrum is denoted as $\overline{P}$,

$$\overline{P} = P * \left(\sum P * dk_x * dk_y \right)^{-1} \tag{11.6}$$

In (11.6) dk_x, dk_y is the wave number spacing in ASAR image range and azimuth direction, given by,

$$dk_x = 2\pi / (B_x * d_x) \quad , \ dk_y = 2\pi / (B_y * d_y)$$

(11.7)

d_x, d_y is the pixel spacing in meters of ASAR image.

The ASAR parameters to be used for the CWAVE_ENV model are then computed from the SAR image spectrum $\overline{P}$ by projection onto the subspace spanned by the orthonormal functions, i.e., by computing the respective scalar products.

$$S = \sum \overline{P}(k_x, k_y) h_i(k_x, k_y) dk_x dk_y$$

(11.8)

where $1 \le i \le n_\varphi n_k$ and h_i is the orthonormal functions and their exact forms are proposed in the CWAVE_ENV model.

Appendix 5: Probability Density Functions (PDF)

Normal Distribution

The normal distribution or Gaussian distribution is a continuous probability distribution that describes data that clusters around a mean or average. The graph of the associated probability density function is bell-shaped, with a peak at the mean, and is known as the Gaussian function. The normal distribution can be used to describe, at least approximately, any variable that tends to cluster around the mean.

The probability density function for a normal distribution is given by the formula

$$p(x) = \frac{1}{\sigma\sqrt{2\pi}} \mathbf{exp}\left(-\frac{(x-\mu)^2}{2\sigma^2}\right) \tag{11.9}$$

where μ is the mean, σ is the standard deviation, and **exp** denotes the exponential function.

The Weibull distribution has two parameters, the 'shape' parameter k and the 'scale' parameter λ as given in (E.2). It is named after [*Waloddi Weibull*, 1951].

$$p(x) = \frac{k}{\lambda}\left(\frac{x}{\lambda}\right)^{k-1} \mathbf{exp}^{-(x/\lambda)^k} \tag{11.10}$$

Under certain parameterizations, the Weibull distribution reduces to several other familiar distributions:

- When $k = 1$, it is the exponential distribution.
- When $k = 2$, it becomes equivalent to the Rayleigh distribution
- When $k = 3.4$, it appears similar to the normal distribution.
- As k goes to infinity, the Weibull distribution asymptotically approaches the Dirac delta function.

Bibliography

Abdalla, S., P. A. E. M. Janssen and J.-R. Bidlod, Status of global validation of ENVISAT ASAR Wave Mode Products at ECMWF, *in Proc. SEASAR workshop*, ESRIN, Frascati, Italy, 2008, ESA-SP656.

Airy, G. B. Tides and waves. in H.J. Rose, et al.. *Encyclopaedia Metropolitana*. Mixed Sciences. 3. 1817–1845. . Also: "Trigonometry, On the Figure of the Earth, Tides and Waves", 1841

Alpers, W and C. Brüning, On the relative importance of motion-related contributions to the SAR imaging mechanism of ocean surface waves, *IEEE Trans. Geosci., and Rem. Sens.,* 24, 873-885, 1986

Alpers, W. and B. Brümmer, Atmospheric boundary layer rolls observed by the synthetic aperture radar aboard the ERS-1 satellite, *J. Geophys. Res.*, 99, 12613-12621, 1994

Alves, J., and I.R. Young, On estimating extreme wave heights using combined Geosat, Topex/Poseidon and ERS-1 altimeter data. Applied Ocean Research, 25(4), 167-186, 2003.

Amante, C. and B. W. Eakins, "ETOPO1 1 arc-minute global relief model: procedures, data sources and analysis," National Geophysical Data Center, NESDIS, NOAA, U.S. Department of Commerce, Boulder, CO, 2008

Arthur, R. S. "The effect of islands on surface waves," *Bulletin of the Scripps Institution of Oceanography*, vol.6, 1951

Bacon S., and D. J. T. Carter, Wave climate changes in the North Atlantic and North Sea. *Int. J. Climatol.*, 11, 545–558, 1991.

Bao, M. Q. and W. Alpers, On the cross spectrum between individual-look synthetic aperture radar images of ocean waves, *IEEE Trans. Geosci. and Rem. Sens.,* 36(3), 922-932, 1998;

Battjes, J. A., Long-term wave height distributions at seven stations around the British Isles. *Ocean Dynamics*, 25(4), 179-189, 1972.

Beal,R.C. D.G. Tilley, F.M. Monaldo, "Large- and small-scale spatial evolution of digitally processed ocean surface wave spectra from the Seasat synthetic aperture radar," *J. Geophys. Res*., vol. 88, pp.1761-1778, 1983.

Behrens, A. and H. Günther, Operational wave prediction of extreme storms in Northern Europe, *Natural Hazards*, doi: 10.1007/s11069-008-9298-3, 2008.

Bidlot, J.R., D.J. Holmes, P.A. Wittmann, R. Lalbeharry, and H.S. Chen, Intercomparison of the Performance of Operational Ocean Wave Forecasting Systems with Buoy Data. , 17, 287–310, 2002

Breit H., Schaettler B. and Steinbrecher U., A high precision workstation-based chirp scaling SAR precessor, *Proceeding of the IGARSS97*, Singapore, 1997

Breivik, L.-A., M. Reistad, H. Schyberg, J. Sunde, H. E. Krogstad, and H. Johnsen, Assimilation of ERS SAR wave spectra in an operational wave model, *J. Geophys. Res.,* 103, 7887–7900, 1998

Brooker, G., UWA processing algorithm specification, version 2.0,Tech. Rep., Eur. Space Agency, ESTEC/NWP, Noordwijk, The Netherlands,1995

Caires, S. and A. Sterl, Validation of ocean wind and wave data using triple collocation, *J. Geophys. Res.*, 108 (C3), doi: 10.1029/2002JC001491, 2003

Caires, S., A. Sterl, and C. Gommenginger, Global ocean mean wave period data: validation and description, *J. Geophys. Res.,* 110, C02003, doi:10.1029/2004JC002631,2005

Caires, S., and A. Sterl, 100-Year Return Value Estimates for Ocean Wind Speed and Significant Wave Height from the ERA-40 Data. *J. Climate*, 18, 1032–1048, 2005

Caires, S., and A. Sterl, A New Nonparametric Method to Correct Model Data: Application to Significant Wave Height from the ERA-40 Re-Analysis, *J. Atmos. Oceanic Technol.*, 22, 443–459, 2005

Carrar, W. C, R. G. Goodman and R.M. Majewski, Spotlight Synthetic Aperture Radar: Signal Processing Algorithms. Boston, MA, Artech House Publishers, 1995

Carter, D. J. T., P. G. Challenor, and M. A. Srokosz, An assessment of Geosat wave height and wind speed measurements, *J. Geophys. Res*., 97, 11,383–11,392, 1992

Challenor, P., Ch. Gommenginger, D.Woolf , M. Srokosz , D.Carter , and D. Cotton, Satellite altimetry: A revolution in understanding the wave climate

Challenor, P.G. and P.D. Cotton, The joint calibration of altimeter and in-situ wave heights. *World Meteorological Organization document number WMO/TD-No.1081*, JCOMM Technical Report No. 13, 2002

Challenor, P., Wimmer, W. and Ashton, I. (2004) Climate change and extreme wave heights in the North Atlantic. In *proc. 2004 Envisat and ERS Symposium,* Salzburg, Austria, 2004

Chelton, D.B., K.J. Hussey, and M.E. Parke, Global Satellite Measurements of Water-Vapor, Wind- Speed and Wave Height, *Nature*, 294(5841), 529-532, 1981

Chen, G., S.W. Bi, and R. Ezraty, Global structure of extreme wind and wave climate derived from TOPEX altimeter data. *Int. J. Remote Sensing*, 25, 1005-1018., 2004

Cooper, C.K., and G.Z. Forristall, The Use of Satellite Altimeter Data to Estimate the Extreme Wave Climate. *J. Atmos. Oceanic Technol.*, 14, 254–266,1997

Cotton, P.D., P.G., Challenor, D.J.T.Carter, An assessment of the accuracy and reliability of GEOSAT, ERS-1, ERS-2 and Topex altimeter measurements of significant wave height and wind speed, *Proc. CEOS Wind and Wave Valid Workshop*, 81-93, ESA, ESTEC, The Netherlands, 1997

Dietrich, G., K. Kalle, W. Krauss and G. Siedler, *Allgemeine Meereskunde. Eine Einfruehrung in die Ozeanographie*, Gebrueder Borntraeger, Berlin, 1975

Elfouhaily, T., B. Chapron, K. Katsaros, and D. Vademark, A unified directional spectrum for long and short wind-driven waves. *J. Geophys. Res.*, 102, 15 781 – 15 796, 1997

Engen, G. and H. Johnson, SAR-ocean wave inversion using image cross spectra, *IEEE Trans. Geosci., and Rem. Sens.*, 33, 1047-1056, 1995

Engen, G., Johnsen, H., Høgda, K.A., Chapron, B., "Envisat ASAR Level 2 Wave Mode Product Algorithm Specification Software Requirement Document", NORUT IT Doc. No.: 650/1-01,v2.2.5, Oct., 2001

European Space Agency, *ENVISAT ASAR Product Handbook*, Issue 2.2, 2007

Ferreira, J. A., and C. Guedes Soares, An application of the peaks over threshold method to predict extremes of significant wave height. *J. Offshore Mech. Arct. Eng.,* 120**,** 165–176, 1998

Gade, M., W. Alers, H. Hühnerfuss, H. Masuko and T. Kobayashi, Imaging of biogenic and anthropogenic ocean surface files by the multi-frequency/multi-polarization SIR-C/X-SAR, *J. Geophys. Res.*, 103, 18851-18866, 1998

Golding, B., A wave prediction system for real-time sea state forecasting, *Q. J. Roy Met Soc*, vol.109, 393-416, 1983

Gommenginger, C. P., M. A. Srokosz, P. G. Challenor, and P. D. Cotton, Measuring ocean wave period with satellite altimeters: A simple empirical model, *Geophys. Res. Lett.*, 30(22), 2150, doi:10.1029/2003GL017743,2003

Gordon, H.R., D.K. Clark, J.W. Brown, O.B. Brown, R.H. Evans and W.W. Broenkow, Phytoplankton pigment concentrations in the Middle Atlantic Bight: Comparison of ship determination and CZCS estimates. *Appl. Opt.* 22, 20–36, 1983

Greenwood, J. A., V. J. Cardone and L. M. Lawson. Intercomparison test version of the SAIL wave model. In Ocean Wave Modeling, The SWAMP Group (24 authors). Plenum Press, New York, 221-233, 1985

Grevemeyer I., R. Herber, and H.-H. Essen, Microseismological evidence for a changing wave climate in the northeast Atlantic Ocean, *Nature*, 408, 349–352, 2000

Guedes Soares, C. and A. C. Henriques, Statistical Uncertainty in Long-Term Distributions of Significant Wave Height. *J. Offshore Mech. Arct. Eng.*, 118(4), 284-291, doi:10.1115/1.2833917, 1996

Gulev, S. K., V. Grigorieva, A. Sterl, and D. Woolf, Assessment of the reliability of wave observations from voluntary observing ships: Insights from the validation of a global wind wave climatology based on voluntary observing ship data, *J. Geophys. Res.*, 108(C7), 3236, doi:10.1029/2002JC001437,2003

Gulev, S. K., and V. Grigorieva, Last century changes in ocean wind wave height from global visual wave data, *Geophys. Res. Lett.*, 31, L24302, doi:10.1029/2004GL021040,2004

Günther, H., S. Hasselmann, and P.A.E.M., Janssen, *The WAModel cycle 4 (revised version)*, Technical report, Deutsches Klimarechenzentrum (DKRZ), Hamburg, Germany, 1992

Günther, H., W. Rosenthal, M. Stawarz, Carretero, J.C., M. Gomez, I. Lozano, O. Serano, and M. Reistad, The wave climate of the Northeast Atlantic over the period 1955-94: the WASA wave hindcast. *Global Atmos. Ocean System,* 6, 121-163, 1998

Hasselmann, K., On the non-linear energy transfer in a gravity-wave spectrum Part 1. General theory. *J. of Fluid Mech.,* 12, 1962

Hasselmann, K., On the non-linear energy transfer in a gravity wave spectrum Part 2. Conservation theorems; wave-particle analogy; irrevesibility. *J. of Fluid Mecha., Digital Archive,* 273-281, doi:10.1017/S0022112063000239,1963

Hasselman, K. , T. P. Barnett, E. Bouws, D. E. Carlson, and P. Hasselmann, Measurements of wind-wave growth and swell decay during the joint north sea wave project (JONSWAP), *Deutsche Hydrographische Zeitschrift*, 8(12), 1973

Hasselmann, K., On the spectral dissipation of ocean waves due to whitecapping, *Boundary Layer Meteor.*, 6, 107-127, 1974

Hasselmann, K., R.K. Raney, W. J. Plant, et al., Theory of synthetic aperture radar ocean imaging: A MARSEN view. *J. Geophys. Res.,* 90, 4659-4686, 1985

Hasselmann, K. and S. Hasselmann, On the nonlinear mapping of an ocean wave spectrum into a synthetic aperture radar image spectrum and its inversion, *J. Geophys. Res.,* 96, 10713-10729, 1991

Hasselmann, S., C. Brüning, K. Hasselmann and P. Heimbach, An improved algorithm for the retrieval of ocean wave spectra from SAR image spectra. *J. Geophys. Res.*, C101, 16615-16629, 1996

Heimbach, P., S. Hasselmann, and K. Hasselmann, Statistical analysis and intercomparison with WAM model data of three years of global ERS-1 SAR wave Mode Spectral retrievals, *J. Geophys. Res.,* 103, 7931–7977, 1998

Hersbach, H., A. Stoffelen, and S. de. Haan, An Improved C-band scatterometer ocean geophysical model function: CMOD5. *J. Geophys. Res.,* 112, doi:10.1029/2006JC003743, 2007

Hollinger, J.P., *DMSP Special Sensor Microwave/Imager Calibration/Validation*. Final Report, Vol. I., Space Sensing Branch, Naval Research Laboratory, Washington D.C., 1989

Holthuijsen, L. H. 2007. Waves in ocean and coastal waters. Cambridge: Cambridge University Press

Irvine, D. E. and D. G. Tilley, "Ocean wave directional spectra and wave-current interaction in the Agulhas from the shuttle imaging radar-B Synthetic Aperture Radar," *J. Geophys. Res.*, vol. 93(C12), pp.15, 389–15,401, 1998

Janssen, P. A. E. M., P. Lionello, M. Reistad, and A. Hollingsworth, Hindcasts and data assimilation studies with the WAM model during the Seasat period, *J. Geophys. Res.*, 94, 973–993. 1989

Janssen, P. A. E. M., Progress in ocean wave forecasting, *J. Comput. Phys.*, 227, 3572-3594, 2008

Jaspers, N.H., Statistical distribution patterns of ocean waves and of wave induced ship stresses and motions with engineering applications. *Trans. Soc. Nav. Archit. Mar. Eng.*, 64, 376-432, 1956

Kerbaol, V. B. Chapron, and P. W. Vachon, "Analysis of ERS-1/2 synthetic aperture radar wave mode imagettes," *J. Geophys. Res*., vol. 103, pp.7833–7846, 1998

Kerbaol, V., Analyse spectrale et statistique vent-vagues des images radar a ouverture synthetique, Ph.D. thesis, Univ. de Rennes, Rennes, France,1997

Kinsman, B., *Wind Waves: Their Generation and Propagation on the Ocean Surface.* Prentice-Hall, 1965

Komen, G. J., L. Cavaleri, M. Donelan, K. Hasselmann, S. Hasselmann, P.A.E.M. Janssen, *Dynamics and modelling of ocean waves*, Cambridge University Press, 1994

König, Th., S. Lehner, and J. Schulz-Stellenfleth, Global analysis of a 2 year ERS-2 wave mode dataset over the Ocean, in *Proc. of IGARSS 2007*, Barcelona, Spain, 2007

Krogstad H.E., A simple derivation of Hasselmann's nonlinear ocean –synthetic aperture radar transforms, *J. Geophys. Res.*, 97(C2), 2421-2425, 1992

Krogstad, H. E. S. F. Barstow, Satellite wave measurements for coastal engineering applications*, Coastal Eng.*, 37, 283-307,1999

Lamb, H., *Hydrodynamic*s, 6th, first American edition. New York: Dover Publications, 1945

Lefèvre, J.-M., and L. Aouf, Use of wind/wave satellite data for numerical wave predictions at Meteo-France, Globe Wave workshop, Brest, France, 2007

Lehner, S., J. Horstmann, W. Koch, and W. Rosenthal, Mesoscale wind measurements using recalibrated ERS SAR images, *J. Geophys. Res*., 103, 7847–7856, 1998

Lehner, S., J. Schulz-Stellenfleth, J. B. Schättler, H. Breit, and J. Horstmann, Wind and wave measurements using complex ERS-2 wave mode data, *IEEE Trans. Geosci., and Rem. Sens.*, 38, 2000

Lehner, S. J. Schulz-Stellenfleth, S. Brusch and X.-M. LI "Use of TerraSAR-X Data for Oceanography," in *Proc. of EUSAR 2008*, Friedrichshafen, Germany, 2008

Li, X.-F., P. William, et al., "Observation of hurricane-generated ocean swell refraction at the Gulf Stream north wall with the RADARSAT-1 synthetic aperture radar," *IEEE Trans. Geosci., and Rem. Sens.*, vol.40, pp.2131-2142, 2002

Li, X.-M., Lehner, S., M.-X.HE, Ocean wave measurements based on satellite synthetic aperture radar (SAR) and numerical wave model (WAM) data - extreme sea state and cross sea analysis, *Int. J. Remote Sensing*, 29 (21), 6403 - 6416, doi: 10.1080/01431160802175546, 2008

Lionello, P., H. Günther, and P. A. E. M. Janssen, Assimilation of altimeter data in a global third-generation model, *J. Geophys. Res.,* 97, 14 453–14 474, 1992

Liu, A.K., P. W. Vachon, and C. Y. Peng, "Observation of Wave Refraction at an Ice Edge by Synthetic Aperture Radar," *J. Geophys. Res.*, vol. 96(C3), pp.4803–4808, 1991

Lodge, D. W. S. "Surface expressions of bathymetry on SEASAT synthetic aperture radar images," *Int. J. Remote Sensing*, vol. 4(3), pp.639-653, 1983

Lungu, T., QuikSCAT Science Data Product User's Manual. ftp://podaac.jpl.nasa.gov/ocean_wind/quikscat/L2B/doc/QSUG_v3.pdf, 2006

Lyzenga, D. R., R. A. Shuchman, J. D. Lyden, and C. L. Rufenach, SAR Imaging of Waves in Water and Ice: Evidence for Velocity Bunching, *J. Geophys. Res.*, 90(C1), 1031–1036, 1985

Mackay, E. B. L., C. H. Retzler, P. G. Challenor, and C. P. Gommenginger, A parametric model for ocean wave period from K_u band altimeter data, *J. Geophys. Res.*, 113, C03029, doi:10.1029/2007JC004438, 2008

Mastenbroek, C. and C. F. Valk, A semi-parametric algorithm to retrieve ocean wave spectra from synthetic aperture radar, *J. Geophys. Res.*, 105, 3497-3516, 1998

Miles, J. W., On the generation of surface waves by shear flows. *J. Fluid Mech*., 3, 185-204, 1957

Milman, A. S. A. O. Scheffler, and J. R. Bennett, "A Theory of the Synthetic Aperture Radar Images of Time-Dependent Scenes," *J. Geophys. Res.*, 98(C1), 911–925, 1993

Monaldo, F. "The influence of altitude and look angle on SAR ocean wave imaging: a practical compromise," IGARSS, vol. 3, pp.1519-1521, 1994

Moskowitz, L. Estimates of the power spectrums for fully developed seas for wind speeds of 20 to 40 knots, *Journal of Geophysical Research*, Vol. 69 (24), p.5161–5179, 1964

Naeije, M., E. Doornbos, L. Mathers, R. Scharroo, E. Schrama and P. Visser, Radar Altimeter Database System: exploitation and extension (RADSxx), Final Report. *SRON/NIVR/DEOS publ., NUSP-2 report 02-06, NUSP-2 project 6.3/IS-66, ISBN 90-5623-077-8* September 2002.

Niedermeier, A., J.C. Nieto Borge, S. Lehner and J. Schulz-Stellenfleth, A Wavelet based Algorithm to Estimate Ocean Wave Group Parameters from Radar Images. *IEEE Trans. Geosci., and Rem. Sens.*, 43, No 2, pp 327-336, 2005

Nieto, J.C., K. Hessner, and K. Reichert, "Estimation of the significant wave height with X-Band nautical radars," *Proc. 18th Int. Conf. on Offshore Mechanics and Arctic Engineering*, St. Johns, NF, Canada, ASME, CD-ROM OMAE99/OSU3063, 1999

Nieto Borge, J. C., S. Lehner, A. Niedermeier, and J. Schulz-Stellenfleth, Detection of ocean wave groupiness from spaceborne synthetic aperture radar, *J. Geophys. Res.*, 109, C07005, doi:10.1029/2004JC002298, 2004

Nieto, J.C., G.R. Rodríguez, K.Hessner and P. I. González, "Inversion of marine radar images for surface wave analysis," *J. Atmos. Oceanic Technol.*, vol.21, pp. 1291-1300, 2004

Ochi, M. K., New approach for estimating the severest sea state from statistical data. *Proc. Coastal Eng. Conf.*, 515, 525, 1992

Ouchi, K., S. Maedoi, and H. Mitsuyasu, Determination of ocean wave propagation direction by split-look processing using JERS-1 SAR data, *IEEE Trans. Geosci. and Rem. Sens.,* 37(2), 849-855, 1999

Phillips, O. M., *The Dynamics of the Upper Ocean*, 2nd ed., Cambridge Univ. Press, Cambridge, 1977

Phillips, O.M., On the generation of waves by turbulent wind, *J. Fluid Mech*., 2, 417-445, 1957

Pierson, W. J., Jr., and L. Moskowitz, A Proposed Spectral Form for Fully Developed Wind Seas Based on the Similarity Theory of S. A. Kitaigorodskii, *J. Geophys. Res.*, 69(24), 5181–5190, 1964

Plant, W. J. "Bragg scattering of electromagnetic waves from the air/sea interface, in surface waves and fluxes," *Remote Sens.*, II, 41– 108, 1990

Queffeulou, P., Long-term validation of wave height measurements from altimeters. *Marine Geodesy*, 27, 495-510, 2004

Quilfen, Y., Chapron, B., Collard, F., Serre, M., Calibration/validation of an altimeter wave period model and application of Topex/Poseidon and Janso-1 altimeters. *Marine Geodesy* (Special Issue on Jason1 Calibration/Validation III), 27,535-549, 2004

Robinson, I. S., *Measuring Oceans from Space: The Principles and Methods of Satellite Oceanography*, Springer-Praxis, Chichester, UK, 2004

Romeiser, R., Alpers, W., and Wismann, V., An Improved Composite Surface Model for the Radar Backscattering Cross Section of the Ocean Surface 1 Theory of the Model and Optimization/Validation by Scatterometer Data, *J. Geophys. Res*., 102(C11), 25,237–25,250, 1997

Rosenthal, W. and S. Lehner, Rogue Waves: Results of the MaxWave Project, *J. Offshore Mech. Arct. Eng.*, 130, DOI:10.1115/1.2918126, 2008.

Schrama, E., R. Scharroo, and M. Naeije, Radar Altimeter Database System (RADS): Towards a generic multi-satellite altimeter database system, Final Report.,88p., *SRON/BCRS publ., USP-2 report 00-11, ISBN 90-54-11-319-7* September 2000

Schulz-Stellenfleth, J. and S. Lehner, "Spaceborne synthetic aperture radar observations of ocean waves traveling into sea ice," *J. Geophys. Res.*, vol. 107(C8), pp.3106, doi:10.1029/2001JC000837, 2002

Schulz-Stellenfleth, J. and S. Lehner, Measurement of 2-D Sea Surface Elevation Fields using Complex Synthetic Aperture Radar Data, *IEEE Trans. Geosci., and Rem. Sens.*, 42(6), 1149-1160, 2004

Schulz-Stellenfleth, J., S. Lehner and D. Hoja, A parametric scheme for the retrieval of two-dimensional ocean wave spectra from synthetic aperture radar look cross spectra, *J. Geophys. Res.*, 110, doi: 10.1029/2004JC002822, 2005

Schulz-Stellenfleth, J., Th. König, and S. Lehner, An empirical approach for the retrieval of Integral Ocean wave parameters from synthetic aperture radar data, *J. Geophys. Res.*, 112, doi: 10.1029/2006JC003970, 2007

Schulz-Stellenfleth, J., Lehner, S, König, Th., "First results of the OSIRIS project", presented in SEASAR 2008 workshop, Franscati, Italy, 2008.

Sheng, C., M. Xue, and S. Gao, The structure and evolution of sea breezes during Qingdao Olympics sailing test event in 2006. *Adv. Atmos. Sci.*, 26(1), doi: 10.1007/s00376-009-0132-y, 132-142, 2009

Snodgrass, F. E., G. W. Groves, K. Hasselmann, G. R. Miller, W. H. Munk, and W. H. Powers, Propagation of ocean swell across the Pacific. *Philos. Trans. Roy. Soc. London*, 249A, 431–497, 1966

Stammer, D., Global Characteristics of Ocean Variability Estimated from Regional TOPEX/POSEIDON Altimeter Measurements. *J. Phys. Oceanogr.*, 27, 1743–1769, 1997

Steele, K.E., and M.D. Earle, The status of data produced by NDBC Wave Data Analyzer (WDA) system, *Proc. Oceans'79*, San Diego, CA, Marine Technology Society and IEEE, 212-220,1979

Stewart, R.H., *Methods of Satellite Oceanography*, University of California Press, 1985

Stoffelen, A., and D. Anderson, Scatterometer data interpretation: Estimation and validation of the transfer function CMOD4, *J. Geophys. Res*., 102, 5767– 5780,1997
SWAMP Group, *Ocean Wave Modeling*, Plenum Press, New York, 1985

Tolman, H. L., The numerical model WAVEWATCH: a third generation model for the hindcasting of wind waves on tides in shelf seas. Communications on Hydraulic and Geotechnical Engineering, Delft Univ. of Techn., ISSN 0169-6548, Rep. no. 89-2, 72, 1989

Tolman, H. L., Effects of numerics on the physics in a third-generation wind-wave model. *J. Phys. Oceanogr*., 22, 1095-1111, 1992

Tolman, H. L. and D. Chalikov, Source terms in a third-generation wind-wave model, *J. Phys. Oceanogr*, 26, 2497-2518, 1996

Uppala et al., The ERA-40 re-analysis. *Quart. J. R. Meteorol. Soc.,* 131, 2961-3012, 2005

Vachon, P.W. and West, J.C., Spectral estimation techniques for multilook SAR images of ocean waves, *IEEE Trans. Geosci., and Rem. Sens.,* 30, 568-577, 1992

Vachon, P. W. H. E. Krogstad, and J. S. Paterson, "Airborne and spaceborne synthetic aperture radar observations of ocean waves," *Atmos.-Ocean*, vol. 32, pp. 83-112, 1994
Vachon, P.W. & Dobson. F. W., Validation of Wind Vector Retrieval from ERS-1 SAR Images over the Ocean, The Global Arm. and Ocean Syst., 4, 177-187,1996

Vesecky, J.F., and R.H. Stewart, The observation of ocean surface phenomena using imagery from the Seasat synthetic aperture radar: An assessment, *J. Geophys. Res.,* 87 (C5), 3397–3430. 1982

von Storch, H. and F. Zwiers, Statistical Analysis in Climate Research, Cambridge Univ. Press, NewYork, 1999

von Storch, H., and R. Weisse, Regional storm climate and related marine hazards in the Northeast Atlantic, In Diaz, H.F. and Murnane, R.J. (eds.), Climate Extremes and Society, Cambridge: Cambridge University Press, ISBN 978-0-521-87028-3, p. 54-73, 2008

WAMDI GROUP, The WAM model a third generation ocean wave prediction model, J. *Phys. Oceanogr.,* 18, 1775-1810, 1998

Wang, X.L., and V.R. Swail, Changes of extreme wave heights in northern hemisphere oceans and related atmospheric circulation regimes. *J. Climate,* 14, 2204-2221, 2001

WASA, Changing waves and storms in the Northeast Atlantic? *Bull. Amer. Met. Soc.* 79, 741-760, 1998

Weibull, W., A statistical distribution function of wide applicability. *J. Appl. Mech.-Trans. ASME* 18(3), 293-297, 1951

Wimmer, W., P.G. Challenor, and C. Retzler, Extreme wave heights in the north Atlantic from altimeter data*, Renewable Energy*, 31(2), 241-248, 2006

WMO, 1998: Guide to wave analysis and Forecasting. WMO – No 702

Woolf, D.K., P.G. Challenor, and P.D. Cotton, Variability and Predictability of the North Atlantic wave climate. *J. Geophys. Res.,* 107, 3145, doi:10,1029/2001JC001124, 2002

Young, I. R., W. Rosenthal and F. Ziemer, "Three-dimensional analysis of marine radar images for the determination of ocean wave directionality and surface currents," *J. Geophys. Res.*, vol. 90, pp.1049-1059, 1985

Acknowledgment

I would like to thank all those who encouraged, helped, and supported me to finish the dissertation.

Prof. Hartmut Graßl provided me with the opportunity to accomplish a PhD examination at the University of Hamburg and encouraged me to finish the PhD. I will keep this in mind for the whole life.

All the work involved in the dissertation was under supervision of Dr. Susanne Lehner, team leader of SAR Oceanography group in German Aerospace Center (DLR). Without her kind help and supervision, completion of the dissertation would not have been possible.

I feel like staying at a family in the SAR Oceanography group. My colleagues, Dr. Thomas Koenig, Stephan Brusch, Dr. Andrey Pleskachevsky, Miguel Bruck, Domenico Velotto and Dimitri Hamidi, always treated me as a family member. The friendly atmosphere enhances learning from everyone and sharing experience without reservation.

Dr. Andreas Neumann, the head of the Marine Remote Sensing Department in DLR, provided me with many opportunities to participate conferences and workshops, which broadened my horizon by exchanging ideas with other scientists. He also solved many problems regarding my contract at DLR and I really appreciate this.

Dr. Johannes Schulz-Stellenfleth from the GKSS introduced to me new knowledge and routines for developing SAR ocean wave algorithms. I express my special thanks for him.

Dr. Thomas Bruns from DWD always kindly provided me with the wave model data.

My wife deserves special mentioning. Without her support, it would not have been possible to finish the dissertation in time. Our child, Yuchen, since he was born last year, becomes our source of happiness. Everyday he always gives me surprise and I believe what I have done for the family is well worth.

Only when I have a child I do understand the love from parents. Thanks for my mother and father, who give me so much love and support that could not be only expressed by thanks.